Università degli Studi di Napoli *Federico II*

Università di Camerino

DOTTORATO DI RICERCA IN QUANTUM TECHNOLOGIES

Ciclo XXXIV

Coordinatore: prof. Francesco Tafuri

Static and Dynamic coherence Effects in Fermionic Superfluids at finite Temperature

Settore Scientifico Disciplinare FIS03/FIS02

Dottorando
Verdiana Piselli

Tutore
Prof. Giancarlo Calvanese Strinati

Anni 2018/2021

Contents

Introduction

The stationary (DC) Josephson effect is one of the most striking consequence of the spontaneous broken-symmetry of the phase $\varphi(\mathbf{r})$ of the complex gap parameter $\Delta(\mathbf{r}) = |\Delta(\mathbf{r})|e^{i\varphi(\mathbf{r})}$. It can be observed in a system where a geometrical constraint (like a potential barrier or the insertion of a different material) is placed at the interface between two superconductors [1]. At a microscopic level it can be explained in terms of the coherent tunneling of the Cooper pairs across the constraint. This phenomenon results in a characteristic relation between the stationary supercurrent J and the asymptotic phase difference of $\Delta(\mathbf{r})$ across the constraint, which in its simplest expression takes the form $J = J_c \sin(\delta\phi)$, where J_c is the critical value of the current above which the flow becomes dissipative and superfluidity is destroyed.

The Josephson effect has been observed in both condensed-matter systems [2] and ultra-cold Fermi gases [3, 4, 5]. In the latter case, the interparticle interaction can be tuned via Fano-Feshbach resonances [6, 7], resulting in states characterized by largely overlapping pairs of opposite-spin fermions (in the Bardeen-Cooper-Schrieffer [BCS] limit), to diluite dimers (in the Bose-Einstein Condensate [BEC] limit), across an intermediate regime known as the unitary regime, where the pair size is of the order of the average inter-particle distance.

The Josephson characteristics and their associated critical current values J_c, across the BCS-BEC crossover were studied in details in Refs. [8, 9], where a potential barrier embedded in an otherwise homogeneous superfluid system was considered. The coupling was kept unmodified under the barrier similarly to what occurs in the experiments with ultra-cold atomic gases [3, 4, 5]. This system, which can be referred to as a SS'S junction, was studied in details at $T = 0$ by solving the inhomogeneous Bogoliubov-de Gennes (BdG) equations [10] for various interparticle interaction strengths and potential barriers.

Similar studies were performed at finite temperature in the BCS limit using the mean-field approach taking into consideration tunneling barriers (characterised by a low transmission probability) [11], or considering the high-temperature regimes where Ginzburg-Landau (GL) equation was solved for tunneling barriers [12] or SNS junctions [13, 14]. Many different kinds of junctions have been studied with different methods [15], but only in a restricted region of the coupling-temperature phase diagram or by developping theories valid for strictly specific geometrical constraints. For this reason, in the present work we extend the study in [9] at finite temperature, where the potential barrier used as the geometrical constraint allow to access both low- and high-transmission regimes.

In practice, the BdG equations when applied to inhomogeneous problems are quite demanding to handle. They usually require a large amount of computation time to reach self-consistency and need a considerable memory space to store the functions from which to extract the physical quantities (see Section 1.1 for further

details). For this reason, when dealing with inhomogeneous physical systems, various approximations to the BdG equations were considered, such as the Eilenberger equations [16, 17] in the clean limit (where the carriers mean free path is much larger than the coherence length of the pairs) and the Usadel equations [18, 17] in the dirty limit (where the carriers mean free path is much smaller than the coherence length of the pairs). In this context, in this work we solve the Local Phase Density Approximation (LPDA) equation [19] obtained by a double-coarse graining of the BdG equations, based on the assumption of smooth enough variations for both the magnitude and phase of the gap parameter (see Subsection 1.2.1 for further details). The LPDA equation is a higly non-linear differential equation for the order parameter $\Delta(\mathbf{r})$ and its solution, in place of the BdG equations, leads to a considerable reduction of time and storage requirements.

The geometry mostly considered in this work for the barriers corresponds to a regime where the transmission probability of Cooper pairs cannot be treated as a small quantity as it is done when dealing with a Superconducting-Insulating-Superconducting layers (SIS) junction [11]. This regime, where the width of the potential barrier is non-negligible and the height is small enough with respect to the Fermi energy E_F, can be put in analogy with Superconducting-Normal metal-Superconducting layers (SNS) junctions. These two distinct physical systems can be characterised by similar temperature dependence of the respective critcal current J_c. The critical behaviour of J_c as the critical temperature of the (S) region is approached is the same for both SS'S (in the above described regime) and SNS junctions (cf. [15] and [2]). In this work we show that it is possible to obtain a temperature dependence of the critical current J_c quite similar to that of a SNS junction, upon considering a suitable external potential (single-particle) in place of the change in the inter-particle interaction (two-particle) which occurs at the interfaces of SNS junctions. This result constitutes a bridge between the condensed-matter and ultra-cold gases experiments where it is not possible to modify the interparticle interaction within a few μm.

Although the LPDA equation represents a practical improvement with respect to BdG equations when dealing with problems of physical interest, it can at most recover the same physical contents obtained by the BdG equations. For this reason its results are expected not to be appropriate at finite temperature when the inter-particle interaction is increased from the BCS to the BEC limit, where the Cooper pair size becomes comparable or even smaller than the inter-particle distance. In order to obtain reliable results in this regime, but also in the unitary regime where the Cooper pair size is comparable with the inter-particle distance, it would be desirable to include pairing fluctuations beyond the present mean-field approach. In this work, we provide some insights on this issue, proposing to include pairing fluctuations for inhomogeneous Fermi systems on top of the LPDA equation (in order not to lose the numerical advantages with respect to BdG equations), following the lines of Ref. [20]. Though a complete treatment of this topic is outside the scope of the present work, we provide in Section 2.10 a comparison between some early-stage results for the critical value J_c, obtained within this approach and the experimental data of Ref. [3].

The second part of this work is devoted to the study of the dynamics of a quantum system driven out of equilibrium. Dynamic perturbation of superconducting systems is a flourishing research field. The possibility of inducing superconductivity

above T_c for a limited amount of time [21, 22] promises to endless technological applications. In this context, atomic quantum gases offer a valid platform for building a quantitative understanding of the underlying processes. Realization of out-of-equilibrium protocols in these systems is favoured because of the easy tunability of the relevant parameters. As an example, we can mention the observation of the crossing from the normal to the superfluid phase in atomic quantum gases following a quench of the interaction [23]. In this context, we have solved the time-dependent BdG equations to study the dynamics of a two-component Fermi gas following the action of an external perturbation, in order to provide a close-to-reality perspective of the occurring phenomena.

The thesis is organized as follows. In the first chapter, the main theoretical concepts and tools utilized throughout this work are briefly discussed. In the second chapter, the main results of the study of the Josephson effect are reported, including a detailed mean-field study of the effect, the proposal of an analogy between SNS and $SS'S$ junctions, and early-stage results obtained by including pairing fluctuations on top of the mean-field treatment. In the third chapter, an analysis of three different out-of-equilibrium protocols is reported for a system of N fermions confined in a 1D box potential. In the fourth chapter, the main conclusions and perspectives of this work are briefly discussed.

Chapter 1

Theoretical Background

Ever since its discovery, superconductivity has been a phenomenon with striking experimental manifestations. From 1911, the year of the observation of the resistivity drop to zero in Mercury by Onnes, it has taken almost 50 years for the formulation of a complete theory explaining the phenomenon. Purpose of this Section is to provide an insight on this theory and to discuss the main theoretical instruments used throughout this work.

In particular, whithin the mean-field approach to superfluidity, we will derive the Bogoliubov-de Gennes (BdG) equations, also in their time-dependent version, and the so called Local Phase Density Approximation (LPDA) obtained through a coarse graining procedure of the BdG equations.

Two limiting situations are of special interest: The weak-coupling (BCS) limit for $T \lesssim T_c$ and the strong-coupling (BEC) limit at $T \approx 0$. In these cases, the LPDA equation, like the BdG equations, reduces to the Ginzburg-Landau (GL) and the Gross-Pitaevskii (GP) equation, respectively.

1.1 The Bogoliubov-de Gennes equations

One of the most successful approach used to study superconductivity in the late 60s was the mean-field approach of the BCS theory. Subject of this theory is a system of interacting fermions. The most commonly used kind of interaction is a contact attractive one. The reason why this model works can be briefly explained. Referring to electrons in metals, they can be regarded as freely moving except for occasional scattering by lattice vibrations (Bloch model). It was showed in [24] that, adding to this model the effects of Pauli principle, it can happen that the phonon-electron interaction leads to an effective electron-electron attraction in a narrow energy range around the Fermi surface, resulting in a momentum distribution of the ground state different from that of the normal one (the Fermi sphere). The new ground state, identified as the superconducting one, is characterised by the presence of new formed pairs of electrons with opposite spin and zero total momentum, which are known as Cooper pairs (see [25]).

1.1.1 The mean-field Hamiltonian

Let us consider a two-component Fermi gas with electric charge e interacting through a potential of the contact form $-g\delta(\mathbf{r} - \mathbf{r}')$ (where $g > 0$). The time-independent

grand canonical Hamiltonian of the system reads [26]:

$$\begin{aligned}\hat{K} = \sum_{\sigma=\uparrow,\downarrow} \int d\mathbf{r} \hat{\Psi}^\dagger_\sigma(\mathbf{r}) \left\{ \frac{1}{2m} \left[-i\hbar\nabla + \frac{e\mathbf{A}(\mathbf{r})}{c} \right]^2 + V^\sigma_{\text{ext}}(\mathbf{r}) - \mu_\sigma \right\} \hat{\Psi}_\sigma(\mathbf{r}) \\ - g \int d\mathbf{r} \hat{\Psi}^\dagger_\uparrow(\mathbf{r}) \hat{\Psi}^\dagger_\downarrow(\mathbf{r}) \hat{\Psi}_\downarrow(\mathbf{r}) \hat{\Psi}_\uparrow(\mathbf{r}),\end{aligned} \tag{1.1}$$

where $\hat{\Psi}_\sigma(\mathbf{r})$ and $\hat{\Psi}^\dagger_\sigma(\mathbf{r})$ are the fermionic field operators[1] with spin projection σ, $\mathbf{A}(\mathbf{r})$ the vector potential, $V^\sigma_{\text{ext}}(\mathbf{r})$ the spin-dependent external potential, and μ_σ the chemical potential associated with fermions with spin projection σ.

Dealing with this Hamiltonian results to be hard because of the 4-field operators term. For this reason, the interaction part of $\hat{K}$ is simplified by adopting a bilinear form following the mean-field prescription. The resulting effective Hamiltonian reads:

$$\begin{aligned}\hat{K}_{eff} = \sum_{\sigma=\uparrow,\downarrow} \int d\mathbf{r} \hat{\Psi}^\dagger_\sigma(\mathbf{r}) \left\{ \frac{1}{2m} \left[-i\hbar\nabla + \frac{e\mathbf{A}(\mathbf{r})}{c} \right]^2 + V^\sigma_{\text{ext}}(\mathbf{r}) - \mu_\sigma \right\} \hat{\Psi}_\sigma(\mathbf{r}) \\ - \int \left[\Delta^*(\mathbf{r}) \hat{\Psi}_\downarrow(\mathbf{r}) \hat{\Psi}_\uparrow(\mathbf{r}) + \Delta(\mathbf{r}) \hat{\Psi}^\dagger_\uparrow(\mathbf{r}) \hat{\Psi}^\dagger_\downarrow(\mathbf{r}) \right],\end{aligned} \tag{1.3}$$

where we have introduced the gap parameter

$$\Delta(\mathbf{r}) = g \langle \hat{\Psi}_\downarrow(\mathbf{r}) \hat{\Psi}_\uparrow(\mathbf{r}) \rangle \tag{1.4}$$

with the angular brackets denoting an ensemble average over $\hat{K}_{eff}$.

1.1.2 Explicit derivation of the BdG equations (T=0)

Let us assume that the Hamiltonian $\hat{K}_{eff}$ can be rearranged as

$$\hat{K}_{eff} = E_g + \sum_\nu E_\nu \left(\hat{\gamma}^\dagger_{\nu 1} \hat{\gamma}_{\nu 1} + \hat{\gamma}^\dagger_{\nu 2} \hat{\gamma}_{\nu 2} \right), \tag{1.5}$$

where E_g is the ground state energy, E_ν the energy of the νth excitation, and $\gamma_{\nu\alpha}$ operators which satisfy the fermionic anticommutation relations:

$$\{\hat{\gamma}_{\nu\alpha}, \hat{\gamma}_{\nu'\alpha'}\} = 0, \qquad \left\{\hat{\gamma}^\dagger_{\nu\alpha}, \hat{\gamma}^\dagger_{\nu'\alpha'}\right\} = 0, \qquad \left\{\hat{\gamma}_{\nu\alpha}, \hat{\gamma}^\dagger_{\nu'\alpha'}\right\} = \delta_{\nu\nu'}\delta_{\alpha\alpha'}. \tag{1.6}$$

The assumption made in (1.5) allow us to identify the ground state $|\Phi_0\rangle$ over which the average in Eq. (1.4) is performed, with the property

$$\gamma_{\nu\alpha}|\Phi_0\rangle = 0 \qquad \forall\nu \quad \text{for } \alpha = 1, 2. \tag{1.7}$$

The state $|\Phi_0\rangle$ is commonly referred to as the Bogoliubov vacuum.

[1] The fermionic field operators satisfy the following anticommutation relations:

$$\left\{\hat{\Psi}_\sigma(\mathbf{r}), \hat{\Psi}_{\sigma'}(\mathbf{r}')\right\} = 0, \qquad \left\{\hat{\Psi}^\dagger_\sigma(\mathbf{r}), \hat{\Psi}^\dagger_{\sigma'}(\mathbf{r}')\right\} = 0, \qquad \left\{\hat{\Psi}_\sigma(\mathbf{r}), \hat{\Psi}^\dagger_{\sigma'}(\mathbf{r}')\right\} = \delta_{\sigma\sigma'}\delta(\mathbf{r}-\mathbf{r}'). \tag{1.2}$$

Let us further assume that the field operators in Eq. 1.3 can be written as:

$$\begin{pmatrix} \hat{\Psi}_\uparrow(\mathbf{r}) \\ \hat{\Psi}^\dagger_\downarrow(\mathbf{r}) \end{pmatrix} = \sum_\nu \begin{pmatrix} u_{\nu\uparrow}(\mathbf{r}) & -v^*_{\nu\uparrow}(\mathbf{r}) \\ v_{\nu\downarrow}(\mathbf{r}) & u^*_{\nu\downarrow}(\mathbf{r}) \end{pmatrix} \begin{pmatrix} \hat{\gamma}_{\nu 1} \\ \hat{\gamma}^\dagger_{\nu 2} \end{pmatrix}, \tag{1.8}$$

where $u_{\nu\sigma}(\mathbf{r})$ and $v_{\nu\sigma}(\mathbf{r})$ are complex functions to be specified in the following.

In order for $\hat{\Psi}_\sigma(\mathbf{r})$ and $\hat{\Psi}^\dagger_\sigma(\mathbf{r})$ to satisfy the fermionic anticommutation relation (see (1.2)), $u_{\nu\sigma}(\mathbf{r})$ and $v_{\nu\sigma}(\mathbf{r})$ have to obey the following closure relation:

$$\sum_\nu \left[\begin{pmatrix} u_{\nu\uparrow}(\mathbf{r}) \\ v_{\nu\downarrow}(\mathbf{r}) \end{pmatrix} \begin{pmatrix} u^*_{\nu\uparrow}(\mathbf{r}') & v^*_{\nu\downarrow}(\mathbf{r}') \end{pmatrix} + \begin{pmatrix} -v^*_{\nu\uparrow}(\mathbf{r}) \\ u^*_{\nu\downarrow}(\mathbf{r}) \end{pmatrix} \begin{pmatrix} -v_{\nu\uparrow}(\mathbf{r}') & u_{\nu\downarrow}(\mathbf{r}') \end{pmatrix} \right] = \mathbb{1}\delta(\mathbf{r}-\mathbf{r}'). \tag{1.9}$$

From eq. (1.5) follows that

$$\begin{aligned} [\hat{\gamma}_{\nu\alpha}, \hat{K}_{eff}] &= E_\nu \hat{\gamma}_{\nu\alpha} \\ [\hat{\gamma}^\dagger_{\nu\alpha}, \hat{K}_{eff}] &= -E_\nu \hat{\gamma}^\dagger_{\nu\alpha} \end{aligned} \qquad \text{with} \quad \alpha = 1,2 \tag{1.10}$$

and using the anticommutation relation of fermionic field operators one finds

$$\begin{aligned} [\hat{\Psi}_\uparrow(\mathbf{r}), \hat{K}_{eff}] &= \hat{h}_\uparrow(\mathbf{r})\hat{\Psi}_\uparrow(\mathbf{r}) - \Delta(\mathbf{r})\hat{\Psi}^\dagger_\downarrow(\mathbf{r}) \\ [\hat{\Psi}_\downarrow(\mathbf{r}), \hat{K}_{eff}] &= \hat{h}_\downarrow(\mathbf{r})\hat{\Psi}_\downarrow(\mathbf{r}) + \Delta(\mathbf{r})\hat{\Psi}^\dagger_\uparrow(\mathbf{r}) \end{aligned} \tag{1.11}$$

where

$$\hat{h}_\sigma(\mathbf{r}) = \frac{1}{2m}\left[-i\hbar\nabla + \frac{e\mathbf{A}(\mathbf{r})}{c}\right]^2 + V^\sigma_{\text{ext}}(\mathbf{r}) - \mu_\sigma. \tag{1.12}$$

Using the transformation (1.8) and the relation (1.10) into (1.11) and equating the coefficients of the γ_ν operators, one eventually finds the following equations for $u_{\nu\sigma}(\mathbf{r})$ and $v_{\nu\sigma}(\mathbf{r})$

$$\begin{cases} \hat{h}_\uparrow u_{\nu\uparrow}(\mathbf{r}) - \Delta(\mathbf{r}) v_{\nu\downarrow}(\mathbf{r}) = E_\nu u_{\nu\uparrow}(\mathbf{r}) \\ -\hat{h}^*_\uparrow v_{\nu\uparrow}(\mathbf{r}) - \Delta^*(\mathbf{r}) u_{\nu\downarrow}(\mathbf{r}) = E_\nu v_{\nu\uparrow}(\mathbf{r}) \\ \hat{h}_\downarrow u_{\nu\downarrow}(\mathbf{r}) - \Delta(\mathbf{r}) v_{\nu\uparrow}(\mathbf{r}) = E_\nu u_{\nu\downarrow}(\mathbf{r}) \\ -\hat{h}^*_\downarrow v_{\nu\downarrow}(\mathbf{r}) - \Delta^*(\mathbf{r}) u_{\nu\uparrow}(\mathbf{r}) = E_\nu v_{\nu\downarrow}(\mathbf{r}) \end{cases} \tag{1.13}$$

where

$$\hat{h}^*_\sigma(\mathbf{r}) = \frac{1}{2m}\left[i\hbar\nabla + \frac{e\mathbf{A}(\mathbf{r})}{c}\right]^2 + V^\sigma_{\text{ext}}(\mathbf{r}) - \mu_\sigma. \tag{1.14}$$

Let us remark that the E_ν entering in (1.13) are positive definite because of the assumption (1.5). However, after simple manipulations we can rewrite the second and third equation of (1.13) as follows

$$\begin{aligned} \hat{h}_\uparrow[-v^*_{\nu\uparrow}(\mathbf{r})] - \Delta(\mathbf{r})[u^*_{\nu\downarrow}(\mathbf{r})] &= -E_\nu[-v^*_{\nu\uparrow}(\mathbf{r})], \\ -\hat{h}^*_\downarrow u^*_{\nu\downarrow}(\mathbf{r}) - \Delta^*(\mathbf{r})[-v^*_{\nu\uparrow}(\mathbf{r}) &= -E_\nu u^*_{\nu\downarrow}(\mathbf{r}), \end{aligned}$$

which are the first and fourth equations in (1.13) using the correspondance

$$E_\nu \begin{pmatrix} u_{\nu\uparrow}(\mathbf{r}) \\ v_{\nu\downarrow}(\mathbf{r}) \end{pmatrix} \quad \leftrightarrow \quad -E_\nu \begin{pmatrix} -v^*_{\nu\uparrow}(\mathbf{r}) \\ u^*_{\nu\downarrow}(\mathbf{r}) \end{pmatrix}. \tag{1.15}$$

As a consequence (1.13) can be rearrenged as

$$\begin{pmatrix} h_\uparrow(\mathbf{r}) & -\Delta(\mathbf{r}) \\ -\Delta^*(\mathbf{r}) & -h_\downarrow^*(\mathbf{r}) \end{pmatrix} \begin{pmatrix} u_{\nu\uparrow}(\mathbf{r}) \\ v_{\nu\downarrow}(\mathbf{r}) \end{pmatrix} = E_\nu \begin{pmatrix} u_{\nu\uparrow}(\mathbf{r}) \\ v_{\nu\downarrow}(\mathbf{r}) \end{pmatrix}, \tag{1.16}$$

where now the solutions have both $E_\nu > 0$ and $E_\nu < 0$.

Equation (1.16) is an eigen-value problem, whose eigenvectors are orthonormal to each other (see (1.9)), which has to be solved consistently with the gap equation (1.4). This equation, using the transformation in (1.8) and the property of the state $|\Phi_0\rangle$ (see eq. (1.7)), becomes:

$$\Delta(\mathbf{r}) = -\frac{g}{2} \sum_\nu \left[u_{\nu\downarrow}(\mathbf{r}) v_{\nu\uparrow}^*(\mathbf{r}) + u_{\nu\uparrow}(\mathbf{r}) v_{\nu\downarrow}^*(\mathbf{r}) \right]. \tag{1.17}$$

Other quantities of interest, which can be evalued from $u_{\nu\sigma}(\mathbf{r})$ and $v_{\nu\sigma}(\mathbf{r})$, are the number density and the energy of the system. Their expressions read:

$$n_\sigma(\mathbf{r}) = \langle \Phi_0 | \hat{\Psi}_\sigma^\dagger(\mathbf{r}) \hat{\Psi}_\sigma(\mathbf{r}) | \Phi_0 \rangle = \sum_\nu |v_{\nu\sigma}(\mathbf{r})|^2 \tag{1.18a}$$

and

$$\begin{aligned} E &= \langle \Phi_0 | \hat{K}_{eff} | \Phi_0 \rangle + \sum_\sigma \mu_\sigma \int d\mathbf{r} \langle \Phi_0 | \hat{\Psi}_\sigma^\dagger(\mathbf{r}) \hat{\Psi}_\sigma(\mathbf{r}) | \Phi_0 \rangle \\ &= \int d\mathbf{r} \left\{ \sum_{\nu,\sigma} v_{\nu\sigma}(\mathbf{r}) \left[\hat{h}_\sigma(\mathbf{r}) + \mu_\sigma \right] v_{\nu\sigma}^*(\mathbf{r}) - \frac{1}{g} |\Delta(\mathbf{r})|^2 \right\}. \end{aligned} \tag{1.18b}$$

1.1.3 BdG Equations at finite Temperature

At finite temperature, eq. (1.16) remains formally the same, but an ensemble averages has correpondingly to be performed.

Averages of pairs of fermionic operators $\hat{\gamma}_{\nu\alpha}$ and $\hat{\gamma}_{\nu\alpha}^\dagger$ read:

$$\langle \hat{\gamma}_{\nu\alpha} \hat{\gamma}_{\nu'\alpha'} \rangle_T = 0 \qquad \langle \hat{\gamma}_{\nu\alpha}^\dagger \hat{\gamma}_{\nu'\alpha'}^\dagger \rangle_T = 0 \qquad \langle \hat{\gamma}_{\nu\alpha}^\dagger \hat{\gamma}_{\nu'\alpha'} \rangle_T = \delta_{\nu\nu'} \delta_{\alpha\alpha'} f_F(E_\nu, T), \tag{1.19}$$

where $f_F(E_\nu, T)$ is the Fermi function at temperature T

$$f_F(E_\nu, T) = \frac{1}{e^{\beta E_\nu} + 1} \tag{1.20}$$

with $\beta = 1/k_B T$ (k_B being the Boltzmann constant).

Using the relations (1.19) in eqs. (1.4) and (1.18) we obtain:

$$\Delta_T(\mathbf{r}) = g \langle \hat{\Psi}_\downarrow(\mathbf{r}) \hat{\Psi}_\uparrow(\mathbf{r}) \rangle_T = -\frac{g}{2} \sum_\nu \left[u_{\nu\downarrow}(\mathbf{r}) v_{\nu\uparrow}^*(\mathbf{r}) + u_{\nu\uparrow}(\mathbf{r}) v_{\nu\downarrow}^*(\mathbf{r}) \right] \left[1 - 2 f_F(E_\nu, T) \right], \tag{1.21a}$$

$$n_{T\sigma}(\mathbf{r}) = \langle \hat{\Psi}_\sigma^\dagger(\mathbf{r}) \hat{\Psi}_\sigma(\mathbf{r}) \rangle_T = \sum_\nu \left\{ |u_{\nu\sigma}(\mathbf{r})|^2 f_F(E_\nu, T) + |v_{\nu\sigma}(\mathbf{r})|^2 \left[1 - f_F(E_\nu, T) \right] \right\}, \tag{1.21b}$$

$$
\begin{aligned}
E_T =& \langle \hat{K}_{eff}(T)\rangle_T + \sum_\sigma \mu_{T\sigma} \int d\mathbf{r} \langle \hat{\Psi}^\dagger_\sigma(\mathbf{r})\hat{\Psi}_\sigma(\mathbf{r})\rangle_T = \\
&= \int d\mathbf{r} \left\{ \sum_{\nu,\sigma} v_{\nu\sigma}(\mathbf{r}) \left[\hat{h}_\sigma(\mathbf{r}) + \mu_{T\sigma}\right] v^*_{\nu\sigma}(\mathbf{r}) \left[1 - f_F(E_\nu, T)\right] \right. \\
&\quad \left. + u^*_{\nu\sigma}(\mathbf{r}) \left[\hat{h}_\sigma(\mathbf{r}) + \mu_{T\sigma}\right] u_{\nu\sigma}(\mathbf{r}) f_F(E_\nu, T) - \frac{1}{g}|\Delta_T(\mathbf{r})|^2 \right\}.
\end{aligned} \tag{1.21c}
$$

.

1.1.4 An equivalent version of the BdG Equation

The BdG equations are sometimes not used in the form (1.16), rather in an alternative form obtained introducing the so-called Gorkov propagators or single-particle finite-temperature Green's functions. At first sight, these functions could appear as theoretical constructs of no-use when dealing with an experimental problem, but they provide a direct link to measurable quantities.

As a first step, let us introduce field operators in the *modified* Heisenberg picture

$$
\hat{\Psi}_{K\sigma}(\mathbf{r}\tau) = e^{\hat{K}_{eff}(T)\tau/\hbar}\hat{\Psi}_\sigma(\mathbf{r})e^{-\hat{K}_{eff}(T)\tau/\hbar}, \quad \hat{\Psi}^\dagger_{K\sigma}(\mathbf{r}\tau) = e^{\hat{K}_{eff}(T)\tau/\hbar}\hat{\Psi}^\dagger_\sigma(\mathbf{r})e^{-\hat{K}_{eff}(T)\tau/\hbar} \tag{1.22}
$$

where τ is an imaginary time, and define the normal and anomalous single-particle Green's functions, respectively, as follows

$$
\mathcal{G}(\mathbf{r}\tau, \mathbf{r}'\tau') \equiv -\langle \hat{T}_\tau \left[\hat{\psi}_{K\uparrow}(\mathbf{r}\tau)\hat{\psi}^\dagger_{K\uparrow}(\mathbf{r}'\tau')\right]\rangle_T, \tag{1.23a}
$$

$$
\mathcal{F}(\mathbf{r}\tau, \mathbf{r}'\tau') = -\langle \hat{T}_\tau \left[\hat{\psi}_{K\uparrow}(\mathbf{r}\tau)\hat{\psi}_{K\downarrow}(\mathbf{r}'\tau')\right]\rangle_T, \quad \mathcal{F}^\dagger(\mathbf{r}\tau, \mathbf{r}'\tau') = -\langle \hat{T}_\tau \left[\hat{\psi}^\dagger_{K\downarrow}(\mathbf{r}\tau)\hat{\psi}^\dagger_{K\uparrow}(\mathbf{r}'\tau')\right]\rangle_T, \tag{1.23b}
$$

where $\hat{T}_\tau$ is a time-ordering operator which rearranges the operators to which is applied in decreasing time ordering and multiply them to $(-1)^P$, where P is the number of permutations of fermionic operators needed to obtain the correct time ordering.

The Heisenberg field operators (1.22) obey the following equations of motion:

$$
\hbar\frac{\partial\hat{\Psi}_{K\uparrow}(\mathbf{r}\tau)}{\partial\tau} = e^{\hat{K}_{eff}\tau/\hbar}[\hat{K}, \hat{\Psi}_\uparrow(\mathbf{r})]e^{-\hat{K}_{eff}\tau/\hbar} = -\hat{h}_\uparrow(\mathbf{r})\hat{\Psi}_{K\uparrow}(\mathbf{r}\tau) + \Delta(\mathbf{r})\hat{\Psi}^\dagger_{K\downarrow}(\mathbf{r}\tau), \tag{1.24a}
$$

$$
\hbar\frac{\partial\hat{\Psi}^\dagger_{K\downarrow}(\mathbf{r}\tau)}{\partial\tau} = e^{\hat{K}_{eff}\tau/\hbar}[\hat{K}, \Psi^\dagger_\downarrow(\mathbf{r})]e^{-\hat{K}_{eff}\tau/\hbar} = \hat{h}^*_\downarrow(\mathbf{r})\hat{\Psi}^\dagger_{K\downarrow}(\mathbf{r}\tau) + \Delta^*(\mathbf{r})\hat{\Psi}_{K\uparrow}(\mathbf{r}\tau), \tag{1.24b}
$$

such that the time derivatives of the normal and anomalous Green's functions (1.23) are:

$$
\hbar\frac{\partial\mathcal{G}(\mathbf{r}\tau, \mathbf{r}'\tau')}{\partial\tau} = -\hbar\delta(\tau - \tau')\delta(\mathbf{r} - \mathbf{r}') - \hat{h}_\uparrow(\mathbf{r})\mathcal{G}(\mathbf{r}\tau, \mathbf{r}'\tau') + \Delta(\mathbf{r})\mathcal{F}^\dagger(\mathbf{r}\tau, \mathbf{r}'\tau'), \tag{1.25a}
$$

$$\hbar\frac{\partial\mathcal{F}(\mathbf{r}\tau,\mathbf{r}'\tau')}{\partial\tau} = -\hat{h}_\uparrow(\mathbf{r})\mathcal{F}(\mathbf{r}\tau,\mathbf{r}'\tau') + \Delta(\mathbf{r})\mathcal{G}(\mathbf{r}'\tau',\mathbf{r}\tau), \tag{1.25b}$$

$$\hbar\frac{\partial\mathcal{F}^\dagger(\mathbf{r}t,\mathbf{r}'t')}{\partial t} = \hat{h}^*_\downarrow(\mathbf{r})\mathcal{F}^\dagger(\mathbf{r}\tau,\mathbf{r}'\tau') + \Delta^*(\mathbf{r})\mathcal{G}(\mathbf{r}\tau,\mathbf{r}'\tau'). \tag{1.25c}$$

Since the Hamiltonian $\hat{K}_{eff}$ is time-independent, the Green's functions depend only on $\tau - \tau'$. It is therefore useful to introduce the Fourier representation of the Green's functions

$$\mathcal{G}(\mathbf{r}\tau,\mathbf{r}'\tau') = \frac{1}{\beta\hbar}\sum_n e^{-i\omega_n(\tau-\tau')}\mathcal{G}(\mathbf{r},\mathbf{r}',\omega_n), \tag{1.26a}$$

$$\mathcal{F}^\dagger(\mathbf{r}\tau,\mathbf{r}'\tau') = \frac{1}{\beta\hbar}\sum_n e^{-i\omega_n(\tau-\tau')}\mathcal{F}^\dagger(\mathbf{r},\mathbf{r}',\omega_n), \tag{1.26b}$$

where $\omega_n = (2n+1)\pi/(\beta\hbar)$ to ensure Fermi statistics. The frequencies ω_n are commonly referred to as Matsubara frequencies.

Introducing (1.26) into (1.25) yields the other well-known version of the BdG equations, namely:

$$\begin{pmatrix} i\hbar\omega_n - \hat{h}_\uparrow(\mathbf{r}) & \Delta(\mathbf{r}) \\ \Delta^*(\mathbf{r}) & i\hbar\omega_n + \hat{h}^*_\downarrow(\mathbf{r}) \end{pmatrix}\begin{pmatrix} \mathcal{G}(\mathbf{r},\mathbf{r}',\omega_n) \\ \mathcal{F}^\dagger(\mathbf{r},\mathbf{r}',\omega_n) \end{pmatrix} = \begin{pmatrix} 1 \\ 0 \end{pmatrix}\hbar\delta(\mathbf{r}-\mathbf{r}'), \tag{1.27}$$

where the gap parameter can be cast in terms of the anomalous Green's function as

$$\Delta^*(\mathbf{r}) = g\mathcal{F}(\mathbf{r}\tau^+,\mathbf{r}\tau) = \frac{g}{\beta\hbar}\sum_n e^{-i\omega_n\eta}\mathcal{F}^\dagger(\mathbf{r},\mathbf{r},\omega_n) \quad (\eta\to 0^+). \tag{1.28}$$

Combining eq. (1.9) with eq. (1.16) one sees that the solutions of eqs. (1.16) and (1.27) are related by

$$\begin{pmatrix} \mathcal{G}(\mathbf{r},\mathbf{r}',\omega_n) \\ \mathcal{F}^\dagger(\mathbf{r},\mathbf{r}',\omega_n) \end{pmatrix} = \sum_\nu\left[\frac{1}{i\omega_n - E_\nu/\hbar}\begin{pmatrix} u_{\nu\uparrow}(\mathbf{r})u^*_{\nu\uparrow}(\mathbf{r}') \\ v_{\nu\downarrow}(\mathbf{r})u^*_{\nu\uparrow}(\mathbf{r}') \end{pmatrix} + \frac{1}{i\omega_n + E_\nu/\hbar}\begin{pmatrix} v^*_{\nu\uparrow}(\mathbf{r})v_{\nu\uparrow}(\mathbf{r}') \\ -u^*_{\nu\downarrow}(\mathbf{r})v_{\nu\uparrow}(\mathbf{r}') \end{pmatrix}\right]. \tag{1.29}$$

1.1.5 The time-dependent BdG Equations

In this Subsection we consider a time-dependence of the Hamiltonian (1.1), by allowing the external potential or the interaction constant to vary with time. Performing a mean-field decoupling on this newly defined time-dependent Hamiltonian, we end up with an effective Hamiltonian of the same form of Eq. (1.3), where $V^\sigma_{\text{ext}}(\mathbf{r}) \to V^\sigma_{\text{ext}}(\mathbf{r},t)$ and $\Delta(\mathbf{r}) \to \Delta(\mathbf{r},t)$ is the time-dependent order parameter

$$\Delta(\mathbf{r},t) = g(t)\langle\hat{\Psi}_\downarrow(\mathbf{r})\hat{\Psi}_\uparrow(\mathbf{r})\rangle_t. \tag{1.30}$$

This definition corresponds to (1.4) upon changing $g \to g(t)$ and $\langle\dots\rangle \to \langle\dots\rangle_t$, where the angular brackets denote an ensamble average over the state $|\Phi(t)\rangle$ to be defined in the following.

We assume the time-dependence of the Hamiltonian to begin at a time t_0^+, such that $\hat{K}_{\text{eff}}(t \le t_0) = \hat{K}_{\text{eff}}(t_0) = \hat{K}_{\text{eff}}$ where $\hat{K}_{\text{eff}}$ is defined by eq. (1.3). It results that $|\Phi(t=t_0)\rangle = |\Phi_0\rangle$, where $|\Phi_0\rangle$ is the Bogoliubov vacuum at zero temperature

introduced before (cf. eq. (1.7)). Therefore, the state $|\Phi(t)\rangle$ for $t > t_0$ can be obtained from $|\Phi_0\rangle$ by

$$|\Phi(t)\rangle = \hat{\mathcal{U}}(t, t_0)|\Phi_0\rangle, \tag{1.31}$$

where $\hat{\mathcal{U}}(t, t_0)$ is the evolution operator associated with the time-dependent Hamiltonian $\hat{K}_{\text{eff}}(t)$

$$\hat{\mathcal{U}}(t, t_0) = \hat{T}_D \exp\left[-\frac{i}{\hbar}\int_{t_0}^{t} \hat{K}_{\text{eff}}(t')dt'\right] \tag{1.32}$$

with $\hat{T}_D$ denoting the time-ordering operator.

We assume the state $|\Phi(t)\rangle$ to be still a Bogoliubov vacuum [27], in the sense that

$$\hat{\gamma}_{\nu\alpha}(t)|\Phi(t)\rangle = 0 \qquad (t > t_0), \tag{1.33}$$

where $\hat{\gamma}_{\nu\alpha}(t)$ are a set of time-dependent operators. These operators, following the assumption (1.33), satisfy the relation

$$i\hbar\frac{\partial\hat{\gamma}_{\nu\alpha}(t)}{\partial t} + \left[\hat{\gamma}_{\nu\alpha}(t), \hat{K}_{\text{eff}}(t)\right] = 0. \tag{1.34}$$

Moreover, in the Heisenberg picture, the operators $\gamma_{K\nu\alpha}(t)$ are defined as

$$\hat{\gamma}_{K\nu\alpha}(t) = \mathcal{U}^{\dagger}(t, t_0)\hat{\gamma}_{\nu\alpha}(t)\hat{\mathcal{U}}(t, t_0) \tag{1.35}$$

and obey the following time evolution condition

$$i\hbar\frac{\partial\hat{\gamma}_{K\nu\alpha}(t)}{\partial t} = \mathcal{U}^{\dagger}(t, t_0)\left\{\left[\hat{\gamma}_{\nu\alpha}(t), \hat{K}_{\text{eff}}(t)\right] + i\hbar\frac{\partial\hat{\gamma}_{\nu\alpha}(t)}{\partial t}\right\}\hat{\mathcal{U}}(t, t_0). \tag{1.36}$$

Entering (1.34) into (1.36), we conclude that $\hat{\gamma}_{K\nu\alpha}(t) = \hat{\gamma}_{K\nu\alpha}(t_0) = \hat{\gamma}_{\nu\alpha}(t_0) = \hat{\gamma}_{\nu\alpha}$, where $\hat{\gamma}_{\nu\alpha}$ are the fermionic operators introduced in (1.5).

At this point, following the same procedure used for the diagonalization of the time-indipendent Hamiltonian, we assume that the Heisenberg field operators can be written in terms of $\hat{\gamma}_{\nu\alpha}$ as

$$\begin{pmatrix}\hat{\Psi}_{K\uparrow}(\mathbf{r}, t)\\ \hat{\Psi}^{\dagger}_{K\downarrow}(\mathbf{r}, t)\end{pmatrix} = \sum_{\nu}\begin{pmatrix}u_{\nu\uparrow}(\mathbf{r}, t) & -v^{*}_{\nu\uparrow}(\mathbf{r}, t)\\ v_{\nu\downarrow}(\mathbf{r}, t) & u^{*}_{\nu\downarrow}(\mathbf{r}, t)\end{pmatrix}\begin{pmatrix}\hat{\gamma}_{\nu 1}\\ \hat{\gamma}^{\dagger}_{\nu 2}\end{pmatrix}, \tag{1.37}$$

where $u_{\nu\sigma}(\mathbf{r}, t)$ and $v_{\nu\sigma}(\mathbf{r}, t)$ are complex functions to be dermined. Notice that, in order for the Heisenberg field operators to depend on time, we have assumed that the complex functions $u_{\nu\sigma}$ and $v_{\nu\sigma}$ depend on time.

Entering eq. (1.37) in the equation of motion of the Heisenberg field operators (cf. 1.24 where now $\tau = it$) and equating the coefficients of the $\hat{\gamma}_{\nu\alpha}$, we obtain eventually the time-dependent Bogoliubov-de Gennes (TDBdG) equations:

$$\begin{pmatrix}\hat{h}_{\uparrow}(\mathbf{r}, t) & -\Delta(\mathbf{r}, t)\\ -\Delta^{*}(\mathbf{r}, t) & -\hat{h}^{*}_{\downarrow}(\mathbf{r}, t)\end{pmatrix} = i\hbar\frac{\partial}{\partial t}\begin{pmatrix}u_{\nu\uparrow}(\mathbf{r}, t)\\ v_{\nu\downarrow}(\mathbf{r}, t)\end{pmatrix}. \tag{1.38}$$

Here, the time-dependent gap parameter $\Delta(\mathbf{r}, t)$ can be expressed in terms of $u_{\nu\sigma}(\mathbf{r}, t)$ and $v_{\nu\sigma}(\mathbf{r}, t)$ in the following way:

$$\Delta(\mathbf{r}, t) = -\frac{g(t)}{2}\sum_{\nu}\left[u_{\nu\downarrow}(\mathbf{r}, t)v^{*}_{\nu\uparrow}(\mathbf{r}, t) + u_{\nu\uparrow}(\mathbf{r}, t)v^{*}_{\nu\downarrow}(\mathbf{r}, t)\right]. \tag{1.39}$$

To arrive to this expression, eq. (1.30) was used along with the property

$$\langle\Phi(t)|\hat{\Psi}_{\downarrow}(\mathbf{r})\hat{\Psi}_{\uparrow}(\mathbf{r})|\Phi(t)\rangle = \langle\Phi_0|\hat{\Psi}_{K\downarrow}(\mathbf{r},t)\hat{\Psi}_{K\uparrow}(\mathbf{r},t)|\Phi_0\rangle. \tag{1.40}$$

Other quantities of interest, which can be obtained from $u_{\nu\sigma}(\mathbf{r},t)$ and $v_{\nu\sigma}(\mathbf{r},t)$, are the number density

$$n_\sigma(\mathbf{r},t) = \sum_\nu |v_{\nu\sigma}(\mathbf{r},t)|^2, \tag{1.41a}$$

and the energy of the system

$$E(t) = \int d\mathbf{r} \left\{ \sum_{\nu,\sigma} v_{\nu\sigma}(\mathbf{r},t) \left[\hat{h}_\sigma(\mathbf{r},t) + \mu_\sigma\right] v^*_{\nu\sigma}(\mathbf{r},t) - \frac{1}{g(t)}|\Delta(\mathbf{r},t)|^2 \right\}. \tag{1.41b}$$

1.2 Coarse-graining procedure of the BdG equations

To fully analyse an inhomogeneous superconducting system at any coupling and temperature in terms of the time-independent BdG equations is quite prohibitive except for a few cases. This is because solving eqs. (1.27) along with the self-consistency condition (1.28) (or, equivalently, (1.16) along with (1.21a)) is computationally demanding both in terms of memory space and evaluation time, and possible only for a limited number of relatively simple problems.

More amenable solutions are obtainable in terms of simpler non-linear differential equations, like the Ginzburg-Landau (GL) equation in weak-coupling for $T \lesssim T_C$ and the Gross-Pitaevskii (GP) equation in strong-coupling at $T \approx 0$. However, it is not possible to recover a solution for $\Delta(\mathbf{r})$ along the BCS-BEC crossover at any temperature T. For this reason, many attempts have been made to approximate the BdG equations over wider sectors of temperature-coupling phase diagram. The one used here consists of the coarse graining of the BdG equations considered in [19]. This process is based on the assumption that the local magnitude and phase of the gap parameter $\Delta(\mathbf{r})$ have both smooth spatial variations and allows one to obtain a non-linear differential (local) equation for $\Delta(\mathbf{r})$ which is referred to as LPDA equation. One of the virtues of this equation is that it reduces to the GL and GP equations in the appropriate limits.

In the following, the constants $\hbar$ and e will be set equal to 1, and $(k_F a_F)^{-1}$ will be used as the coupling parameter, where $k_F = (3\pi^2 n)^{1/3}$ is the Fermi wavevector associated with the density n and a_F is the scattering length of the two-fermion problem [28]. This dimensionless coupling parameter ranges from $\ll -1$ in the weak-coupling (BCS) limit to $\gg +1$ in the strong-coupling (BEC) limit, across the unitary limit where $(k_F a_F)^{-1} = 0$. The present work is mainly focused on the region $(k_F a_F)^{-1} \lesssim 0.5$, where the mean-field approach at finite temperature is more reliable than in BEC regime for $(k_F a_F)^{-1} > 0.5$.

1.2.1 The Local Phase Density Approximation of the BdG equations

In [19] spin-balanced populations of interacting fermions subject to both an external potential $V(\mathbf{r})$ and a vector potential $\mathbf{A}(\mathbf{r})$ were considered. In this case, it is useful

to adopt Gorkov's procedure [29] and introduce the non-interacting Green's function $\mathcal{G}_0$ which satisfies the following equations:

$$\left[i\omega_n - \hat{h}(\mathbf{r})\right]\mathcal{G}_0(\mathbf{r},\mathbf{r}',\omega_n) = \delta(\mathbf{r}-\mathbf{r}'), \quad \left[i\omega_n - \hat{h}^*(\mathbf{r})\right]\mathcal{G}_0(\mathbf{r}',\mathbf{r},\omega_n) = \delta(\mathbf{r}-\mathbf{r}'), \tag{1.42}$$

where the spin-dependence has been dropped.

Using the properties of $\mathcal{G}_0$, eqs. (1.27) can be rewritten as

$$\begin{cases} \mathcal{G}(\mathbf{r},\mathbf{r}',\omega_n) = \mathcal{G}_0(\mathbf{r},\mathbf{r}',\omega_n) - \int d\mathbf{r}''\mathcal{G}_0(\mathbf{r},\mathbf{r}'',\omega_n)\Delta(\mathbf{r}'')\mathcal{F}^\dagger(\mathbf{r}'',\mathbf{r}',\omega_n) \\ \mathcal{F}^\dagger(\mathbf{r},\mathbf{r}',\omega_n) = \int d\mathbf{r}''\mathcal{G}_0(\mathbf{r}'',\mathbf{r},-\omega_n)\Delta^*(\mathbf{r}'')\mathcal{G}(\mathbf{r}'',\mathbf{r}',\omega_n), \end{cases} \tag{1.43}$$

while the gap parameter becomes

$$\frac{\Delta^*(\mathbf{r})}{g} = \frac{1}{\beta}\sum_n \int \mathrm{d}\mathbf{r}''\tilde{\mathcal{G}}_0(\mathbf{r}'',\mathbf{r},-\omega_n)\Delta(\mathbf{r}'')\mathcal{G}_{11}(\mathbf{r}'',\mathbf{r},\omega_n). \tag{1.44}$$

The starting assumption of the coarse-graining procedure is the smooth behaviour of the gap parameter, which is explicitly assumed through the subsequent process. The variable $\mathbf{r}''$ is written as $\mathbf{r}'' = \mathbf{R} + \boldsymbol{\tau} + \boldsymbol{\rho}$, where $\mathbf{R}$ and $\boldsymbol{\tau}$ identify the centers of the volume elements (embedded into one another) about which the magnitude $\tilde{\Delta}(\mathbf{R})$ and (the gradient of) the phase $2\mathbf{Q}(\mathbf{R},\boldsymbol{\tau})$ of the gap are considered to be approximately constant (cf. fig. 1.1). As a consequence, the spatial behaviour of the gap parameter can be approximated as:

$$\Delta(\mathbf{r}'') \backsimeq \tilde{\Delta}(\mathbf{R})\mathrm{e}^{2i\mathbf{Q}(\mathbf{R},\boldsymbol{\tau})\cdot(\mathbf{R}+\boldsymbol{\tau}+\boldsymbol{\rho})}. \tag{1.45}$$

Moreover, assuming that the volume element centered at $\mathbf{R}+\boldsymbol{\tau}$ is close to the variable $\mathbf{r}$, performing further approximations (among which a (local) eikonal approximation of $\mathcal{G}_0(\mathbf{r}'',\mathbf{r},-\omega_n)$), and using a standard regularization procedure to eliminate g in favour of a_F, the gap equation can be rewritten as

$$-\frac{m}{4\pi a_F}\Delta(\mathbf{R}) = \int \mathrm{d}\mathbf{R}\Delta(\mathbf{R})\int \frac{\mathrm{d}\mathbf{Q}}{\pi^3}\mathrm{e}^{2i\mathbf{Q}\cdot(\mathbf{r}-\mathbf{R})}K^{\mathbf{A}}(\mathbf{Q}|\mathbf{r}), \tag{1.46}$$

where the kernel $K^{\mathbf{A}}(\mathbf{Q}|\mathbf{r})$ is defined by

$$K^{\mathbf{A}}(\mathbf{Q}|\mathbf{r}) \equiv \int \frac{\mathrm{d}\mathbf{k}}{(2\pi)^3}\left[\frac{1-2f_F(E_+^{\mathbf{A}}(\mathbf{k},\mathbf{Q}|\mathbf{r}))}{2E^{\mathbf{A}}(\mathbf{k},\mathbf{Q}|\mathbf{r})} - \frac{m}{\mathbf{k}^2}\right], \tag{1.47}$$

with

$$E_\pm^{\mathbf{A}}(\mathbf{k},\mathbf{Q}) \equiv \sqrt{\left(\frac{\mathbf{k}^2}{2m}+\frac{\mathbf{Q}^2}{2m}-\bar{\mu}-\frac{\mathbf{A}}{m}\cdot\mathbf{Q}\right)^2 + \tilde{\Delta}^2} \pm \frac{\mathbf{k}}{m}\cdot(\mathbf{Q}-\mathbf{A}), \tag{1.48a}$$

$$2E^{\mathbf{A}}(\mathbf{k},\mathbf{Q}) \equiv E_+^{\mathbf{A}}(\mathbf{k},\mathbf{Q}) + E_-^{\mathbf{A}}(\mathbf{k},\mathbf{Q}). \tag{1.48b}$$

The local chemical potential $\bar{\mu}(\mathbf{r}) \equiv \mu - V(\mathbf{r}) - \mathbf{A}^2(\mathbf{r})/(2m)$ has also been introduced for convenience.

Expanding the kernel (cf. eq. (1.47)) in powers of $\mathbf{Q}$ and integrating over $\mathbf{R}$, the following non-linear (local) differential equation is eventually obtained:

$$-\frac{m}{4\pi a_F}\Delta(\mathbf{r}) = \mathcal{I}_0(\mathbf{r})\Delta(\mathbf{r}) + \mathcal{I}_1(\mathbf{r})\frac{\nabla^2}{4m}\Delta(\mathbf{r}) - \mathcal{I}_1(\mathbf{r})i\frac{\mathbf{A}(\mathbf{r})}{m}\cdot\nabla\Delta(\mathbf{r}), \tag{1.49}$$

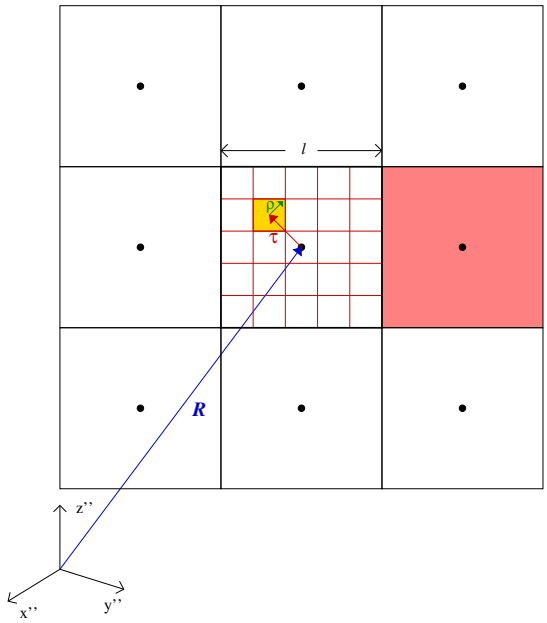

Figure 1.1: Double coarse graining procedure. The magnitude $\tilde{\Delta}(\mathbf{R})$ of the gap parameter is considered to be (approximately) constant in the volume of side l centered at $\mathbf{R}$. The (gradient of the) phase $2\mathbf{Q}(\mathbf{R},\tau)$ of the gap parameter is considered to be (approximately) constant in the smaller volumes centered at $\mathbf{R}+\tau$ embedded in the bigger ones [Figure taken from [19]].

with the notation

$$\mathcal{I}_0(\mathbf{r}) \equiv \int \frac{\mathrm{d}\mathbf{k}}{(2\pi)^3}\left[\frac{1-2f_F(E_+^{\mathbf{A}}(\mathbf{k}|\mathbf{r}))}{2E(\mathbf{k}|\mathbf{r})}-\frac{m}{\mathbf{k}^2}\right], \tag{1.50a}$$

$$\begin{aligned}\mathcal{I}_1(\mathbf{r}) \equiv \frac{1}{2}\int \frac{\mathrm{d}\mathbf{k}}{(2\pi)^3}\Bigg\{&\frac{\xi(\mathbf{k}|\mathbf{r})}{2E(\mathbf{k}|\mathbf{r})^3}[1-2f_F(E_+^{\mathbf{A}}(\mathbf{k}|\mathbf{r}))]+\\ &+\frac{\xi(\mathbf{k}|\mathbf{r})}{2E(\mathbf{k}|\mathbf{r})^2}\frac{\partial f_F(E_+^{\mathbf{A}}(\mathbf{k}|\mathbf{r}))}{\partial E_+^{\mathbf{A}}(\mathbf{k}|\mathbf{r})}-\frac{\mathbf{k}\cdot\mathbf{A}(\mathbf{r})}{\mathbf{A}(\mathbf{r})^2}\frac{1}{E(\mathbf{k}|\mathbf{r})}\frac{\partial f_F(E_+^{\mathbf{A}}(\mathbf{k}|\mathbf{r}))}{\partial E_+^{\mathbf{A}}(\mathbf{k}|\mathbf{r})}\Bigg\},\end{aligned} \tag{1.50b}$$

where

$$\begin{aligned}\xi(\mathbf{k}|\mathbf{r}) &= \frac{\mathbf{k}^2}{2m}-\bar{\mu}(\mathbf{r}),\\ E(\mathbf{k}|\mathbf{r}) &= \sqrt{\xi(\mathbf{k}|\mathbf{r})^2+|\Delta(\mathbf{r})|^2},\\ E_+^{\mathbf{A}}(\mathbf{k}|\mathbf{r}) &= E(\mathbf{k}|\mathbf{r})-\frac{\mathbf{k}\cdot\mathbf{A}(\mathbf{r})}{m}.\end{aligned} \tag{1.51}$$

The remarkable aspect of the above equation, referred to as a Local Phase Density Approximation (LPDA) of the BdG equations, is that *it should hold with no a priori restrictions on coupling and temperature regimes, provided that* $\Delta(\mathbf{r})$ *varies slowly enough with its magnitude varying more slowly than its phase.* In addition, as already mentioned, the LPDA equation reduces to the GL and GP equations in the appropriate limits.

To test its validity in [19], eq. (1.49) has been applied to the non-trivial case of an isolated vortex embedded in a infinite medium. The obtained gap parameter profile is in good agreement with the corresponding solution of the BdG equations (see fig. 2 of [19]), and this appears especially remarkable in the light of the huge reduction of computational time: a few seconds against a whole day. The larger deviations, albeit still rather small, occur in the BCS regime at low temperature. This discrepancy has been attributed to the spatial range of the kernel (of the order of the size of the fermion pairs at low temperature) which in that limit is comparable with the range of the gap parameter itself. Indeed further studies on the subject have lead to the conclusion that the granularity scale resulting from the double-coarse graining procedure discussed above is given by the Cooper pair size [30].

1.2.2 LPDA equation in the presence of a supercurrent

For later convenience, it is useful to introduce the expressions of the density $n(\mathbf{r})$ and the supercurrent $j(\mathbf{r})$ consistent with the LPDA approach when dealing with a neutral Fermi gas.

In this case, $\mathbf{A}(\mathbf{r})$ plays formally the role of an "effective" vector potential, and its physical meaning differs from that of vector potential in classical electrodynamics. In the presence of a flowing supercurrent J, $\mathbf{A}(\mathbf{r})$ is identified with a constant wavevector $-\mathbf{Q}_0$ such that at zero temperature $J = Q_0 n/m$ [9], with $Q_0 = |\mathbf{Q}_0|$, n being the number density and m the fermionic mass. In addition for the present system the superfluid gap parameter solution of eq. (1.49) can be written as

$$\Delta(\mathbf{r}) = |\Delta(\mathbf{r})| e^{i\varphi(\mathbf{r})}, \text{ where } \varphi(\mathbf{r}) = 2\mathbf{Q}_0 \cdot \mathbf{r} + 2\phi(\mathbf{r}). \tag{1.52}$$

Consistently with the LPDA approach, we take the (coarse-grained) local current of the form

$$\mathbf{j}(\mathbf{r}) = \frac{1}{m} \left(\nabla\phi(\mathbf{r}) + \mathbf{Q}_0\right) n(\mathbf{r}) + 2 \int \frac{d\mathbf{k}}{(2\pi)^3} \frac{\mathbf{k}}{m} f_F \left(E_+^{\mathbf{Q}_0}(\mathbf{k}|\mathbf{r}) \right), \tag{1.53}$$

where

$$n(\mathbf{r}) = \int \frac{d\mathbf{k}}{(2\pi)^3} \left\{ 1 - \frac{\xi^{\mathbf{Q}_0}(\mathbf{k}|\mathbf{r})}{E^{\mathbf{Q}_0}(\mathbf{k}|\mathbf{r})} \left[1 - 2 f_F(E_+^{\mathbf{Q}_0}(\mathbf{k}|\mathbf{r})) \right] \right\} \tag{1.54}$$

is the corresponding local number density, and

$$\begin{aligned} \xi^{\mathbf{Q_0}}(\mathbf{k}|\mathbf{r}) &= \frac{\mathbf{k}^2}{2m} - \mu(\mathbf{r}) + \frac{1}{2m} \left(\nabla\phi(\mathbf{r}) + \mathbf{Q}_0\right)^2, \\ E^{\mathbf{Q}_0}(\mathbf{k}|\mathbf{r}) &= \sqrt{\xi^{\mathbf{Q}_0}(\mathbf{k}|\mathbf{r})^2 + |\Delta(\mathbf{r})|^2}, \\ E_+^{\mathbf{Q}_0}(\mathbf{k}|\mathbf{r}) &= E^{\mathbf{Q}_0}(\mathbf{k}|\mathbf{r}) + \frac{\mathbf{k}}{m} \cdot \left(\nabla\phi(\mathbf{r}) + \mathbf{Q}_0\right), \end{aligned} \tag{1.55}$$

with $\mu(\mathbf{r}) = \mu - V(\mathbf{r})$.

Note that at $T = 0$ the local current (1.53) with $\nabla\phi = 0$ coincides with $\mathbf{Q}_0 n/m$ provided the integral contribution vanishes. This is the case as far as the argument of the Fermi function remains positive for all $\mathbf{k}$, while violation of this condition corresponds to the Landau criterion for the collapse of superfluidity [31] when the relevant quasi-particle exitations consist of pair-breaking excitations.

1.2.3 Recovering the GL and GP equations

For later convenience, it is useful to determine how the GL and GP equations are recovered from the LPDA equation in the appropriate limits.

In the weak-coupling limit $(k_F a_F)^{-1} \ll 1$ and at temperature close to T_c, we can approximate $E(\mathbf{k}|\mathbf{r}) \cong |\xi(\mathbf{k}|\mathbf{r})|$ (see Eq. (1.51)) and neglect all integrands in Eqs. (1.50) which are odd in $\xi(\mathbf{k}|\mathbf{r})$. Moreover, using the BCS equation for T_c and assuming $\mathbf{A}(\mathbf{r})$ to be small enough, we obtain:

$$\begin{aligned}\mathcal{I}_0(\mathbf{r}) \cong -\frac{m}{4\pi a_F} + N_0 \left[\left(1-\frac{T}{T_c}\right) - \left(1-\frac{\pi}{4k_F a_F}\right)\frac{V_{ext}(\mathbf{r})}{E_F}\right] \\ -N_0 \frac{7\zeta(3)}{8\pi^2 (k_B T_c)^2}|\Delta(\mathbf{r})|^2 - \frac{\mathbf{A}(\mathbf{r})^2}{m}\mathcal{I}_1(\mathbf{r}),\end{aligned} \tag{1.56a}$$

$$\mathcal{I}_1(\mathbf{r}) \cong N_0 \frac{7\zeta(3) E_F}{6\pi^2 (k_B T_c)^2}, \tag{1.56b}$$

where $\zeta(3) \simeq 1.202$ is the Riemann ζ function of argument 3 and $N_0 = m k_F/(2\pi^2)$ is the density of states at the Fermi level per spin components. Introducing Eqs. (1.56) into Eq. (1.49), we get

$$\begin{aligned}\frac{(i\nabla + 2\mathbf{A}(\mathbf{r}))^2}{4m}\Delta(\mathbf{r}) + \frac{3}{4E_F}|\Delta(\mathbf{r})|^2\Delta(\mathbf{r}) \\ + \frac{6\pi^2 (k_B T_c)^2}{7\zeta(3) E_F}\left[\left(1-\frac{\pi}{4k_F a_F}\right)\frac{V_{ext}(\mathbf{r})}{E_F} - \left(1-\frac{T}{T_c}\right)\right]\Delta(\mathbf{r}) = 0,\end{aligned} \tag{1.57}$$

that is the Ginzburg-Landau equation in the presence of an external potential [32].

In the case of a supercurrent flow, the vector potential $\mathbf{A}(\mathbf{r})$ will be replaced by $-\mathbf{Q_0}$ in Eq. (1.57) and the current becomes to the lowest-order in $|\Delta(\mathbf{r}|^2$:

$$j_{GL}(\mathbf{r}) \simeq \frac{1}{m}\left(\nabla\phi(\mathbf{r}) + \mathbf{Q}_0\right)\frac{7\zeta(3) n}{8\pi^2 (k_B T_c)^2}|\Delta(\mathbf{r})|^2. \tag{1.58}$$

On the other hand, when $(k_F a_F)^{-1} \gg 1$ and $T = 0$ the largest energy scale is given by the two-body binding energy $\epsilon_0 = 1/(m a_F)^2 = -2\mu + \mu_B$, where μ_B is the residual chemical potential of the composite bosons that form in this limit. Expanding Eqs (1.50) in terms of the small parameter $\Delta(\mathbf{r})/|\mu|$, we obtain to the leading orders:

$$\mathcal{I}_0 = -\frac{m}{4\pi a_F} + \frac{m^2 a_F}{8\pi}\left[\mu_B - 2V_{ext}(\mathbf{r}) - \frac{m a_F^2}{2\pi}|\Delta(\mathbf{r})|^2\right], \tag{1.59a}$$

$$\mathcal{I}_1 = \frac{m^2 a_F}{8\pi}. \tag{1.59b}$$

Introducing Eqs. (1.59) into Eq. (1.49) we get eventually

$$\frac{(i\nabla + 2\mathbf{A}(\mathbf{r}))^2}{4m}\Delta(\mathbf{r}) + 2V_{ext}(\mathbf{r})\Delta(\mathbf{r}) + \frac{m a_F^2}{2}|\Delta(\mathbf{r})|^2\Delta(\mathbf{r}) - \mu_B\Delta(\mathbf{r}) = 0, \tag{1.60}$$

which coincide with the Gross-Pitaevskii equation for composite bosons (dimers).

In the case of a supercurrent flow $\mathbf{A}(\mathbf{r}) = -\mathbf{Q}_0$ and the current to the lowest order in $|\Delta(\mathbf{r})|^2$ is given by

$$j_{GP}(\mathbf{r}) \simeq \frac{1}{m}\left(\nabla\phi(\mathbf{r}) + \mathbf{Q}_0\right)\frac{m^2 a_F}{4\pi}|\Delta(\mathbf{r})|^2. \tag{1.61}$$

Chapter 2

Josephson Effect at finite Temperature

2.1 Geometry of the physical system

In order to study the stationary Josephson effect, we have considered a potential barrier embedded in an otherwise homogeneous superfluid extending to infinity (SS'S junction). This system was already studied in [9] and is similar to the experimental setup utilized for ultracold quantum gases [3, 4].

Identifying with $\hat{\mathbf{x}}$ the direction of the current flow, the external potential that will be mostly used in the following takes the form

$$V_{ext}(x,y,z) = \begin{cases} V_0 & \text{for } x \leq L/2, \\ 0 & \text{for } x > L/2, \end{cases} \tag{2.1}$$

where V_0 and L are the height and width of a rectangular barrier centered at $x = 0$, respectively. We are assuming the barrier to be homogeneous along $\hat{\mathbf{y}}$ and $\hat{\mathbf{z}}$, the orthogonal directions to the current flow, in order to simplify the numerical calculations.

The barrier plays the role of the weak-link needed to observe the DC Josephson effect and allow us to study high-transparency and low-transparency regimes by varying the height V_0.

Quite generally, in correspondence of the barrier the magnitude of the gap parameter has a depression and recovers its bulk value away from it. Moreover, when a supercurrent flow is imposed, the phase $2\phi(\mathbf{r})$ introduced in (1.52) has the typical profile shown in fig. 2.1: It varies smoothly between the asymptotic values $2\phi(+\infty) = -2\phi(-\infty) = \delta\phi/2$ and its rate of change is maximum in the region of the barrier.

Following a standard procedure when solving the GL equation, in the numerical calculations the imaginary part of the LPDA equation (1.49) has been replaced by the current conservation

$$|j(\mathbf{r})| = J, \tag{2.2}$$

where $j(\mathbf{r})$ is given by eq. (1.53).

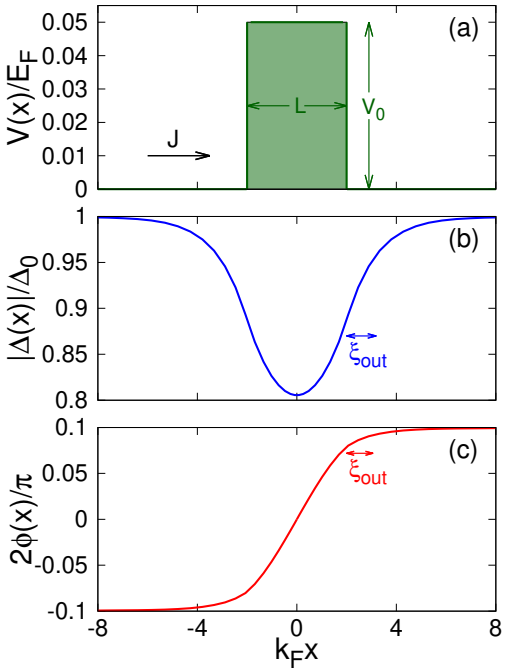

Figure 2.1: (a) Rectangular shape of the potential barrier of height V_0 and width L, on which the stationary supercurrent impinges from the left. Profiles (obtained at unitarity and for $T/T_c = 0.5$) of the (b) magnitude and (c) phase of the gap parameter due to the presence of the barrier, which approach their bulk values Δ_0 and $\delta\phi/2$, respectively, over the distance ξ_{out}. Here, k_F is the Fermi wavevector and $E_F = k_F^2/(2m)$ the corresponding Fermi energy. (Reproduced from Ref. [33].)

2.2 Current vs Phase Josephson Characteristics

One of the main results obtained in the original paper by Josephson [1], later confirmed for fermionic systems [12], was the shape of current-vs-phase characteristic for an insulating (low-transparency) barrier: $J = J_c \sin(\delta\phi)$, where J_c is the critical current above which superfluidity is destroyed. This result has been generalized to different kind of weak links and can be rephrased more generally as $J = J_c f(\delta\phi)$ where f is a periodic function with $f(0) = f(\pi) = 0$ [15].

In the following we shall assume that current-vs-phase numerical characteristics have the shape described by

$$f(\delta\phi) = \frac{A \sin(\delta\phi)}{\sqrt{1 + B \sin^2(\delta\phi/2)}}, \tag{2.3}$$

where A and B are (dimensionless) parameters which depend on the barrier height as well as on coupling and temperature. An expression of the type of (2.3) was obtained for delta-like barriers in the BCS limit at any temperature [34] and recovers both the Ambeagokar-Baratoff result for low-transparency barriers [11] and the Aslamazov-Larkin study for sufficiently thin barriers near T_c [35]. In Ref. [9] an expression similar to eq. (2.3) was analitically derived for delta-like barriers at $T = 0$ and we have proven that it fits rather well all mean-field chracteristics obtained in [9] at $T = 0$ for various couplings and barrier heights and widths (see fig. 2.2).

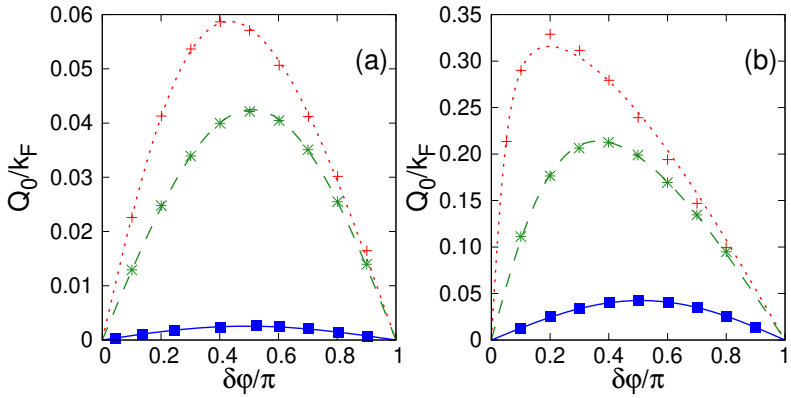

Figure 2.2: Josephson characteristics for a rectangular barrier of width $Lk_F = 4$ and various height V_0/E_F (in units of the Fermi energy $E_F = k_F^2/(2m)$), where the values of Q_0/k_F obtained in Ref. [9] by solving the BdG equations at zero temperature for various couplings (symbols) are compared with the fits obtained by Eq. (2.3) (lines). In (a) $V_0/E_F = 0.4$, with $(k_F a_F)^{-1} = -1$ (crosses and dotted line) where $A = 0.074$ and $B = 1.3$, $(k_F a_F)^{-1} = 0$ (stars and dashed line) where $A = 0.0412$ and $B = -0.11$, and $(k_F a_F)^{-1} = +1.5$ (squares and full line) where $A = 0.00261$ and $B = 0.1$.In (b) $(k_F a_F)^{-1} = 0$, with $V_0/E_F = 0.025$ (crosses and dotted line) where $A = 1.72$ and $B = 96$,$V_0/E_F = 0.1$ (stars and dashed line) where $A = 0.367$ and $B = 4.9$, and $V_0/E_F = 0.4$ (squares and full line) where $A = 0.0412$ and $B = -0.11$. (Reproduced from Ref. [33].)

The expression (2.3) plays an important role in the present study of the DC Josephson effect. This is because the LPDA approach is expected to give reliable results when the spatial variation of the magnitude and phase of the gap parameter are sufficiently smooth. However, for increasing $\delta\phi$ the variations of both $|\Delta(x)|$ and $2\phi(x)$ are expected to be more sharp, such that LPDA approach may fail for $\delta\phi_{max} < \pi$ and we may be able to draw only an arc of the Josephson characteristic. When this occurs, we will use eq. (2.3) to extrapolate the remaining part of the curve. In this context, we expect $\delta\phi_{max}$ to be smaller for decreasing coupling at low temperature (for the intrinsic limits of LPDA approach explained in the subsection 1.2.1), and larger for increasing temperature due to the fact that the healing length, which describes the length scale over which the gap parameter recovers its bulk value (see fig. 2.1), is an increasing function of the temperature [36].

In addition, eq. (2.3) recovers the standard sinusoidal Josephson relation when $B = 0$, while it reduces to $(2A/\sqrt{B})\cos(\delta\phi/2)$ when $B \gg 1$ and to $2A\sin(\delta\phi/2)$ when $B \to -1$, which correspond to the different limiting situations highlighted in [9]. The maximum value of eq. (2.3) for an arbitrary value of $B \in [-1, +\infty)$ occurs at

$$\delta\phi = \arccos\left(\frac{2 + B - 2\sqrt{1+B}}{B}\right). \tag{2.4}$$

Figure 2.3 shows the Josephson characteristics for different temperatures and couplings. In particular, panel(a) shows how the current-vs-phase characteristics evolve for increasing temperature[1] at fixed coupling, while panel(c) shows how the

[1]The temperature range $[0.5, 0.9]T_c$ used in Fig. 2.3 was chosen because it allowed the numerical

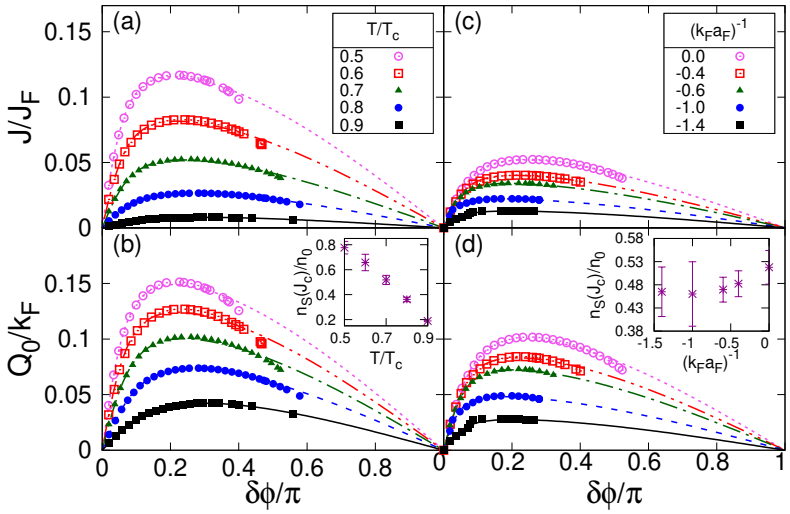

Figure 2.3: The Josephson characteristics for the current J (in units of $J_F = k_F n/m$) (top panels) are compared with those for the wave vector $Q_0 = |\mathbf{Q}_0|$ (in units of k_F) (bottom panels), for a barrier of height $V_0/E_F = 0.05$ and width $k_F L = 3$. The left panels show the dependence of the Josephson characteristics on temperature for $(k_F a_F)^{-1} = 0$, while the right panels show their dependence on coupling for $T/T_c = 0.7$. The insets in the lower panels show the temperature and coupling dependence of n_s/n (see the text). (Reproduced from Ref. [33].)

shape of $J(\delta\phi)$ changes for different couplings at fixed temperature. Looking at panel(a) we notice that the maximum value of the current J_c decreases for increasing temperature with the position of the maximum approaching the value of $\pi/2$ for $T \to T_c^-$. In other words, for increasing temperature the Josephson characteristic approaches the typical sinusoidal shape ($B \to 0$). Looking at panel (c), we notice that J_c decreases upon approaching the BCS side of the crossover with the position of the maximum moving to the left for fixed temperature.

Panel (b) and panel (d) show instead the dependence of $Q_0 = |\mathbf{Q}_0|$ (which enters eq. (1.53)) on $\delta\phi$ for various temperatures at fixed coupling and for different couplings at fixed temperature, respectively. In particular, from the comparison between the top and the bottom panels of fig. 2.3, we can evaluate the superfluid density. This is because eq. (1.53) can be cast in the form

$$\mathbf{j}(\mathbf{r}) = \frac{1}{m}\left[\nabla\phi(\mathbf{r}) + \mathbf{Q}_0\right] n_s(\mathbf{r}), \tag{2.5}$$

where n_s is the local superfluid density. Away from the barrier, the result $J_c/J_F = Q_0 n_s/k_F n$ implies that at $T = 0$ $n_s = n$ for any coupling. At finite temperature on the other hand, from eq. (1.53) we expect $J/J_F < Q_0/k_F$ such that $n_s < n$ where n_s depends on Q_0. The insets in the bottom panels of fig. 2.3 show the ratio n_s/n obtained in correspondence to the maximum of the Josephson characteristics.

integration of LPDA equation up to $\delta\phi_{\rm MAX}$ larger than the critical current abscissa. At lower temperatures, we may need eq. (2.3) to extrapolate the value of J_c and its abscissa. We verified that at $T = 0$, for given coupling and barrier geometry, the branches of the characteristics we obtain by solving the LPDA equation perfectly match the characteristics shown in Ref. [9], where the BdG equations at $T = 0$ were numerically solved.

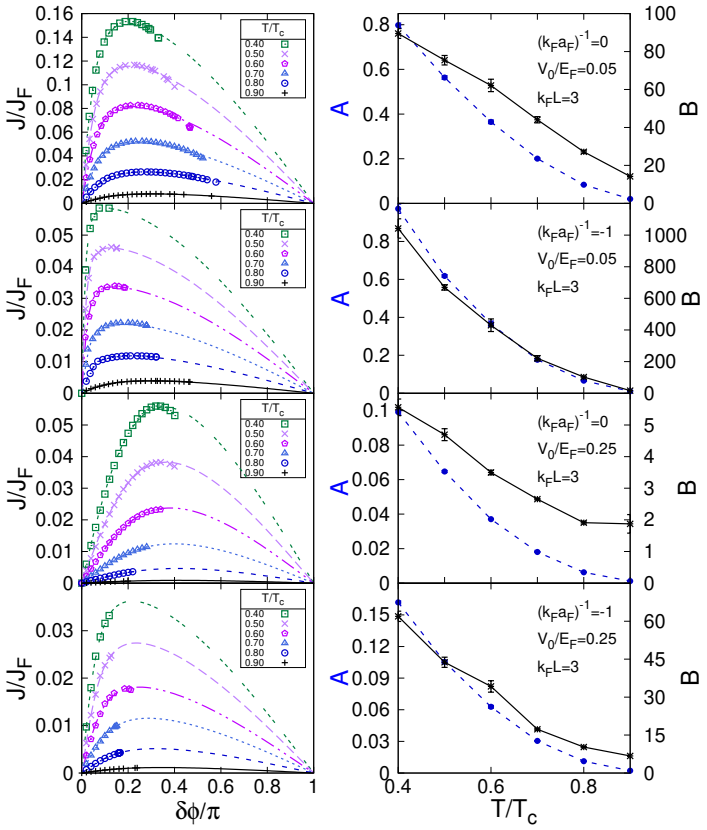

Figure 2.4: Left panels: Temperature dependence of the Josephson characteristics for the couplings $(k_F a_F)^{-1} = 0$ and $(k_F a_F)^{-1} = -1$, with two rectangular barriers of heights $V_0/E_F = (0.05, 0.25)$ and width $k_F L = 3$. Right panels: Corresponding temperature dependence of the coefficients A (dots) and B (stars) of the expression (2.3) used to fit the corresponding Josephson characteristics in the left panels. The values of coupling, barrier height, and width reported in the right panels refer also the left panels. (Reproduced from Ref. [33].)

In particular, the inset in panel (c) shows that, for increasing temperature, the superfluid density decreases, while the inset of panel (d) shows that the superfluid density increases as the unitary limit is approached from the BCS side.

In fig. 2.4 the current-vs-phase characteristics are shown when $(k_F a_F)^{-1} = -1$ and $(k_F a_F)^{-1} = 0$ for two different barrier heights, in order to allow for a clear comparison between the BCS and the crossover regimes. The panels on the right show the corresponding fitting parameters (see eq. (2.3)). We notice that, for both barrier heights and any temperature, $J(\delta\phi)$ has a steeper dependence on the phase difference for $\delta\phi/\pi \lesssim 0.1$ for $(k_F a_F)^{-1} = -1$, which is reflected on the fitting parameter B that results to be an order of magnitude larger in the BCS regime than at unitarity. At the same time the fitting parameter A is comparable in the two cases.

Since the shape of the characteristics is deeply affected by the height and width of the potential barrier, we studied how $J(\delta\phi)$ and $Q_0(\delta\phi)$ change at fixed temperature and coupling for varying barrier heights and widths. The main results of this analysis are reported in Fig. 2.5. In the left panels, we see that, at fixed coupling and for a

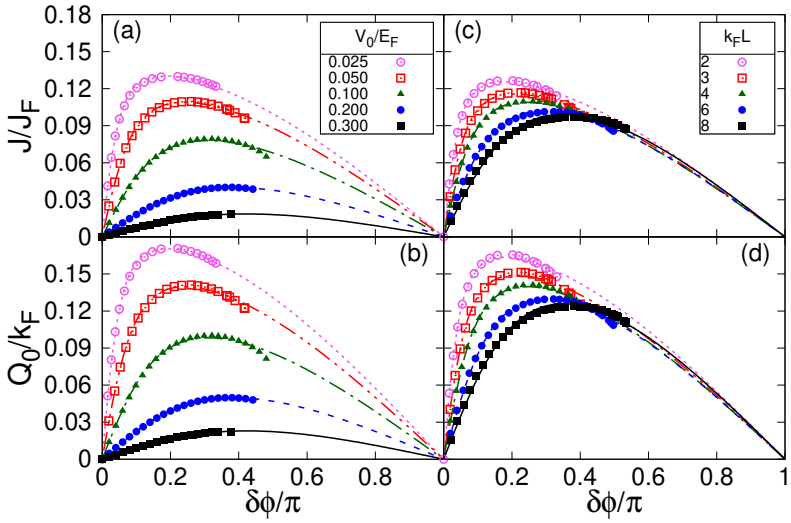

Figure 2.5: The Josephson characteristics for the current J (in units of J_F) (top panels) are compared with those for the wave vector $Q_0 = |\mathbf{Q}_0|$ (in units of k_F) (bottom panels) for $T/T_c = 0.5$ and $(k_F a_F)^{-1} = 0$, for barriers with several heights and widths. In particular, the left panels show the dependence of the Josephson characteristics on the height V_0/E_F when $k_F L = 4$, while the right panels show their dependence on $k_F L$ for $V_0/E_F = 0.05$. (Reproduced from Ref. [33].)

temperature sufficiently smaller than T_c, the characteristics for $V_0 \ll E_F$ approach the shape $\cos(\delta\phi/2)$, while for increasing V_0 they recover the typical $\sin(\delta\phi)$ relation. We point out that this behaviour is observable only at small enough barrier widths, because for increasing barrier widths additional effects may play an important role as it will be highlighted in Section 2.4. Another effect of the increasing barrier height is the suppression of the maximum value of the current J_c (this aspect will be studied in details in the following).

Looking at the right panels of Fig. 2.5 we see that at fixed coupling, temperature, and barrier height, the chacteristics shift the abscissa of their maximum to the right for increasing L. Moreover, the value J_c, after an initial decrease, seems to reach an asymptotic finite value. This feature was already observed in [37] and will be discussed in details in Section 2.4.

2.3 Spatial profiles of the magnitude and phase of the gap parameter

In this section, we study the profiles of the magnitude and phase of the gap parameter which is solution to the LPDA equation. Because of the geometry of the system (see Section 2.1), $|\Delta(x)|$ is an even function about $x = 0$, while $2\phi(x)$ is odd[2] about the same point. For these reasons, we will show the profiles only in the region $x > 0$.

In fig. 2.6 we show the profiles of the magnitude [panel (a)] and phase [panel (b)] of the gap parameter which are solutions of the LPDA equation for different temperatures at unitarity and at fixed $\delta\phi$. Looking at both panels, we see how the

[2]provided that $\phi(x = 0) = 0$

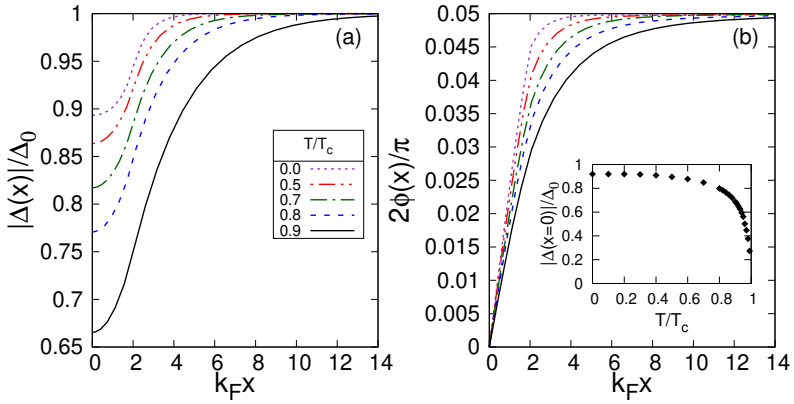

Figure 2.6: Spatial profiles of (a) $|\Delta(x)|$ (in units of the bulk value Δ_0 at the given temperature in the presence of the current) and (b) $2\phi(x)$, for $(k_F a_F)^{-1} = 0$ and several temperatures in the interval $0 \leq T/T_c \leq 0.9$. The barrier has height $V_0/E_F = 0.05$ and width $k_F L = 4$, and the value $\delta\phi/\pi = 0.10$ is kept fixed for all profiles. Symbols are common to both panels. The inset shows the temperature dependence of $|\Delta(x = 0)|/\Delta_0$ when T approaches T_c. (Reproduced from Ref. [33].)

spread of the profiles increases for increasing temperature, which implies an increase on the healing length ξ_{out} (already represented in fig. 2.1) as expected. Moreover, looking at panel (a) we notice that for increasing temperature the normalized value $|\Delta(x = 0)|/\Delta_0$ (where Δ_0 is the bulk gap value) decreases. In the inset of panel (b), this ratio is shown to be a decreasing function of temperature approaching 0 for $T \to T_c^-$. These features, which we are showing only at unitarity and for a particular choice of height and width of the barrier, are found to be common to all the profiles obtained at $-1.5 < (k_F a_F)^{-1} < 0$ and for any choice of V_0 and L.

In fig. 2.7 we show the profiles of the magnitude and phase of the gap parameter solution of the LPDA equation at fixed temperature and $\delta\phi$ for different couplings for a common barrier. Looking at both panels we see that the spread of the profiles increases going to the BCS side of the crossover, as expected from the calculation of the healing length given in [36]. Moreover, looking at panel (a) of fig. 2.7, we notice that the dimensionless ratio $\Delta(x = 0)/\Delta_0$ decreases approaching the unitarity limit and that all profiles have a common point at $x \gtrsim L/2$ in correspondence to which we observe a change of curvature. These features, shown for a fixed value of temperature, are found to be common to all profiles obtained within the temperature-coupling phase diagram where the LPDA (mean-field) approach is expected to be applied with confidence (namely, $0.3 \lesssim T/T_c$ and $-1 \lesssim (k_F a_F)^{-1} \lesssim 0$), since in this range the temperatures of pair formation and condensation about coincide.

The profiles of the magnitude and phase of the gap parameter solution of the LPDA equation depend also on the barrier height and width, as shown in Figs. 2.8 and 2.9, respectively, for the case of unitarity, $T/T_c = 0.5$, and $\delta\phi/\pi = 0.1$. In fig. 2.8 we see that the major effect of increasing the barrier height is to reduce the dimensionless ratio $|\Delta(x = 0)|/\Delta_0$. Looking at fig. 2.9, we notice that the dimensionless ratio $|\Delta(x = 0)|/\Delta_0$ appears to be almost unaffected by the change of the barrier width L. This width has instead an important influence on the spread of both the magnitude and phase profiles of the gap parameter, as can be seen in panel (a) and (b), respectively. Moreover, for large enough L the gap inside the

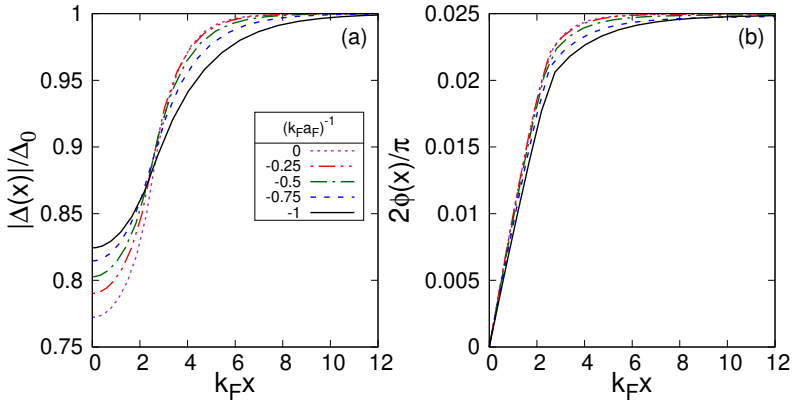

Figure 2.7: Spatial profiles of (a) $|\Delta(x)|$ (in units Δ_0) and (b) $2\phi(x)$, for $T/T_c = 0.5$ and several couplings on the BCS side of unitarity. The barrier has height $V_0/E_F = 0.1$ and width $k_F L = 5$, and the value $\delta\phi/\pi = 0.05$ is kept fixed for all profiles. Symbols are common to both panels. (Reproduced from Ref. [33].)

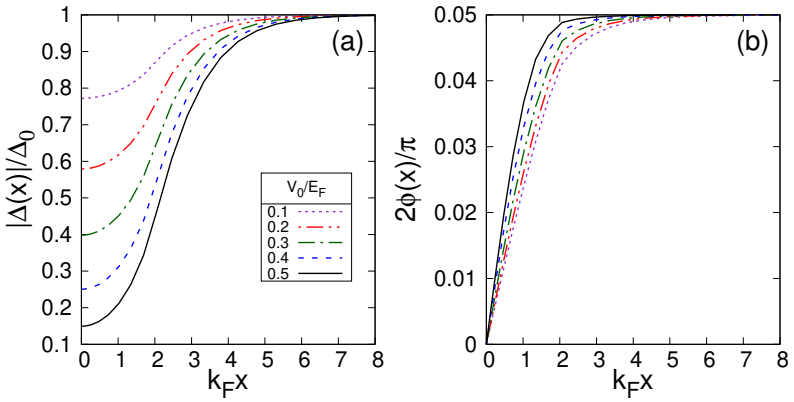

Figure 2.8: Spatial profiles of (a) $|\Delta(x)|$ (in units of Δ_0) and (b) $2\phi(x)$, for a barrier of width $k_F L = 4$ and several heights $V_0/E_F = (0.1, 0.2, 0.3, 0.4, 0.5)$. Here, $(k_F a_F)^{-1} = 0$ and $T/T_c = 0.5$, while the value $\delta\phi/\pi = 0.1$ is kept fixed in all profiles. Symbols are common to both panels. (Reproduced from Ref. [33].)

barrier turns out to be essentially flat. This could be interpreted as the emergence of a "mini-gap" in this region (see Section 2.4 for further details).

Regarding the profiles of the magnitude and phase of the gap parameter, we have often mentioned their spread and how this is affected by the temperature, coupling, and barrier characterstics. In order to quantitatively study this dependence, we have extracted from the gap profiles the healing length $\xi_{\rm out}$, that describes the length scale over which the gap recovers its bulk value, through a fitting procedure of the type:

$$|\Delta(x)|/\Delta_0 = 1 - C_{out} e^{-(x-L/2)/\xi_{\rm out}} \qquad \text{for} \quad x \gtrsim L/2, \tag{2.6}$$

in terms of the parameters C_{out} and $\xi_{\rm out}$. The fitting region has been restricted to $x \gtrsim L/2$ because of the change of curvature of the profiles of the magnitude of the gap parameter mentioned while commenting Fig. 2.7.

In fig. 2.10 the results for $\xi_{\rm out}$ obtained in this way are reported as a function of temperature, for $(k_F a_F)^{-1} = 0$ (top panels) and $(k_F a_F)^{-1} = -1$ (bottom panels),

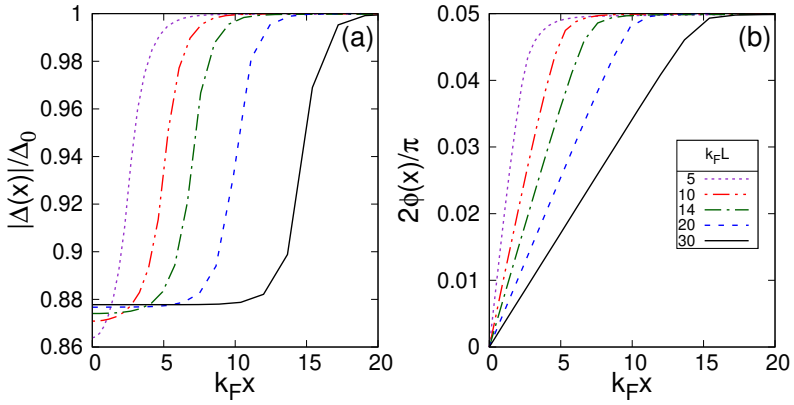

Figure 2.9: Spatial profiles of (a) $|\Delta(x)|$ (in units of Δ_0) and (b) $\phi(x)$, for a barrier of height $V_0/E_F = 0.05$ and several widths $k_F L = (5, 10, 14, 20, 30)$. Here, $(k_F a_F)^{-1} = 0$ and $T/T_c = 0.5$, while the value $\delta\phi/\pi = 0.1$ is kept fixed in all profiles. Symbols are common to both panels. (Reproduced from Ref. [33].)

obtained for two different barriers (whose features are reported in the caption of the figure) at $\delta\phi = 0$. Looking at fig. 2.10, we notice that the values of the healing length $\xi_{\rm out}$ depend only on coupling and temperature, as it is the case for a homogeneous superfluid. In order to confirm this finding, in Fig. 2.10 we have compared the temperature dependence of $\xi_{\rm out}$ with the healing length ξ obtained for a homogeneous system by including pairing fluctuations beyond mean-field [36]. This comparison shows a very good overall agreement.

So far, we have studied the features of the profiles of $|\Delta(x)|$ and $2\phi(x)$ at fixed $\delta\phi$. In fig. 2.11 the profiles of the magnitude and phase of the gap parameter are shown for a given barrier at different $\delta\phi$, in the sense that they correspond to a point on the same current-vs-phase characteristic. In this case, we show also the typical density profiles [see panel (c)]. Looking at panel (a) and panel (c), we notice that the dimensionless ratios $|\Delta(x=0)|/\Delta_0$ and $n(x=0)/n$ are decreasing functions of $\delta\phi$. As a consequence, the profiles show a steeper dependence on the spatial variable (which prevents the LPDA to converge at $\delta\phi_{\rm max}$, as mentioned in section 2.2). These features are common to all the profiles obtained by the LPDA approach.

From the profiles shown in fig. 2.11 we can extract the length $\xi_{\rm out}$ for different $\delta\phi$, and we can do this by considering both profiles $|\Delta(x)|$ and $2\phi(x)$. In the latter case, in order to reduce the numerical uncertainty, it was found it convenient not to use $2\phi(x)$ but rather to consider $2d\phi/dx$ which approaches 0 away from the barrier (as discussed in details in the Appendix A) and to fit it by the expression $C_{\rm out}^{(2\phi)} \exp[-(x - L/2)/\xi_{\rm out}^{(2\phi)}]$. The results of the fitting procedures are shown in fig. 2.12, where $(k_F a_F)^{-1} = 0$ (top panels) and $(k_F a_F)^{-1} = -1$ (bottom panels) for two different barriers. Looking at Fig 2.12, we notice that $\xi_{\rm out}$ at finite $\delta\phi$ depends on the characteristics of the barrier. Upon comparing panel (a) and (b), or (c) and (d), equivalently, we notice that $\xi_{\rm out}$ increases when passing from $V_0/E_F = 0.1$ to $V_0/E_F = 0.05$. Moreover, although the values of $\xi_{\rm out}$ obtained from $|\Delta(x)|$ and $2\phi(x)$ slightly differ from each other, they share the same overall shape, namely, they have a maximum for a certain of $\delta\phi$ which happens to be slightly larger than the abscissa of J_c for the correponding characteristic. These findings are further confirmed in two important limiting situations: On the BCS side of the crossover at $T \lesssim T_c$ and on

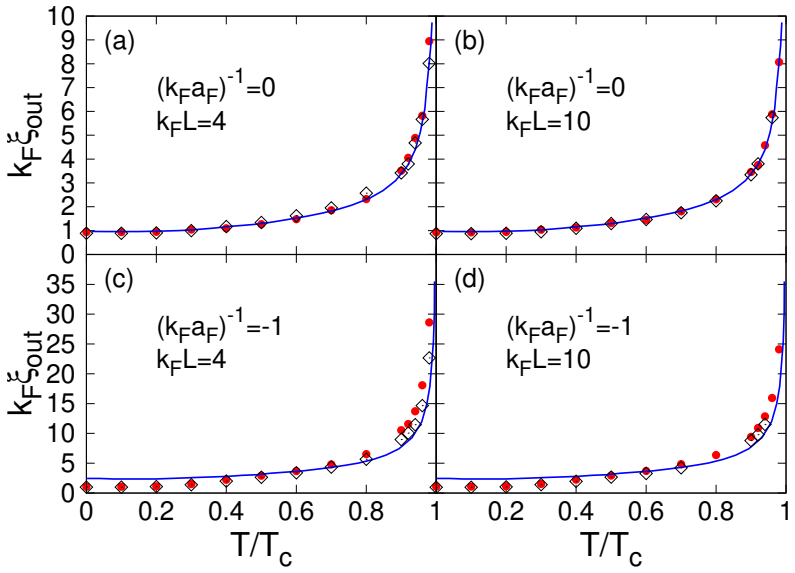

Figure 2.10: Healing length $\xi_{\rm out}$ (in units of k_F^{-1}) vs temperature (in units of T_c),obtained by fitting the numerical LPDA data with the expression (2.6). Here, the barrier has height $V_0/E_F = 0.05$ (dots) and $V_0/E_F = 0.5$ (diamonds), and width $k_FL = 4$ (left panels) and $k_FL = 10$ (right panels), while $\delta\phi = 0$ in all cases. Two coupling values $(k_Fa_F)^{-1} = 0$ (top panels) and $(k_Fa_F)^{-1} = -1$ (bottom panels) are considered. A comparison is also shown with the temperature dependence of the healing length ξ for a homogeneous system (full lines), whereby pairing fluctuations beyond mean field are included for the same couplings (cf. Fig. 10 of Ref. [36]). For this comparison, the results of the present calculation are rescaled by a factor 6/5, which accounts for the different definitions for $\xi_{\rm out}$ and ξ in the two independent calculations. (Reproduced from Ref. [33].)

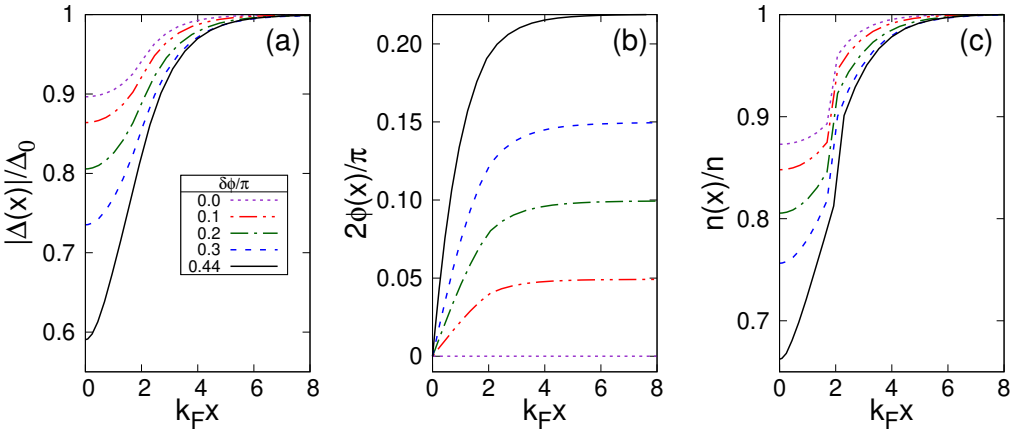

Figure 2.11: Spatial profiles of (a) $|\Delta(x)|$ (in units of Δ_0), (b) $2\phi(x)$, and (c) the density $n(x)$ (in units of the bulk density n), for a barrier of height $V_0/E_F = 0.05$ and width $k_FL = 4$. Here, $(k_Fa_F)^{-1} = 0$ and $T/T_c = 0.5$, while several values of $\delta\phi/\pi = (0.0, 0.1, 0.2, 0.3, 0.44)$ are considered. Symbols are common to all panels. (Reproduced from Ref. [33].)

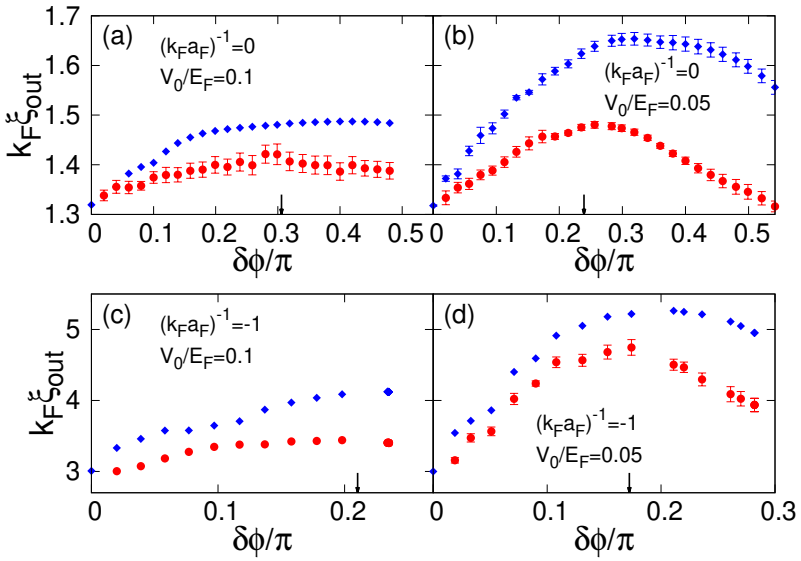

Figure 2.12: Healing length $\xi_{\rm out}$ (in units of k_F^{-1}) vs $\delta\phi$, at temperature $T/T_c = 0.7$ and coupling $(k_F a_F)^{-1} = 0$ (top panels) and $(k_F a_F)^{-1} = -1$ (bottom panels). Here, the barrier has width $Lk_F = 4$ and height $V_0/E_F = 0.1$ (left panels) and $V_0/E_F = 0.05$ (right panels). Both the values of $\xi_{\rm out}$ extracted from the spatial profiles of $|\Delta(x)|$ (diamonds) and of $d\phi(x)/dx$ (dots) are shown, where the error bars arise from the fitting procedure. In each panel, the arrow points at the value of $\delta\phi/\pi$ where the corresponding Josephson characteristic has its maximum. (Reproduced from Ref. [33].)

BEC side at $T = 0$, where the LPDA equation reduces to the Ginzburg-Landau and Gross-Pitaevskii equation respectively (see subsection 1.2.3)[19]. In these cases, we have numerically solved Eq. (1.57) together with the current conservation Eq. (2.2) where $j(\mathbf{r})$ is given by (1.58) as well as Eq. (1.60) together with Eq. (2.2) where $j(\mathbf{r})$ is given by Eq. (1.61), respectively. In fig. 2.13 we report the shape of $\xi_{\rm out}(\delta\phi)$, extracted from the profiles of $|\Delta(x)|$ obtained by solving the GL equation (top panel) and GP equation (bottom panel). As noted before, $\xi_{\rm out}$ reaches its maximum value for a $\delta\phi$ slightly larger than the abscissa of J_c of the corresponding characteristics (shown in the insets for completeness).

2.4 Emergence of the Proximity Effect

In this section, we are interested in the length $\xi_{\rm in}$ complementary to $\xi_{\rm out}$, which describes the spatial range over which the gap reaches the "mini-gap" value[3] (occuring when L is large enough) in the internal region of the barrier.

The world "mini-gap" is usually associated with SN bilayers or SNS trilayers junctions, where the Proximity effect induces superconducting properties in the N layer [38]. Its value identifies the energy range around the Fermi energy in which there are no available states for quasiparticles [39, 40]. In the present context, we used the world "mini-gap" referring to the fact that for wide enough barriers $|\Delta(x)|$

[3]as introduced in Section 2.3 while commenting Fig. 2.9

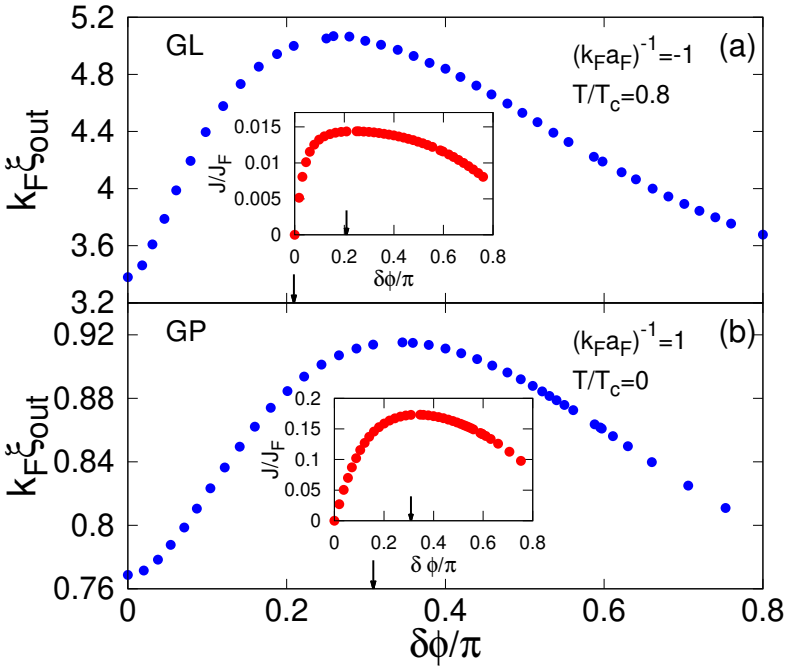

Figure 2.13: Healing length $\xi_{\rm out}$ (in units of k_F^{-1}) vs $\delta\phi$, extracted from the spatial profiles of $|\Delta(x)|$ for a barrier of width $k_FL = 4$ and height $V_0/E_F = 0.05$. Here, $(k_Fa_F)^{-1} = -1$ and $T/T_c = 0.8$ (top panel) and $(k_Fa_F)^{-1} = +1$ and $T = 0$ (bottom panel), which correspond to the conditions when the GL and GP equations can respectively be applied. The arrows point at the values of $\delta\phi/\pi$ where the corresponding Josephson characteristics (shown also for comparison in the insets) have the maximum. (Reproduced from Ref. [33].)

becomes flat in the interior region of the barrier (cf. Fig. 2.9) and its value is not affected by further increasing the barrier width. This aspect allows us to regard the present SS'S system as an effective SNS junction, where the N layer is a superfluid with a lower critical temperature than T_c. Further details on this parallelism can also be found in Section 2.9.

The length $\xi_{\rm in}$ can be interpreted as the equivalent in a SS'S junction of the coherence length ξ_N in a SNS junction [2]. In order to extract $\xi_{\rm in}$ in a meaningful way, in the following the barrier width will be significantly increased with respect to the values mostly considered so far.

Following the procedure of Ref. [2], we show in Fig. 2.14 the temperature dependence of the critical current J_c for two barrier heights (left and right top panels) using different barrier widths, as well as the depence of J_c on the barrier width at different temperatures for two barrier heights (left and right bottom panels). The top and bottom panels of Fig. 2.14 correspond to Fig. 2 and Fig. 3 of Ref. [2], respectively. Looking at the top panels, we see that the critical current is a decreasing function of temperature and approaches 0 as $T \to T_c^-$. We notice also that the drop of the ratio J_c/J_F gets more abrupt for increasing L and spans three orders of magnitude for $0 \leq T \leq T_c$, similarly to what was reported in Fig. 2 of Ref. [2]. Looking at the bottom panels of Fig. 2.14, we see instead that increasing the barrier width may result, depending on temperature, in a continuous drop of

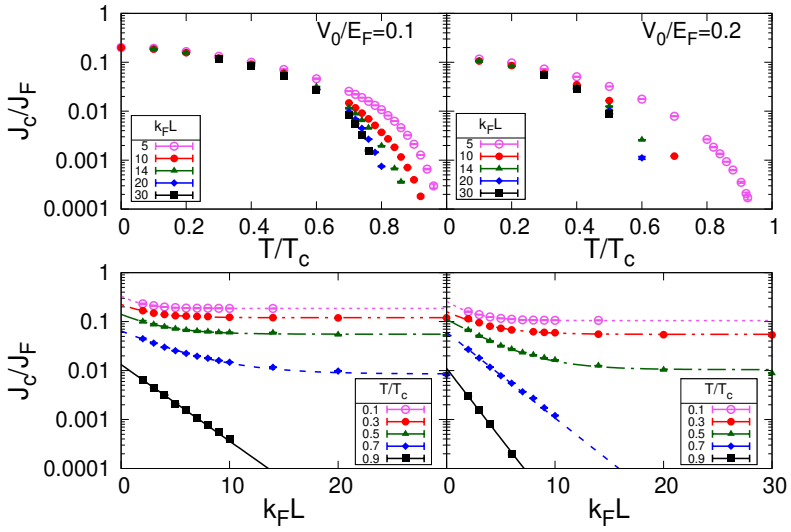

Figure 2.14: Upper panels: Temperature dependence of the critical current J_c (in units of J_F) at unitarity for two barrier heights and several barrier widths. Lower panels: Width dependence of J_c for several temperatures. The curves through the numerical data (symbols) correspond to fits obtained by the expression (2.7). (Reproduced from Ref. [33].)

the critical current or in reaching an asymptotic value. For this reason, we have identified the dependence of J_c on the barrier width by a fit of the type

$$J_c(L) = J_c^0 e^{-L/\xi_{\rm in}^{J_c}} + J_c^{\rm mini}, \tag{2.7}$$

performed in terms of the parameters J_c^0, $\xi_{\rm in}^{J_c}$ and $J_c^{\rm mini}$. Looking at the curves in the bottom panels of Fig. 2.14, we notice that, as anticipated, $J_c^{\rm mini}$ remains finite only up to a certain temperature, above which J_c appears to have an exponential dependence on the barrier width L (as reported in Fig. 3 of Ref. [2] for $T > T_c^N$).

The temperature dependence of the fitting parameters $\xi_{\rm in}^{J_c}$ and $J_c^{\rm mini}$ is shown in the top and bottom panels of Fig. 2.15, respectively, for the same barrier heights considered in Fig. 2.14. For completeness, in the insets of the bottom panels we show the characteristics in correspondence to the largest barrier widths here considered. It should be remarked, that in these cases, it is not possible to use eq. (2.3) to fit $J_c(\delta\phi)$, because for the widths here considered the Josephson characteristics become "re-entrant" (sometimes called "multivalued" [15]) and extend beyond $\delta\phi > \pi$. Nevertheless, we are still able to distinguish the value of J_c (black dots) which is shared by all characteristics here considered. This aspect, by our interpretation, signals the presence of a minigap.

Looking at the top panels of Fig. 2.15, we see that $\xi_{\rm in}^{J_c}$ has a substantial enhancement in correspondence to a temperature $T_c' < T_c$. At the same temperature, $J_c^{\rm mini}$ drops to zero. These two combined effects are reminiscent of the proximity effect [41] in a SNS junction[2], where the normal metal acquires superconducting properties due to the "proximity" to the superconducting material and allows for a supercurrent flow. This effect, known as "proximity-induced Josephon effect" [42, 43], is in a sense complementary to what we have reported in Fig. 2.15, which could be thus referred to as "*Josephson-induced proximity effect*".

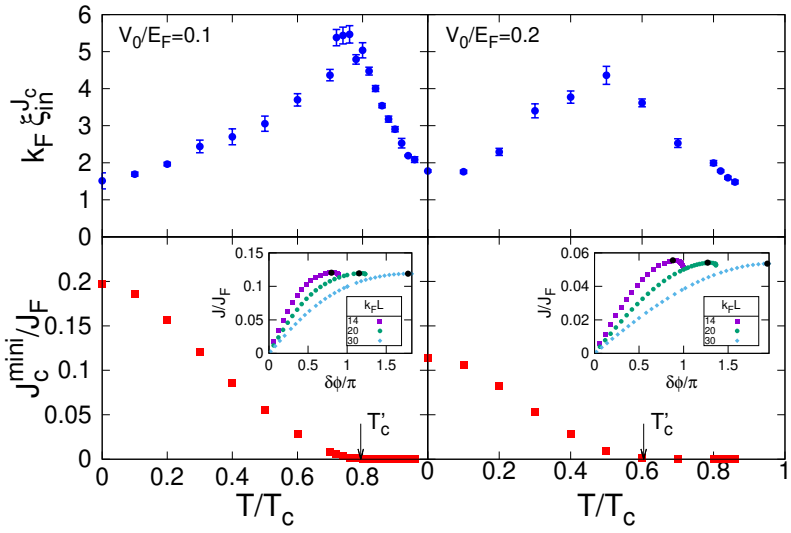

Figure 2.15: Upper panels: Temperature dependence of the healing length $\xi_{\rm in}^{J_c}$ (in units of k_F^{-1}) obtained at unitarity from the fit (2.7) for two barrier heights. Lower panels: Corresponding temperature dependence of the parameter $J_c^{\rm mini}$ of the fit 2.7. The vertical arrows mark the temperature $T_c^{'}$ where $J_c^{\rm mini}$ vanishes. The insets show the Josephson characteristics for $T/T_c = 0.3$ and three values of $k_F L$. (Reproduced from Ref. [33].)

In order to confirm our findings, we can study in detail the profile $|\Delta(x)|$ in the region where the potential barrier occurs. In Section 2.3 (cf. Fig. 2.9), we noticed that increasing the barrier width L of the barrier may result in a profile of $|\Delta(x)|$ which is essentially flat in the internal region of the barrier. As already mentioned, this could be interpreted as the emergence of a minigap $\Delta_{\rm mini}$. Accordingly, provided the barrier width is large enough, we identify the behaviour of $|\Delta(x)|$ with a fit of the type:

$$|\Delta(x)| = \Delta_{\rm in} e^{-|x+L/2|/\xi_{\rm in}^{\Delta}} + \Delta_{\rm mini} \qquad \text{for} \quad -L/2 \lesssim x \lesssim 0, \tag{2.8}$$

in terms of the two parameters $\Delta_{\rm in}$ and $\xi_{\rm in}^{\Delta}$. The fitting function (2.8) was already used in [44], where we studied the gap profiles of an SN interface obtained by the non-local (integral) version of the LPDA equation [30] with no current flow.

In Fig. 2.16 we show the temperature dependence of $\xi_{\rm in}$ (top panels) and $\Delta_{\rm mini}$ (bottom panels) for the same barrier heights considered in Fig. 2.15 (left and right panels). The fitting procedure has been applied both for $J = 0$ ($\delta\phi = 0$) and for a finite current flow ($\delta\phi/\pi = 0.2$). The insets of the top panels show an example of the fitting procedure performed on the magnitude of the gap profiles. Looking at the top panels of Fig. 2.16, we see that $\xi_{\rm in}^{\Delta}$ has an enhancement in correspondence to a temperature $T_c^{'}$ below T_c. At the same temperature, $\Delta_{\rm mini}$ vanishes and remains zero up to T_c.

Looking at the top panels of Fig. 2.16, we notice that $\xi_{\rm in}^{J_c}$ and $\xi_{\rm in}^{\Delta}$ share the same behaviour and assume similar values at each temperature. The agreement between the data sets is better in the region $T > T_c^{'}$ where the fitting procedure Eq. (2.7) becomes more reliable.

The values obtained in Fig. 2.16 for $\xi_{\rm in}^{\Delta}$ and $\Delta_{\rm mini}$ at $\delta\phi = 0$ and $\delta\phi/\pi = 0.2$ are practically indistinguishable from each other. Notice that for $T > T_c^{'}$ the values of

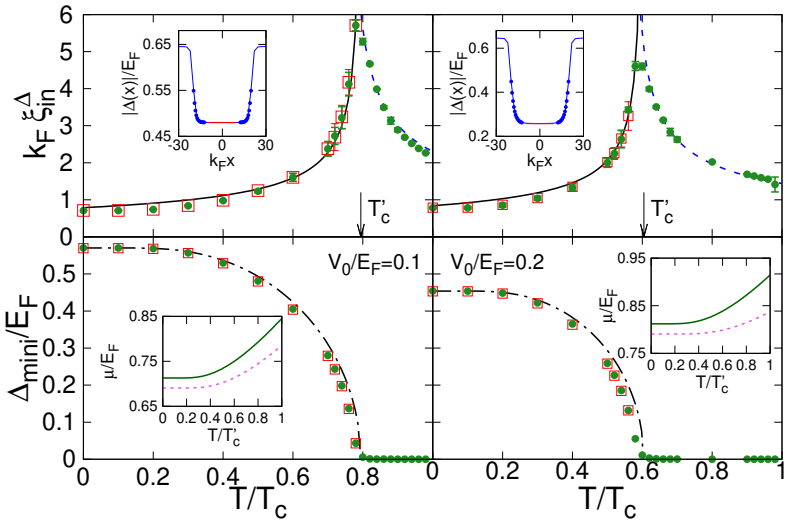

Figure 2.16: Temperature dependence of the healing length $\xi_{\rm in}^{\Delta}$ (in units of k_F^{-1}) obtained at unitarity from the fit (2.8) for two barrier heights. The vertical arrows mark the temperature $T_c^{'}$ at which $\Delta_{\rm mini}$ vanishes. The insets show the spatial profiles of $|\Delta(x)|$ in the presence of a current (lines) with the associated fits (dots) for $T/T_c = 0.5$ and $k_F L = 40$, from which the plateau corresponding to $\Delta_{\rm mini}$ can be identified. Lower panels: Temperature dependence of the minigap $\Delta_{\rm mini}$ (with the same symbols of the upper panels). The insets show the temperature dependence of the chemical potential at unitarity shifted upward by V_0/E_F (broken lines) and of the chemical potential for the effective couplings listed in Table 2.1 (full lines). In all panels, the numerical data (symbols) are obtained for a given value of $\delta\phi$ in the Josephson characteristics, corresponding to zero current ($\delta\phi = 0$ - filled dots) and a finite current ($\delta\phi/\pi = 0.2$ - empty squares). The meaning of the broken lines passing through these symbols is explained in the text. (Reproduced from Ref. [33].)

$\xi_{\rm in}^{\Delta}$ and $\Delta_{\rm mini}$ for $\delta\phi/\pi = 0.2$ are missing because within LPDA approach it is not possible to sustain a finite current flow when $|\Delta| = 0$.

The continuous lines in the top panels of Fig. 2.16 represent the same fitting procedures performed in [44] for the length ξ_R (equivalent to ξ_N in [2]) near T_c^R, which in our case corresponds to identify $\xi_{\rm in}$ through the relations

$$k_F\xi_{\rm in}^{\Delta} = C_{\rm in}\sqrt{1 - T/T_c'} \qquad \text{for} \quad T < T_c', \tag{2.9a}$$

$$k_F\xi_{\rm in}^{\Delta} = C_{\rm in}\sqrt{T/T_c' - 1} \qquad \text{for} \quad T > T_c', \tag{2.9b}$$

where $C_{\rm in}$ is a dimensionless parameter and $T_c^{'}$ is identified as the temperature at which $\Delta_{\rm mini}$ vanishes.

To the temperature $T_c^{'}$ we can associate an effective coupling $(k_F a_F)_{\rm eff}^{-1}$ in the internal region of the barrier. The values of $(k_F a_F)_{\rm eff}^{-1}$ for the physical systems considered in Fig. 2.16 are reported in Tab. 2.1. Using these values, in the lower panels of Fig. 2.16 we have compared the temperature dependence of $\Delta_{\rm mini}$ (symbols) with that of the bulk gap $\Delta_{\rm homo}$ (broken lines) obtained for $(k_F a_F)_{\rm eff}^{-1}$. The good agreement between the two data sets encourages our interpretation of Figs. 2.15 and 2.16 in terms of a "Josephson-induced proximity effect", which acts to convert the

V_0/E_F	$T_c^{'}/T_c$	$(k_F a_F)^{-1}_{\rm eff}$
0.1	0.794	-0.189
0.2	0.604	-0.397

Table 2.1: Values of the temperature $T_c^{'}$ (in units of the bulk critical temperature T_c) at which $\Delta_{\rm mini}$ vanishes and of the related effective coupling $(k_F a_F)^{-1}_{\rm eff}$, for the two barrier heights considered in Fig. 2.16.

internal (s) region of the SS'S junction into the N region of an SNS junction with an appropriate effective coupling smaller than the coupling in the S region. This result is remarkable from a physical point of view, since it implies that a local one-body potential (the barrier) can locally induce a change in the two-body interaction. The novelty of this finding relies on the fact that the external potential induces a local change in the inter-particle interaction while not affecting the dimensionality of the system.

Nevertheless, we cannot fully identify the internal (S') region of the SS'S junction with an indipendent piece of material, as it is for a SNS junction, with its own bulk thermodynamic properties. This is because at thermodynamic equilibrium the chemical potential $\mu_{\rm eff}$ associated with $(k_F a_F)^{-1}_{\rm eff}$, should satisfy the identity $\mu_{\rm eff} - V_0 = \mu$. However, as it can be seen from the insets of the bottom panel of Fig. 2.16, this identity is only approximately satisfied by our numerical calculations.

2.5 Identification of an extended BCS regime

In principle, the GL equation could be applied when $(k_F a_F)^{-1} \to -\infty$ and at $T \simeq T_c^-$, which is a very limited portion of the coupling-temperature phase diagram. Nevertheless, GL equation is commonly applied even outside this limited portion of the coupling-temperature phase diagram. For this reason, we would like to identify an extended BCS regime where the GL equation can be approximately applied. In order to do that, we have preliminarly checked that the numerical values of the coefficients $\mathcal{I}_0(\mathbf{r})$ and $\mathcal{I}_1(\mathbf{r})$ whithin the LPDA approach (see Eqs. (1.50)) recover their GL limiting expressions (see Eqs. (1.56)) in the appropriate coupling and temperature regimes. Moreover, in the same portion of coupling-temperature phase diagram, we have compared the $|\Delta(\mathbf{r})|$ profiles which are solution to the LPDA and GL equations for given barrier height and width. In the top panels of Fig. 2.17, we show the color map of the difference $|\Delta^{\rm GL}(x=0)| - |\Delta^{\rm LPDA}(x=0)|$ at fixed $\delta\phi/\pi = 0.2$, while in the bottom panels we show the color map of the difference $(J_c^{\rm GL} - J_c^{\rm LPDA})$. Both quantities are essentially the same when $(k_F a_F)^{-1} \leq -0.7$ and $T/T_c \geq 0.85$, which identify the ranges of the extended BCS regime we were after.

2.6 Critical Current

In section 2.4, we have shown how the critical current J_c is affected by the barrier width keeping all the other relevant physical parameters fixed, namely, the barrier height, coupling, and temperature. In this section we aim at performing a systematic analysis of these dependences.

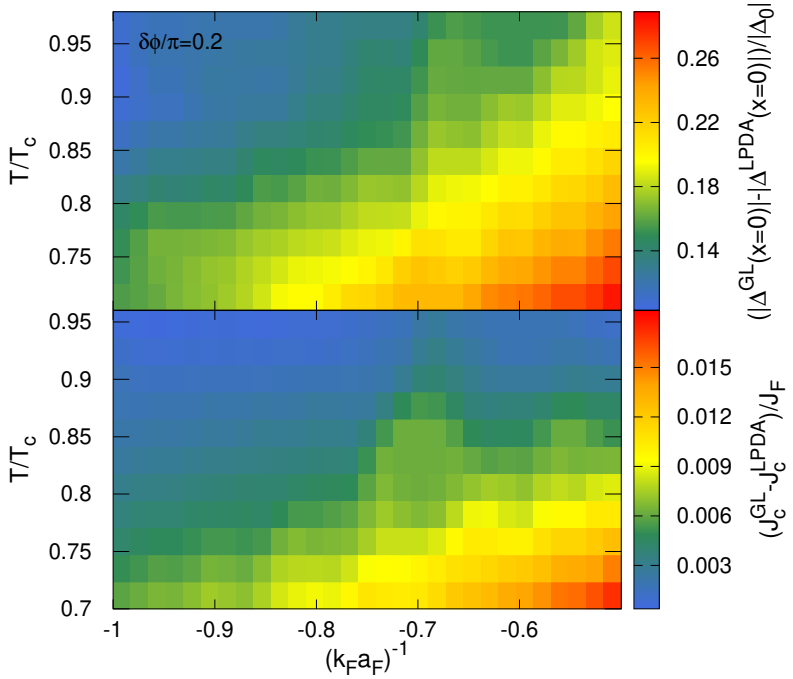

Figure 2.17: Color maps in the temperature-coupling phase diagram, showing the difference of the magnitude of the gap parameter $|\Delta(x=0)|$ at the barrier center in units of the bulk value Δ_0 (upper panel) and of the critical current J_c in units of J_F (lower panel) which are obtained by solving alternatively the GL equation (1.57) and the LPDA equation (1.49). All numerical values are obtained with a barrier of height $V_0/E_F = 0.1$ and width $k_F L = 4$. In addition, in the upper panel a fixed value $\delta\phi/\pi = 0.2$ is used. (Reproduced from Ref. [33].)

In Fig. 2.18 we show color maps of J_c (left panels) for decreasing barrier heights (from top to bottom) in the temperature-coupling phase diagram, as well as the coupling dependence of J_c (right panels) for the same barrier heigths at various temperatures. Looking at the color maps, we notice that at $T = 0$ increasing the barrier height shifts the maximum value of J_c to the BCS side of the crossover (as observed in [9]), while, looking at the panels on the right, we see that increasing the temperature results in a shift to the BEC side of the crossover.

In Fig. 2.19 we show the temperature dependence of J_c at fixed barrier width for various barrier heights (left panels), and at fixed barrier height for various barrier widths (right panels) using two values of the coupling: $(k_F a_F)^{-1} = 0$ (top panels) and $(k_F a_F)^{-1} = -1$ (right panels). Comparing the plots on the left and on the right, we conclude that the barrier height affects the critical current more significantly than the barrier width. We point out here that the data for $(k_F a_F)^{-1}$ in the region $T \lesssim 0.3T_c$ are missing due to the limitations of LPDA (mean-field) approach mentioned in Section 2.3. Moreover, we have verified that the values obtained for J_c at $T = 0$ and unitarity compare favourably with those shown in [9] using the same barrier heigths and widths.

Once we have established that $J_c \to 0$ for $T \to T_c^-$, it is of interest to verify how this limit is achieved. We identify the temperature dependence of J_c near T_c

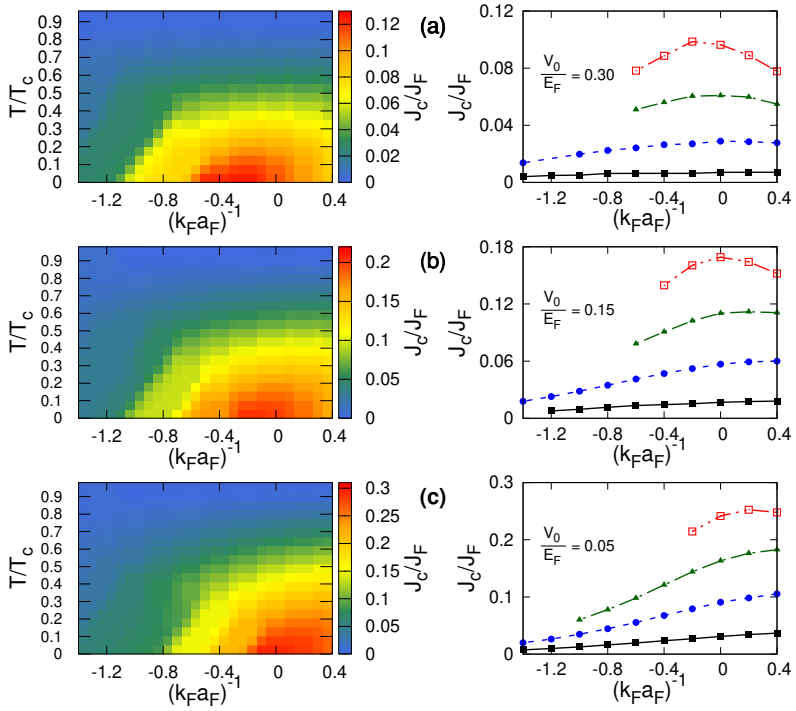

Figure 2.18: Critical current J_c (in units of J_F) for a barrier of width $k_F L = 2$ and various heights: (a) $V_0/E_F = 0.30$, (b) $V_0/E_F = 0.15$, and (c) $V_0/E_F = 0.05$. For each barrier, the left panels show the colour maps of J_c/J_F in the temperature-coupling phase diagram, while the right panels show the curves J_c/J_F vs $(k_F a_F)^{-1}$ for various temperatures: $T/T_c = 0.2$ (empty squares), $T/T_c = 0.4$ (filled triangles), $T/T_c = 0.6$ (filled circles), and $T/T_c = 0.8$ (filled squares). Note the different vertical scale in each panel. (Reproduced from Ref. [33].)

through a fit of the type

$$\frac{J_c(T)}{J_F} = Dt^{\eta}, \qquad \text{where} \quad t = 1 - \frac{T}{T_c}, \tag{2.10}$$

performed in terms of the dimensionless parameter D and the exponent η. In [15] it was found that η dependends on the barrier type. Accordingly, in the present context of an SS'S junction, we expect η to depend on both barrier height and width.

In order to perform a systematic study, we choose to evaluate η for different barriers with two couplings: $(k_F a_F)^{-1} = -1$, representative of the BCS side of the crossover, and $(k_F a_F)^{-1} = 0$. For $(k_F a_F)^{-1} = -1$, we found it convenient to use the results obtained by solving the GL equation (1.57), which was proven to reproduce the LPDA results over an extended BCS region (see section 2.5). The fit (2.10) is performed over $M = 10$ points and on a restricted temperature range, that is, $0.93T_c \leq T \leq 0.98T_c$. At unitarity, on the other hand, we have used the LPDA results and applied the fitting procedure (2.10) over $M = 15$ points and the temperature range $0.9T_c \leq T \leq 0.98T_c$. In this case, the lower limit of the temperature range could have been further reduced to $0.85T_c$ with no particular change on the fitting function.

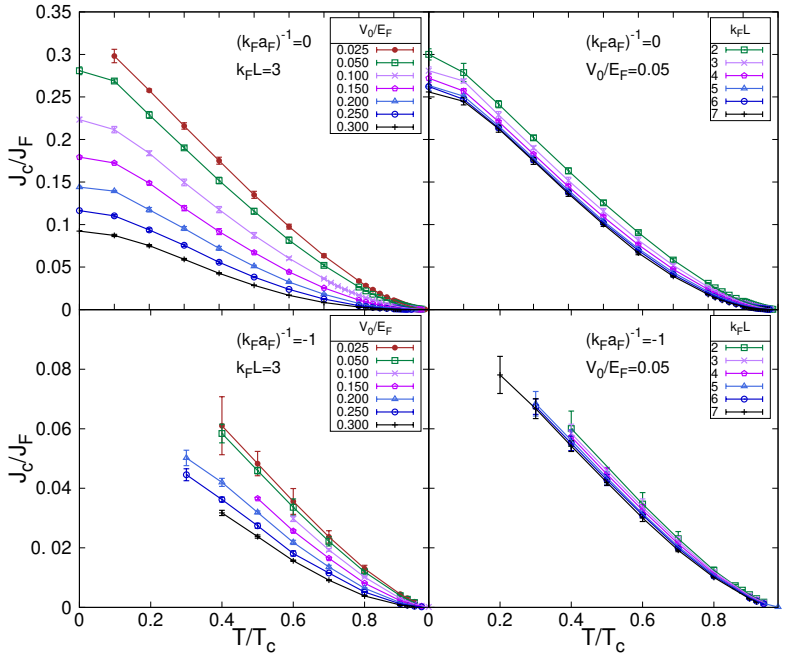

Figure 2.19: Temperature dependence of the critical current J_c (in units of J_F), for a barrier of width $k_F L = 3$ and various heights (left panels), and a barrier of height $V_0/E_F = 0.05$ and various widths (right panels). In each case, the upper and lower panels refer to couplings $(k_F a_F)^{-1} = 0$ and $(k_F a_F)^{-1} = -1$, respectively. (Reproduced from Ref. [33].)

The upper limit of $0.98T_c$ is due to the numerical inability for obtaining a realiable characteristic with a critical current smaller than $10^{-4}J_F$, while the lower limits were chosen by looking at the temperature dependence of J_c at $(k_F a_F)^{-1} = -1$ and $(k_F a_F)^{-1} = 0$. They reflect our expectation that the width of the critical region near T_c is larger at unitarity than in the BCS regime [45].

In Fig. 2.20 we show the results of the fitting procedure (see eq. (2.10)) of the critical current, both for $(k_F a_F)^{-1} = -1$ (left panel) and $(k_F a_F)^{-1} = 0$ (right panel). In the first case, the fit is done using M points (the green ones in the plot) with M ranging from 5 to 10, while at unitarity M ranges from 5 to 15. The values obtained for η in each case, namely, for each set of the M points used in the fitting procedure, are shown in the insets of each panel. These values show little variation, and for this reason the critical exponent η, reported in each panel, has been identified with its average. In principle, the upper limit of the temperature range $0.98T_c$ we are considering in the numerical calculations, may affect the numerical value of η. However, we are confident that the M points considered are distributed in a sufficiently smooth way, that the error on the exponent η in the restricted interval of T/T_c we are considering does not exceed a few percent.

We have performed the analysis shown in Fig.2.20 for a wide set of barrier heights and widths, for both $(k_F a_F)^{-1} = -1$ and $(k_F a_F)^{-1} = 0$, in order to verify how η is affected by the barrier characteristics. The results of this analysis are shown in the colormaps of Fig. 2.21. Looking at the left panel for $(k_F a_F)^{-1} = -1$ we see that η takes the value 1.5 in the bottom-left corner (high-transparency barriers), and evolves smoothly towards the value 2 in the top-right corner (low-transparency

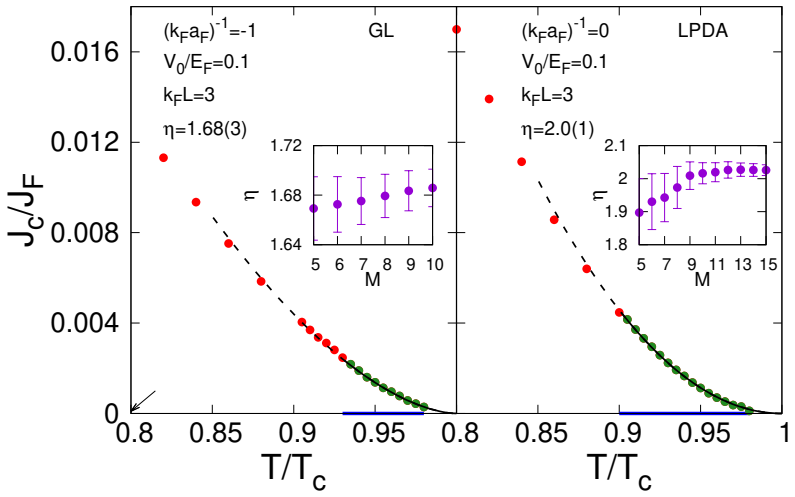

Figure 2.20: Numerical procedure to obtain the exponent η for the vanishing of J_c upon approaching T_c. The same barrier is considered for two different couplings. In both panels, the temperature interval of the fit (2.10) corresponds to blue thick segment, and the M values of $J_c(T)/J_F$ over which the fit is applied correspond to the green dots (additional values of $J_c(T)/J_F$ are given by the red dots). The black thick curve through the green dots gives the result of the fit, which is extrapolated outside its range by the dashed curve.The oblique arrow in the left panel points to the minimum value of J_c that can be handled numerically with confidence.The insets reports the values of η with the associated error bars, obtained by restricting the fit (2.10) to the first M numerical values closer to the upper limit $T/T_c = 0.98$ used in the fit. (Reproduced from Ref. [33].)

barriers), in accordance with what predicted in [15]. By making a comparison between the left and right panels, we notice that at unitarity the exponent η takes systematically larger values with respect to those at the same barrier height and width for $(k_F a_F)^{-1} = -1$. None of the combinations of V_0 and L here considered seems to model a tunnel junction with small transmission probability [11], for which $\eta = 1$.

2.7 The Landau Criterion

In this section, we aim at developping a procedure to determine the critical current J_c, above which superfluidity is destroyed, at any temperature in the BCS-BEC crossover. Following the Landau criterion [46], we expect the LPDA equation not to have solutions for $J > J_c$, whereby the superfluid flow is expected to be dissipative and unstable, thus preventing the convergence of the LPDA equation.

There are two different mechanisms by which superfluidity is destroyed: The pair-breaking excitations on the BCS side of the crossover and the sound mode quanta on the BEC side of the crossover. These two limiting situations have already been taken into consideration in the context of Josephson effect at zero temperature [9] and we expect the LPDA results to be consistent with them.

To extend the Landau criterion at finite temperature, we will exploit the Josephson characteristics for decreasing barrier heights and widths down to vanishingly

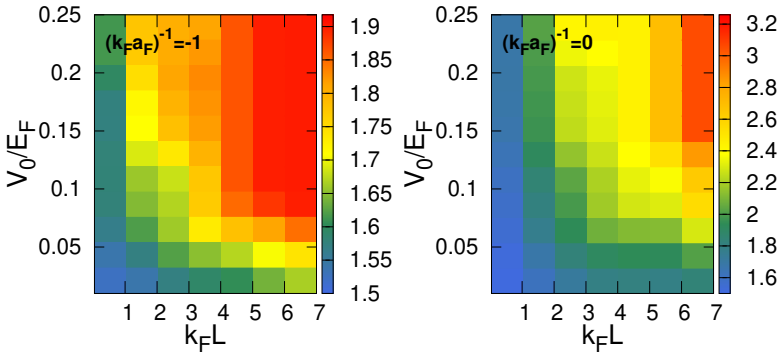

Figure 2.21: Colour maps of the exponent η for the critical current J_c in the critical region. Results are shown for two coupling values over extended ranges of the barrier height and width. (Reproduced from Ref. [33].)

small barriers, in order to identify the critical value J_c we are looking for when $V_0 \to 0^+$ and $L \to 0^+$. This procedure has already been used in Ref. [9] where the BdG equations applied to the Josephson effect were proven to include both the dissipative mechanisms mentioned above. We expect the critical current to be a decreasing function of the temperature for any coupling since the superfluid density decreases for increasing temperature, as shown in the insets of Fig. 2.3.

In order to obtain J_c for a vanishingly small barrier, we have at first studied the dependence of J_c on the barrier height V_0 for fixed barrier width L. The results of this study are shown in Fig. 2.22 at unitarity for $k_F L = 2$. Looking at the main plot of Fig. 2.22, we have identified the dependence of J_c on V_0 via the relation

$$\frac{J_c(V_0)}{J_F} = E e^{-V_0/F} \tag{2.11}$$

in terms of the parameters E and F. The occurence of an exponential dependence on V_0 for fixed L could be inferred also from Fig. 13 of Ref. [37], although there only at unitarity and for $T = 0$.

The quite large sets of barrier heights here considered and the fitting procedure Eq. (2.11) allows us to extrapolate $J_c(0) = J_c(V_0 \to 0^+)$. This quantity has been evalued for different barrier widths and its depence on L is reported in the inset of Fig. 2.22. The quantity $J_c(0)$ appears to have no dependece on L, in such a way that $J_c(0)$ can be identified as the critical current.

The procedure explained above has been applied to obtain $J_c(0)$ in the ranges $-1.4 < (k_F a_F)^{-1} < 1.4$ and $0 \leq T < T_c$, and has involved the analysis of about 30000 Josephson characteristics. The main results of this systematic study are shown in Fig. 2.23, where the values of $J_c(0)$ implement the Landau criterion for superfluidity at finite temperature along the BCS-BEC crossover. The values of $J_c(0)$ in Fig.2.23 are consistent with the critical exponent $\eta = 1.5$ as $T \to T_c^-$ irrespective of coupling (see Fig. 2.21).

From Fig. 2.23 we notice that the LPDA results all lie (within the numerical error) in the shaded region delimited by the broken lines, that correspond to pair-breaking excitations on the BCS side of unitarity (left branch) and sound-mode excitations on the BEC side of the crossover (right branch) [9]. This fact, which wad already observed in [9] at $T = 0$, is rather remarkable: The LPDA results for

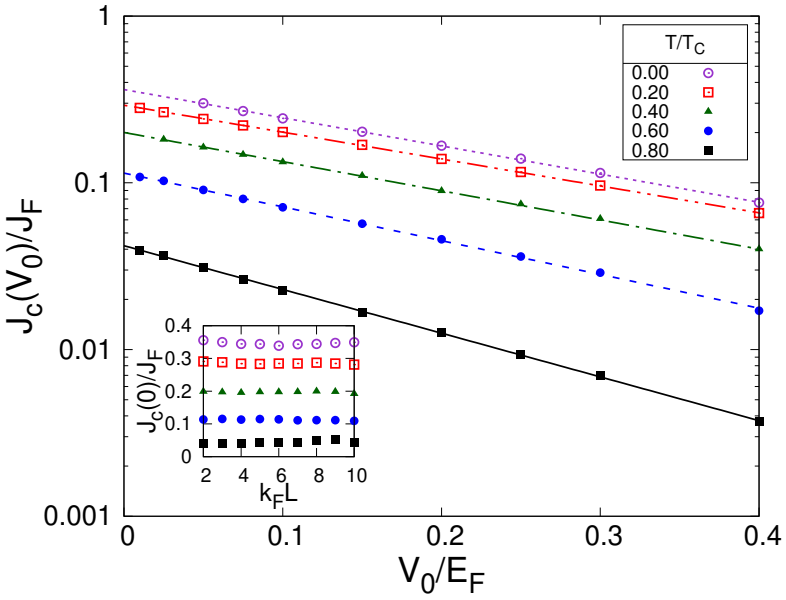

Figure 2.22: Semi-log plot of the critical current $J_c(V_0)$ (in units of J_F) vs V_0/E_F with a barrier of width $k_F L = 2$, for $(k_F a_F)^{-1} = 0$ and various temperatures. The inset shows the behaviour of the limiting value of $J_c(0) = J_c(V_0 \to 0^+)$ when the width L is varied, for the same coupling and temperatures of the main panel. (Reproduced from Ref. [33].)

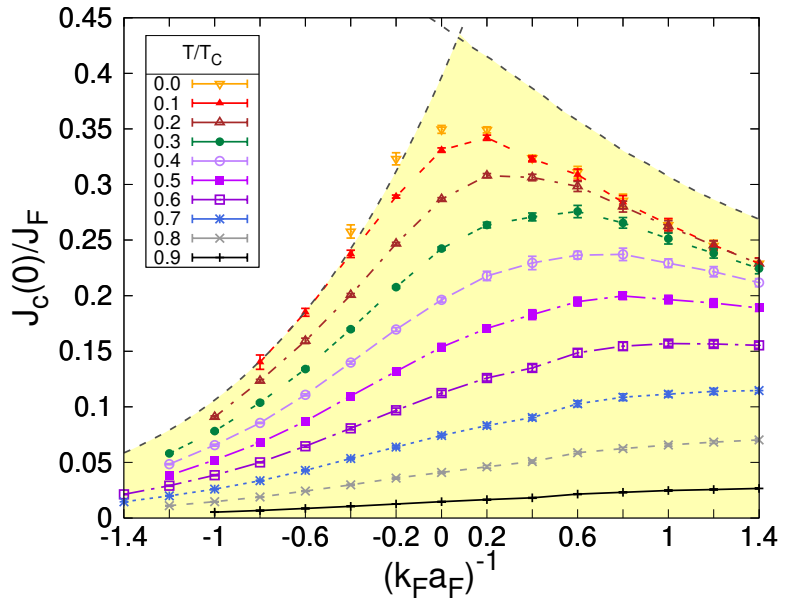

Figure 2.23: The critical current $J_c(0)$ (in units of J_F), for which the superfluid flow becomes unstable in the limit of a barrier with vanishing height and width, is shown as a function of $(k_F a_F)^{-1}$ for several temperatures. The left and right dashed lines (which cross each other near unitarity) correspond to the appearance at $T = 0$ of pair-breaking and sound-mode excitations, respectively [9]. The shaded area highlights the region of allowed superfluid flow, where the superfluid critical current lies below both dashed lines. (Reproduced from Ref. [33].)

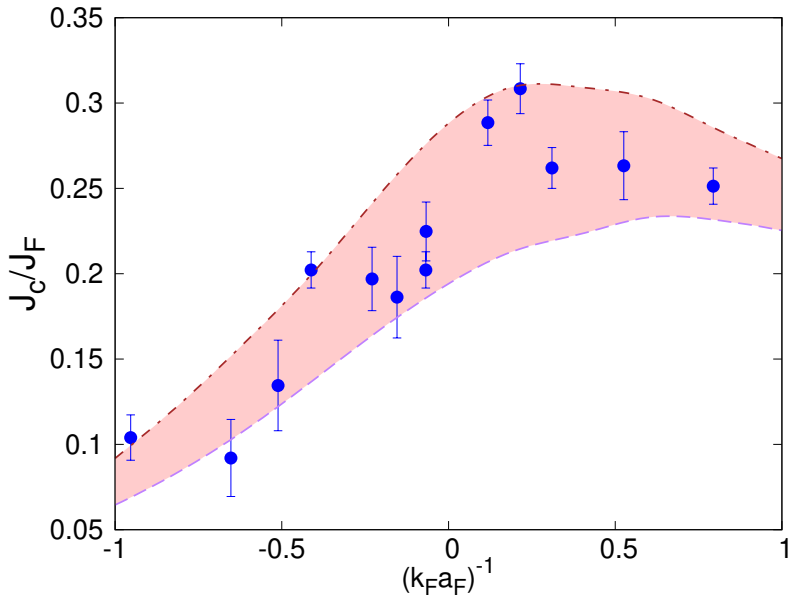

Figure 2.24: Comparison of the values of J_c/J_F over an extended coupling range, obtained experimentally in Ref. [5] for a weak barrier (dots with error bars) and calculated theoretically for a vanishingly small barrier in the temperature interval $0.2 \leq T/T_c \leq 0.4$ (shaded area). The upper and lower curves delimiting the shaded area correspond, respectively, to the values $T/T_c = 0.2$ and $T/T_c = 0.4$ in Fig. 2.23. (Reproduced from Ref. [33].)

the inhomogeneous problem at hands, namely, an homogeneous superfluid with a vanishingly small barrier, appear to include not only pair-braking excitations on the BCS side of the crossover (which are explicitly included in the mean-field treatment of a homogeneous system), but also sound-mode excitations on the BEC side of the crossover (which for a homogeneous system would require the inclusion of pairing fluctuations beyond mean-field). Despite this positive feature, we believe that the inclusion of pairing-fluctuations beyond the present mean-field treatment is still required, since it should change quantitatively the results of Fig. 2.23 especially at finite temperature on the BEC side of the crossover [47].

We have further compared the data of Fig. 2.23 with the experimental results of Ref. [5]. In this experiment particular effort was made to produce a small perturbation to a superfluid system of ^{6}Li atoms. A red detuned laser was moved in the atomic cloud with constant velocity and the column integrated density at the cloud center was measured. Variation of this quantity with respect to the unperturbed value signaled the reaching of the critical velocity. The experiment was carried out at low enough temperature. For this reason, in fig. 2.24 we have compared the experimental results with our results comprised in the area between the curve for $T = 0.2T_c$ and $T = 0.4T_c$ of Fig. 2.23. The shaded area obtained theoretically shows a good agreement with the experimental data.

Recently, a relation between the critical current J_c and the condensate density n_c for low transparency barriers, based on theoretical arguments valid on the BEC side of the crossover but extended also to the BCS side of the crossover [48], was used to determine the condensed density from the experimental measurements of J_c [3]. Here, we look for a relation between the same quantities in the complementary

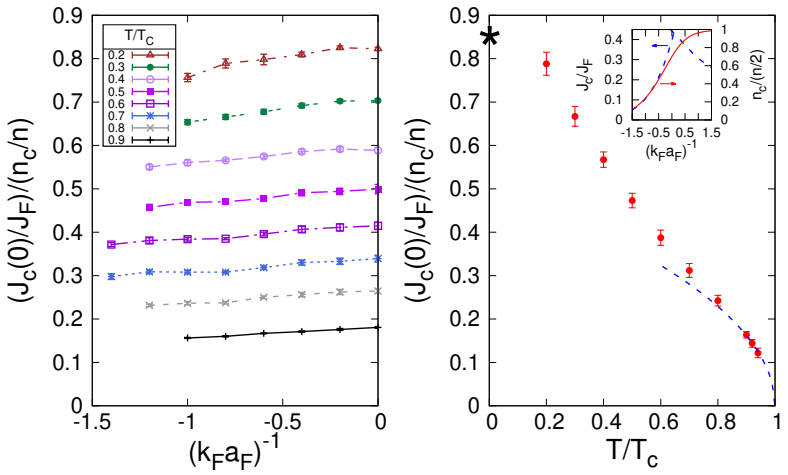

Figure 2.25: Left panel: Coupling dependence of the ratio between $J_c(0)/J_F$ taken from Fig. 2.23 and the condensate density n_c (in units of the bulk density n) obtained at the mean-field level [49] for various temperatures. Right panel: Temperature dependence of the "universal" function extracted from this ratio in the interval $0.2 \leq T/T_c \leq 0.9$. Here, the broken line corresponds to a square-root behaviour close to T_c and the star for the value $8/(3\pi)$ obtained analytically at $T = 0$. The inset shows the coupling dependences of $J_c(0)/J_F$ (dashed line - left scale) and of $n_c/(n/2)$ (full line - right scale) at $T = 0$, covering the whole BCS-BEC crossover. (Reproduced from Ref. [33].)

regime, namely, for a vanishingly small barrier and on the BCS side of the crossover. We have taken into consideration the values $J_c(0)/J_F$, shown in Fig. 2.23, for $-1.4 \leq (k_F a_F)^{-1} \leq 0$ and $0.2T_c \leq T \leq 0.9T_c$, and divided them by the ratio n_c/n, where n_c is the condensed density evaluated at the mean-field level [49] and n the bulk density. The results of this calculation, shown in the right panel Fig. 2.25, appear to be independent of coupling. In the left panel of Fiq. 2.25 we have plotted the "universal function" of $J_c n_c/J_F n$ vs temperature, by taking the average value of $J_c n_c/J_F n$ from the right panel at fixed temperature and associating with it an error equal to the difference between its maximum and minimum values. The ratio is a decreasing function of the temperature and vanishes as $T \to T_c^-$ with a square-root behaviour, as expected. Moreover, the relation found and numerically proven at finite temperature, holds true also at $T = 0$, as shown in the inset of Fig. 2.25, for which analytical expressions are available for both the critical current [9] and the condensed density [49].

2.8 Comparison with Experimental Data

In this section, we will compare the LPDA results for specific barrier heights and widths with experimental data obtained by shining a laser and moving it at constant speed through a ^{6}Li atomic gas in a harmonic trap [3]. Particular care will be taken in this case to translate the experimental parameters into the ones used in the LPDA approach.

In the harmonic trap the Fermi energy is identified by $E_F^t = \omega_0(3N)^{1/3}$, where

ω_0 is the geometric average of the trapping frequencies and N the total number of atoms. In terms of E_F^t and the associated Fermi wavevector k_F^t, it is possible to infer the dimensionless values V_0/E_F^t and $k_F^t L$ used in the experiment. The moving laser, which plays the role of a potential barrier, spans only the central region of the atomic gas. Therefore, it seems reasonable to identify the Fermi wavevector k_F used in the theoretical calculations with the experimental value k_F^0 at the trap center. As a consequence, knowing the ratio $\kappa = E_F^t/E_F^0$, where $E_F^0 = (k_F^0)^2/(2m)$, allows us to determine both the barrier height and width in terms of E_F and k_F, respectively, values to be used in the LPDA approach to simulate the experimental barrier. We point out that in this calculation the external potential used has the shape

$$V_{ext}(x) = V_0 \exp\left(-2\frac{x^2}{2w^2}\right), \tag{2.12}$$

where w is the Gaussian width of the potential. We further notice that the values J_c/J_F obtained by the numerical calculations have to be multplied by κ^2 in order to be comparable with the experimental data for J_c/J_F^t.

Another important quantity to be taken into careful consideration is the temperature. The experimental value is in terms of T_F^t, while in our calculations T is always related to the critical temperature T_c evalued within LPDA approach. We have found it reasonable in this case for each coupling to identify T/T_c with the experimental ratio T/T_c^t, where the values of T_c^T/T_F^t for each coupling have been taken from the fully self-consistent t-matrix calculation of Ref. [50] (cf. Fig. 7 therein). This kind of identification is common in condensed matter when comparing theoretical results with experimental data and has already been considered in the context of ultra-cold Fermi gas [51].

In fig. 2.26 we report the comparison between the theoretical results for J_c (shaded area and continous lines) and the corresponding experimental values (dots with errorbars) for three barrier heights and several couplings across the BCS-BEC crossover. The experimental data are taken for $T/T_F^t = 0.06(2)$ [3], which correponds to the low temperature regime, as it can be seen in Tab. 2.2 where the ratios T/T_c used for each coupling are reported. In addition, in Tab. 2.2 the values of κ for each experimental coupling is reported[4] as well as the corresponding theoretical couplings used in the numerical simulation.

The shaded areas in Fig. 2.26 take into account the experimental error in determining of both temperature and barrier width. The upper (lower) border represents the results of J_c obtained at $T/T_F^t = 0.08$ ($T/T_F^t = 0.04$) and a barrier width increased (decreased) by 5% with respect to the nominal value [3]. The continous lines in Fig. 2.26 represent the theoretical results obtained at $T/T_c = 0.06$ and using as Gaussian width of the barrier the nominal value of w.

Looking at Fig. 2.26, we notice an overall agreement between theory and experiment which improves as the barrier height increases. Nevertheless the LPDA results seem to overestimate the value of J_c in general. This fact may be partly due to the fact that in our numerical calculations we are not taking into account neither the dependence of the barrier on the transversal direction to the current flow (since we are considering it to be homogeneous), nor the fact that the fermionic gas is confined in an harmonic trap. Both aspects may contribute to a decrease of the theoretical values of J_c.

[4]The values of E_F^t/E_F were kindly provided by W. J. Kwon (private communication).

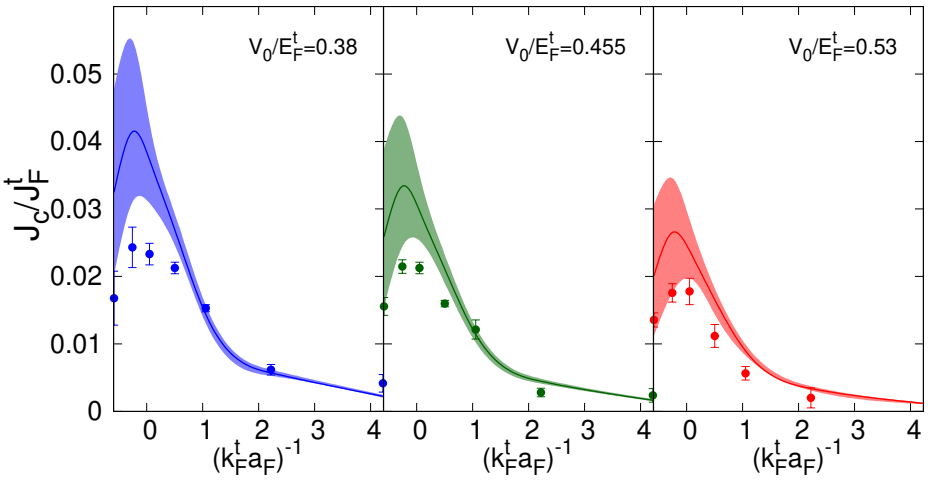

Figure 2.26: Critical current J_c (in units of the trap value J_F^t) vs the experimental coupling parameter $(k_F^t a_F)^{-1}$ for three different barrier heights (in all cases the Gaussian $1/e^2$ width of the barrier is $k_F^t w = 2.530 \pm 0.125$). The experimental data from Ref. [3] (dots with error bars) are compared with the theoretical values represented by the shaded areas, whose boundaries are set by the experimental uncertainties on T/T_F^t and V_0/E_F^t (see the text). For each experimental data point, the values of $(k_F a_F)^{-1}$ and T/T_c at which the theoretical calculations have been performed are listed in Table 2.2. (Reproduced from Ref. [33].)

$(k_F^t a_F)^{-1}$	E_F^t/E_F	$(k_F a_F)^{-1}$	T/T_c
-0.583	0.795	-0.52	0.344
-0.254	0.712	-0.214	0.233
0.0516	0.577	0.039	0.163
0.504	0.511	0.36	0.117
1.055	0.386	0.655	0.076
2.22	0.270	1.15	0.049
4.22	0.206	1.91	0.034

Table 2.2: Conversion from experimental to theoretical coupling values and corresponding theoretical values of T/T_c for $T/T_F^t = 0.06$, used for the comparison shown in Fig. 2.26.

2.9 Analogy between condensed-matter SNS and cold-atoms SS'S Josephson junctions

In this section, we point out an analogy between SNS and SS'S junctions. To this end, we consider for the SS'S junction a slab geometry like that described in Section 2.1, with a potential barrier of height V_0 and width L embedded in an otherwise homogeneous superfluid of critical temperature T_c^S and coupling $(k_F a_F)_S^{-1}$. The SNS junction will instead be modelled by an infinite homogeneous superfluid S (with the same critical temperaure and coupling of the SS'S junction), with the insertion of a different material N for a width L (centered at $x = 0$ like the potential barrier for the SS'S junction (cf. Fig. 2.1)) with a critical temperature $T_c^N < T_c^S$ and coupling $(k_F a_F)_N^{-1} < (k_F a_F)_S^{-1}$. Both $(k_F a_F)_N^{-1}$ and $(k_F a_F)_S^{-1}$ will specifically refer to the BCS side of unitarity, where mean-field results are expected to be more reliable. [By our convention, in both cases the Fermi wavevector k_F refers to the outer superfluid (S) with associated bulk density n].

As a first step in this study we have taken into consideration the GL equation for both the SS'S (cf. (1.57) where $(k_F a_F)^{-1} \to (k_F a_F)_S^{-1}$ and $T_c \to T_c^S$ in the present context) and SNS junctions (cf. (1.57) where $V_0 \to 0$ and $T_c \to T_c^N \theta(L/2 - |x|) + T_c^S \theta(|x| - L/2)$). By comparing the two expressions, we notice that the discontinuity of T_c across the SNS junction corresponds to the following value of the barrier height V_0 for the SS'S junction:

$$\left[1 - \frac{\pi}{4}(k_F a_F)_S^{-1}\right] \frac{V_0}{E_F} = 1 - \left(\frac{T_c^N}{T_c^S}\right)^2 - \frac{T}{T_c^S}\left(1 - \frac{T_c^N}{T_c^S}\right) \tag{2.13}$$

where the temperature T is assumed sufficiently close to T_c^S for the GL equation to be valid.

Figure 2.27 shows the temperature dependence of V_0 as obtained by eq. (2.13) over an extended range of temperature for four different sets of couplings $(k_F a_F)_N^{-1}$ and $(k_F a_F)_S^{-1}$, to which there correpond different ratios T_c^N/T_c^S. It is interesting to notice that for barrier heights within the range of those used in ultra-cold gases experiments (cf. [3, 4]) there correspond ratios of T_c^N/T_c^S that corresponds to condensed-matter SNS junctions (cf. [2]).

In Fig. 2.28 we show the temperature dependence of the critical current J_c for an SNS and SS'S junctions for which the values of $(k_F a_F)_N^{-1}$, $(k_F a_F)_S^{-1}$, and V_0 have been chosen so as to obtain a similar behaviour. The remarkable aspect of this plot is that the values of J_c/J_F obtained for the two junctions overlap each other over three order of magnitude in the range $0 \leq T < T_c^S$.

Fig. 2.29 extends the comparison of Fig. 2.28 to another pair of values $(k_F a_F)_N^{-1}$ and $(k_F a_F)_S^{-1}$. In this case, the temperature dependence of J_c of the SS'S junction is shown for three values of V_0. The good agreement between the values of J_c/J_F covers three orders of magnitude as in the previous case and becomes optimal when the critical current of the SS'S system for increasing values of V_0 are compared with J_c of the SNS junction in the "low", "intermediate", and "high" temperature regimes, in line with the temperature dependence of the effective barrier reported in Fig. 2.27.

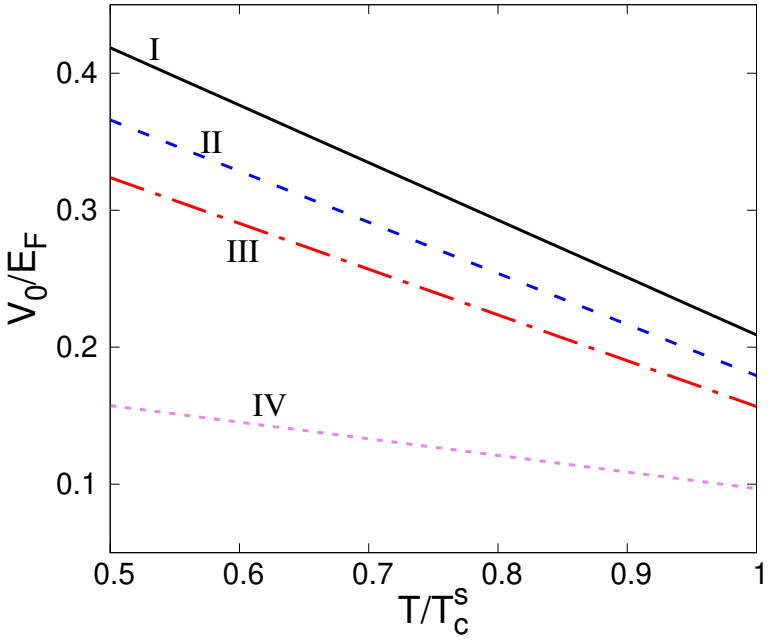

Figure 2.27: Temperature dependence of the barrier height V_0 (in units of the Fermi energy E_F) for an SS'S junction, which would be needed to mimic an SNS junction according to eq. (2.13). The four cases here reported correspond to : (I-full line) $(k_F a_F)_S = -0.25$, $(k_F a_F)_N = -0.50$, $T_c^N/T_c^S = 0.498$; (II-dashed line) $(k_F a_F)_S = -0.5$, $(k_F a_F)_N = -1$, $T_c^N/T_c^S = 0.48$; (III-dashed-dotted line) $(k_F a_F)_S = -0.75$, $(k_F a_F)_N = -1.25$, $T_c^N/T_c^S = 0.469$; (IV-dotted line) $(k_F a_F)_S = -0.85$, $(k_F a_F)_N = -1$, $T_c^N/T_c^S = 0.798$.

In Section 2.4 it was observed that the dependence of J_c on the barrier width L could be modelled by the form (2.7) and it was shown that finite values of $J_c^{\rm mini}$ correspond to the emergence of a "minigap" in the interior of the barrier. Moreover, $J_c^{\rm mini}$ vanished at the same temperature T_c' at which $\Delta_{\rm mini}$ also vanished (cf. Figs. 2.15 and 2.16). For this reason, in the present context of SNS junctions, it is interesting to consider the behaviour of J_c for increasing width of the N region. In panel (a) of Fig. 2.30 the dependence of the critical current on L is shown for different temperatures. The lines are obtained applying the fitting procedure (2.7) to the LPDA results. The dependence of $J_c^{\rm mini}$ on the barrier width is shown in panel (b). Following the arguments of Section 2.4, we would associate to the interior region of the system an effective temperature $0.5T_c^S$ which in practice corresponds to the numerical input setup of $T_c^N/T_c^S = 0.498$. This provides a non-trivial consistency check on our numerical calulations.

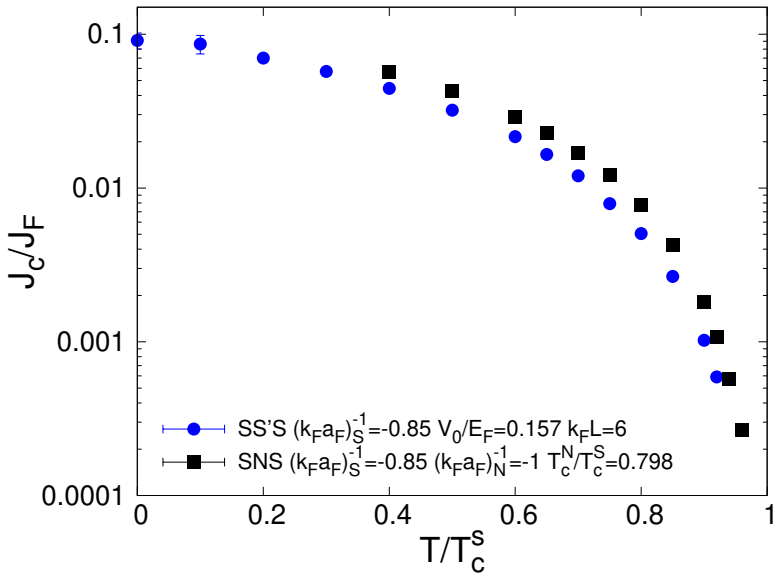

Figure 2.28: Temperature dependence of the critical current J_c (in units of J_F) obtained for an SS'S junction (dots) and an SNS junction (squares) with the same value of the outer coupling $(k_F a_F)_S^{-1}$. Also specified are the values of the barrier height V_0/E_F for the SS'S junction, and the inner coupling $(k_F a_F)_N^{-1}$ and the ratio T_c^N/T_c^S of the critical temperatures for the SNS junction. The value of the slab width $k_F L$ is common to the SS'S and SNS junctions.

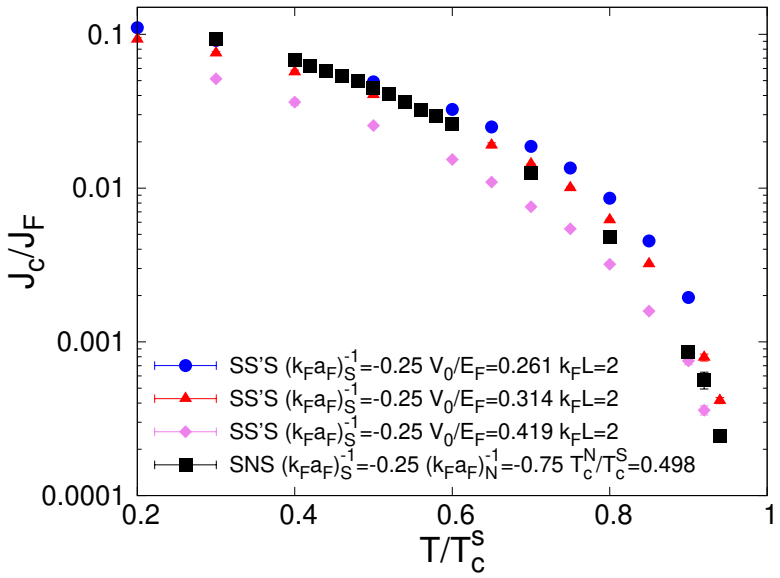

Figure 2.29: The temperature dependence of the critical current J_c (in units of J_F) obtained for three different SS'S junctions (dots, triangles, and diamonds) with given value of the outer coupling $(k_F a_F)_S^{-1}$ and slab width $k_F L$ but different barrier heights V_0/E_F, is compared with the temperature dependence of J_c obtained for an SNS junction (squares) with the same values of the outer coupling and slab width of the SS'S junctions. Also specified are the value of the inner coupling $(k_F a_F)_N^{-1}$ and the ratio T_c^N/T_c^S.

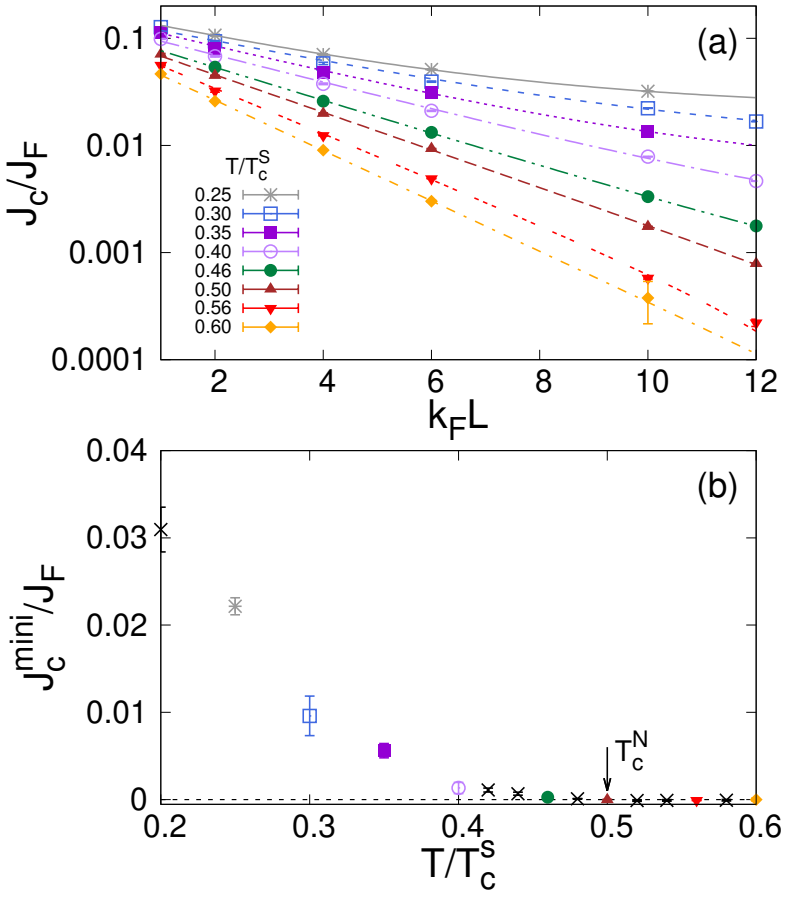

Figure 2.30: (a) Width dependence of J_c (in units of J_F), corresponding to an SNS junction with outer coupling $(k_F a_F)_S^{-1} = -0.25$ and inner coupling $(k_F a_F)_N^{-1} = -0.75$, for several temperatures. (b) Temperature dependence of the minimum value J_c^{mini} attained by J_c. The vertical arrow marks the temperature T_c^N where J_c^{mini} would be expected to vanish.

2.10 Inclusion of pairing fluctuations

In this Section, we show a few early-stage results for the critical current J_c obtained by including pairing fluctuations on top of the LPDA equation.

In Ref. [20] pairing fluctuations were added on top of the mean-field approach in the following way. The gap equation was kept in its form valid at the mean-field level, while the density equation was modified by the inclusion of pairing fluctuations at the level of the t-matrix approximation in the broken-symmetry phase. Following the same line of reasoning, in the present context we retain the LPDA equation (1.49) for the gap parameter $\Delta(\mathbf{r})$ and modify the expressions for the local number density $n(\mathbf{r})$ (1.54) and current density $j(\mathbf{r})$ (1.53) through the inclusion of pairing fluctuations in the spirit of a local-density approach.

As a first test on this procedure, we solved the LPDA equation for the gap parameter $\Delta(\mathbf{r})$ together with the current conservation, where we have introduced the newly found expression for $j(\mathbf{r})$, for the SS'S junctions considered in Section 2.8. We point out that the ratios T/T_c used in this context remain the same as those

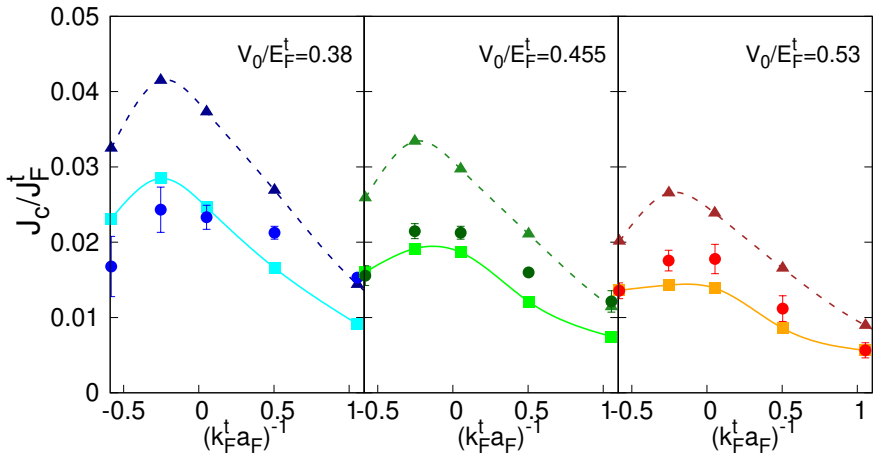

Figure 2.31: Critical current J_c (in units of the trap value J_F^t) vs the experimental coupling parameter $(k_F^t a_F)^{-1}$ for three different barrier heights (in all cases the Gaussian width of the barrier is $k_F^t w = 2.530 \pm 0.125$). The experimental data from Ref. [3] (dots with error bars) are compared with the theoretical values obtained within the mean-field approach (triangles) and with the inclusion of pairing fluctuation (squares) at the experimental nominal temperature $T/T_F^t = 0.06$. For each experimental data point, the values of $(k_F a_F)^{-1}$ and T/T_c at which the theoretical calculations have been performed are listed in Table 2.2.

used at the mean-field level, but the absolute value of the critical temperature T_c is now evaluated whithin the present approach.

Fig. 2.31 shows the comparison among the values of the critical current J_c for three different barriers obtained at the mean-field level (triangles), measured experimentally (circles) [3], and obtained with the inclusion of pairing fluctuations (squares). The triangles and the dotted lines represent the same data of Fig. 2.26 in a restricted coupling region[5]. Looking at Fig. 2.31 we notice that the inclusion of pairing fluctuations leads to lower values of J_c and improves the agreement with the experimental data. Despite this observation, we expect the geometry of the system to play a non-negligible role which could be taken into account in the future by means of a local-density approximation in the transversal direction to the current flow.

Please note that the results reported in this Section are preliminary and need further confirmation.

[5] At the present stage, the values of J_c for $(k_F a_F)^{-1} = [1.15, 1.91]$ (cf. Tab. 2.2) are still to be evaluated.

Chapter 3

Transient Phenomena in a Superfluid Fermi Gas

In this Chapter, we discuss the main results obtained by our study of the dynamics of a two-spin components Fermi system in a 1D box potential. We have considered three different Protocols:

- In Protocol 1, we initially separated the spin-up and spin-down fermions by means of a spin-dependent external potential and then let it vanish in a release time $t_R = 0^+$;
- In Protocol 2, we performed a quench of the inter-particle interaction on a state whose energy corresponds to an effective temperature larger than T_c (as evaluated within a mean-field approach);
- In Protocol 3, we perturbed the ground state at $T = 0$ through a spin-independent external potential with Gaussian shape, whose height was ramped to a maximum and then reduced to a minimum value a certain number of times.

The dynamics of the systems considered for each Protocol was determined by integrating the time-dependent BdG equations using a predictor-corrector algorithm of the 5th order. The BdG functions $u_{\nu\sigma}$ and $v_{\nu\sigma}$ were expanded over the set of functions

$$\phi_n(x) = \sqrt{\frac{2}{L}} \sin\left(\frac{n\pi x}{L}\right) \qquad n = 1, 2, \ldots \tag{3.1}$$

which are the wavefunctions for a particle confined in a 1D box extending from $x = 0$ to $x = L$. In the numerical simulations this expansion is truncated at a certain energy level far enough from the Fermi energy of the system. Further details on the numerical procedure used to integrate the time-dependent BdG equations can be found in Appendix B.

In this context, it is useful to introduce the dimensionless coupling constant [52]

$$\gamma = \frac{mg}{\hbar^2 n} \tag{3.2}$$

being n the total number density. The value $|\gamma| \gg 1$ corresponds to the strong-coupling limit, while $|\gamma| \to 0^+$ to a weak attractive interaction.

The real-time dynamics of the systems described in the following can be observed at the link https://drive.google.com/drive/folders/1-w9nA3MGsIVz0VXc_Om_mZjPkZodEOdw?usp=sharing where various .mp4 files are available for each Protocol.

3.1 Protocol 1

In this Protocol, we begin by separating the spin components using an external potential of the form

$$V_{\text{ext}}^{\sigma}(x) = V_0 \begin{cases} \delta_{\sigma\uparrow}\theta(x - L/2), \\ \delta_{\sigma\downarrow}\theta(L/2 - x), \end{cases} \tag{3.3}$$

where L is the size of the box potential where the fermions are confined. The initial state of this protocol is characterised by a larger number of spin-up (-down) fermions on the left (right) half of the 1D box with respect to the right (left) half. The starting values of $u_{\nu\sigma}$ and $v_{\nu\sigma}$. to be used in (1.38) in order to unveil the dynamics of this system, are found by solving the time-independent BdG equations (1.16) for a fixed number of spin-up and spin-down fermions, $N_\uparrow$ and $N_\downarrow$, respectively.The height V_0 of the potential determines the amount of the separation of the up and down fermions. In practice, a value of $V_0 = 4E_F$ proves sufficient to confine the 99% of $N_\uparrow$ fermions to the left half of the box.

As a first step, we have applied this Protocol of suddenly releasing the external potential ($t_R = 0$) to a non-interacting system. We have found it convenient to define the quantity

$$N_\uparrow^{(L)}(t) = \int_0^{L/2} n_\uparrow(x,t)dx, \tag{3.4}$$

which counts the number of spin-up fermions in the left half of the box at each time t. The $N_\uparrow$ fermions that were initially confined in the left half of the box, after the sudden release of the external potential, experience periodic oscillations in the following sense. The density profile of the $N_\uparrow$ fermions, after an initial spread over the whole box, at a characteristic time t_c rebuilds itself in the right half of the box with a shape which is symmetric to the initial one. Later on, at time $t = 2t_c$, the density profiles recovers the initial shape, with the process going on indefinetely. The characteristic time t_c is independent from the number of fermions and the specific characteristics of the separating potential (as proven in Appendix C). Its value is given by

$$t_c = \pi/\omega_1, \tag{3.5}$$

where ω_1 is the eigenfrequency associated with the ground-state energy of a single particle in the box.

In Fig. 3.1 the quantity $N_\uparrow^{(L)}(t)$ is reported as a function of time for systems with different number of particles. The time dependence of $N_\uparrow^{(L)}(t)$ reflects the oscillatory dynamics of the system. It assumes the initial value $N_\uparrow^{(L)}(0)$ at times $t = lt_c \; \forall l$ even, and the value $1 - N_\uparrow^{(L)}(0)$ at times $t = mt_c \; \forall m$ odd. Moreover, the shape of $N_\uparrow^{(L)}(t)$ for increasing $N_\uparrow$ gets progressively more picked around $t = nt_c \quad \forall n$. At the same time the secondary maxima and minima, right before and after the given time, get less enhanced.

By applying the same Protocol to an interacting system, we have observed a different dynamics. The spin-up (-down) fermions, initially confined in the left (right) half of the box, as soon as the confining external potential is released spread over the whole width L, and at time $t = t_c$ realize a new spin-separation phase, less steep than the starting one, where the spin-up (down) fermions are mostly located

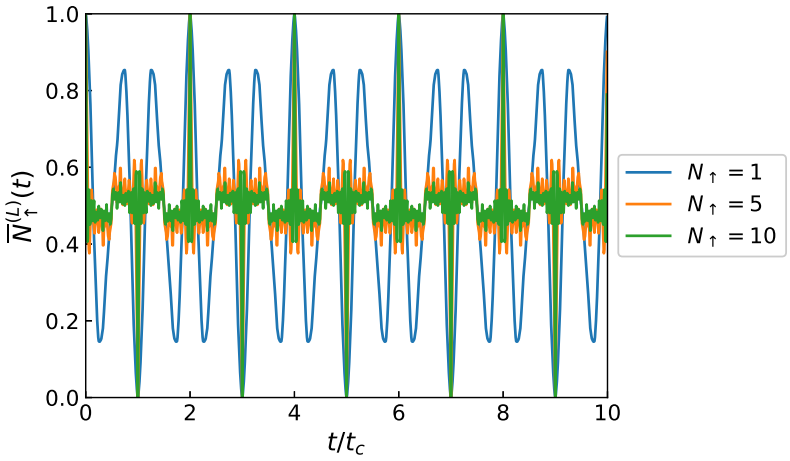

Figure 3.1: Time dependence of $N_\uparrow^{(L)}(t)$ after a sudden release of the external potential for a non-interacting system with $N_\uparrow = 1$ (blue line), $N_\uparrow = 5$ (orange line), and $N_\uparrow = 10$ (green line). To produce the initial state the value $V_0 = 4E_F$ was utilized.

in the right (left) half of the box. Later on, after another spread of the spin-up and spin-down fermions densities over the whole box width, at time $t = 2t_c$ the majority of spin-up (-down) fermions are located in the left (right) half of the box, and so on. This process continues up to a certain time t_e, in correspondence to which spin-up and spin-down densities completely overlap each other and extend over the whole confining box potential. To summarize, we can assert that the main difference between the dynamics of a non-interacting and an interacting system for the present Protocol with $t_R = 0$ consists in the fact that, while the non-interacting system experiences periodic density oscillations, the interacting system is characterized by dumped density oscillations with the same periodicity.

In Fig. 3.2 we report the time dependence of $N_\uparrow^{(L)}$ which we find representative of the dynamics discussed above. This quantity at time $t = lt_c$ $\forall l$ even and small enough experiences local maxima, while at time $t = mt_c$ $\forall m$ odd and small enough experiences local minima. These values, reported in Fig. 3.2 (dots), correspond to a partial restoring of the initial spin separation, which gets less steep as the spin-up and spin-down fermions continue to interact.

From the three panels of Fig. 3.2, we notice that increasing the interaction dampens the density oscillations of the system: The absolute value of $N_\uparrow^{(L)}(t = nt_c)$ $\forall n$ decreased as γ increased. Moreover, the values $N_\uparrow^{(L)}(t = nt_c)$ $\forall n$ can be modelled through

$$\begin{aligned} N_\uparrow^{(L)}(lt_c) &= N_\uparrow^{(L)}(0)e^{-lt_c/t_e} \quad \text{for } l \text{ even} \\ N_\uparrow^{(L)}(mt_c) &= [1 - N_\uparrow^{(L)}(0)]e^{-mt_c/t_e} \quad \text{for } m \text{ odd} \end{aligned} \tag{3.6}$$

in terms of the fitting parameter t_e, which can be identified as the equilibration time in the sense explained above.

We have applied the Protocol 1 with $t_R = 0$ to systems for a large set of values of γ and performed the fitting procedure (3.6) on the corresponding $N_\uparrow^{(L)}(t)$. The results of this analysis are shown in Fig. 3.3, where t_e is shown as a function of

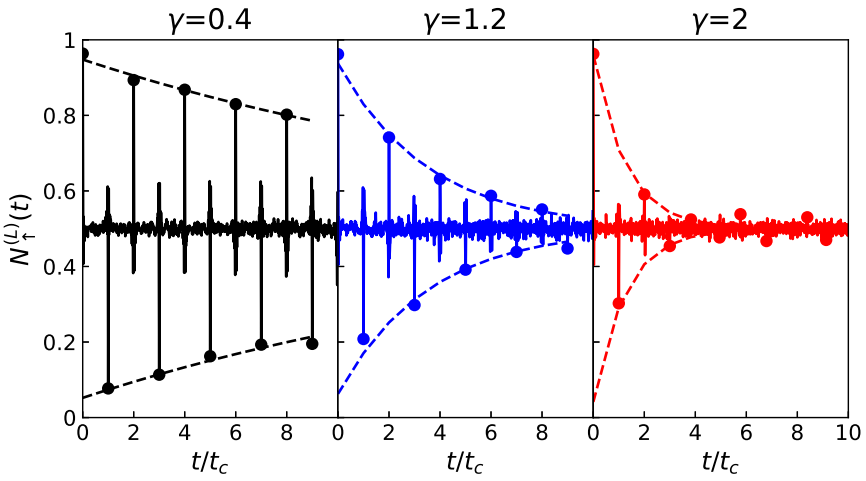

Figure 3.2: Time dependence of $N_\uparrow^{(L)}(t)$ for a sudden release of the separating external potential for an interacting system with 40 fermions ($N_\uparrow = 20$ and $N_\downarrow = 20$) for three different values of coupling constant γ. The continuous lines represent the instanteneous value of $N_\uparrow^{(L)}(t)$, the dots identify the values corresponding to $t = nt_c$ with $n = 1, 2, \ldots$, and the dashed lines represent an exponential fit through the dots.

γ. One sees that the equilibration time results to be inversely proportional to the inter-particle interaction strength γ. Specifically the values of t_e can be modelled through a branch of a hyperbola as shown in Fig. 3.3.

The dynamics discussed so far can be clearly unveiled only when $t_R = 0$ and for a large enough number of fermions, for which it is possible to consider steep initial spin-separations, and for small inter-particle interaction strength. Otherwise, the off-diagonal terms of the BdG equeations (1.38) does not allow us to clearly identify the damped oscillatory dynamics, because the system reaches almost immediately the final equilibrium configuration discussed above. The systems here considered at time $t = 0$ have 97% of spin-up (-down) fermions in the left (right) half of the box when using the value $V_0 = 3.8E_F$ in (3.3).

Choosing finite values for the releasing time t_R of the separating external potential prevents the observation of the dumped oscillatory dynamics described above. In this case, the spin-up and spin-down densities are slowly made to overlap each other and the off-diagonal terms of eq. (1.38) starts to increase immediately.

In particular, for $t_R \to +\infty$ the process is expected to be adiabatic. As a consistency check on our numerical calculations, we verified that the final state for increasing t_R tends indeed to the ground-state of the system with no external potential (apart from the confining box) as found by solving the time-independent BdG equations (1.16).

Following these considerations on the adiabatic limit, the energy E_∞ of the final state for Protocol 1 is expected to be larger than the energy $E_{\rm box}(T = 0)$ of the ground-state at $T = 0$ with no separating external potential. Moreover, the faster the release of the external potential, the more energetic is expected to be the final state. To confirm this expectation, we have studied the dynamics of the system for a large set of values of t_R, obtainig the results shown in Fig. 3.4. The energy E_∞ is

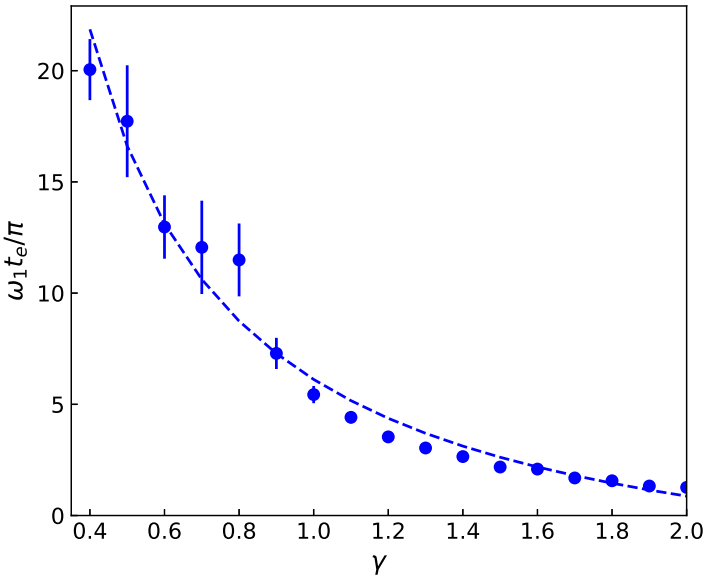

Figure 3.3: Coupling dependence of the equilibration time t_e obtained through the fitting procedure (3.6) for a system of 40 ($N_\uparrow = 20$ $N_\downarrow = 20$) fermions. The dashed line represents the branch of the hyperbola fitting the values of t_e.

found to be a decreasing function of t_R and tends to $E_{\rm box}(T = 0)$ for $t \gg t_c$.

The energy E_∞ can also be used to associate an effective temperature $T_{\rm eff}$ to the final state of Protocol 1. Solving the BdG equations for a system of N fermions confined in a box at finite temperature, we have obtained the relation between the temperature and the energy of the system shown in Fig. 3.5, which can then be used to associate an effective temperature to the final state of Protocol 1. This procedure thus leads us to associate an effective temperature larger than T_c for the final states considered in Fig. 3.4. This result is rather remarkable because the final states here considered have a non-vanishing gap. Metastable states with the same chacteristics, that is $T > T_c$ and finite gap, were experimentally observed in Ref. [22]. We have applied Protocol 1 to the case with $N_\uparrow \neq N_\downarrow$. In particular, we were interested in establishing the differences in dynamics, if any, with respect to the spin-balanced case. The main results of this study are reported in Figs. 3.6 and 3.7.

In Fig. 3.6 the time dependence of $N_\uparrow^{(L)}$ is reported for three cases with $N_\uparrow = 10$ and different values of $N_\downarrow$. Situations with $N_\downarrow < N_\uparrow$, $N_\downarrow = N_\uparrow$, and $N_\downarrow > N_\uparrow$ are considered. The separating external potentials and the interaction constant g are the same in each case, so that the differences in the dynamics in the three cases are due to the imbalance amount of the spin populations. From Fig. 3.6 we note that the initial spin-separation when $N_\downarrow = 5$ is less steep with respect to $N_\downarrow = 10$ and $N_\downarrow = 15$, resulting in a faster dynamic. Namely, when $N_\downarrow = 5$ the equilibrium value 0.5 is reached in a shorter time with respect to the other cases and it is not possible to clearly distinguish the local maxima and minima at $t = lt_c$ for $l = 1, 2 \ldots$ typical of the current Protocol. On the other hand, the case with $N_\downarrow = 15$ has an initial spin separation slightly different from the case with $N_\downarrow = 10$ and the time dependence of $N_\uparrow^{(L)}(t)$ experiences local maxima and minima at the same characteristic times lt_c

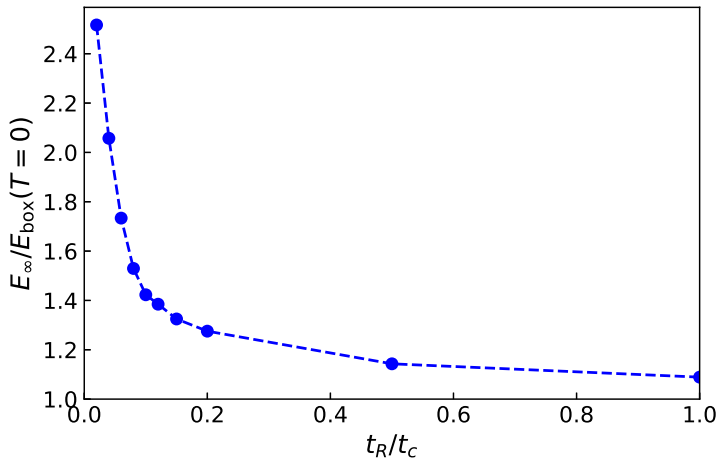

Figure 3.4: Energy of the final state vs the release time t_R of the separating external potential for a system of 20 fermions ($N_\uparrow = 10$ $N_\downarrow = 10$) and $\gamma = 1.05$. The dotted line is a guide to the eye.

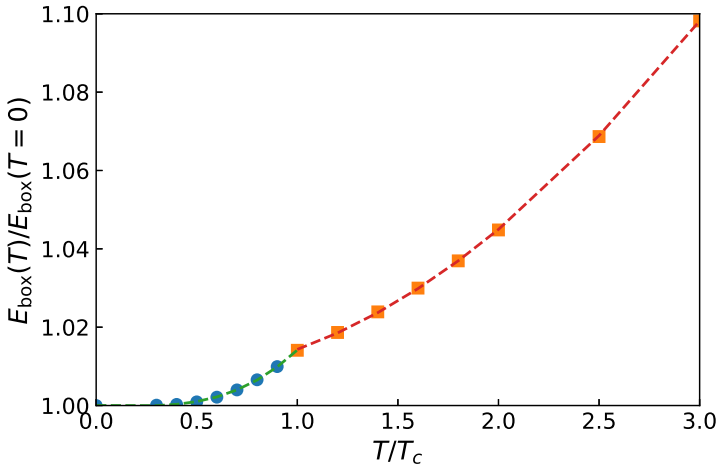

Figure 3.5: Energy of a system of 20 fermions ($N_\uparrow = 10$ $N_\downarrow = 10$) and $\gamma = 1.05$ in units of the energy at $T = 0$ vs the temperature in units of T_c evaluated within the present approach. The blue dots correspond to the values of the energy for $T < T_c$, while the orange squares to the values of the energy for $T \geq T_c$. The green dotted line is the fitting spline of the blue dots, while the red dotted line is the fitting spline of the orange squares.

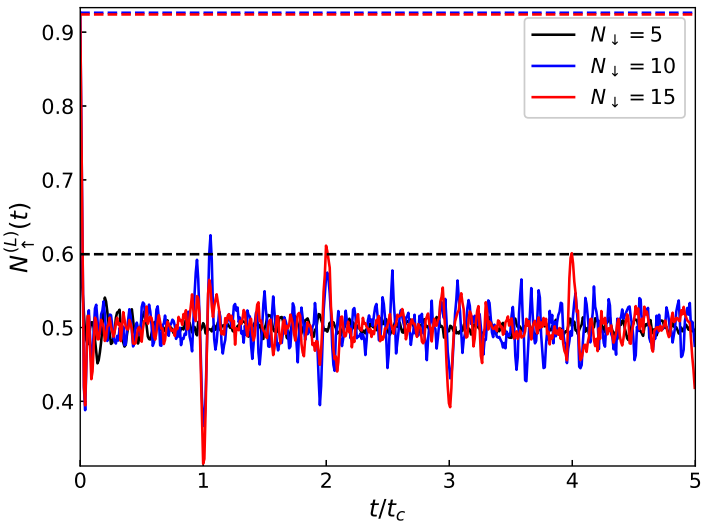

Figure 3.6: Time dependence of $N_\uparrow^{(L)}(t)$ for a sudden release of the separating external potentials for an interacting system with $N_\uparrow = 10$ and three different values of $N_\downarrow$. The dashed lines indicate the value $N_\uparrow^{(L)}(t=0)$ for $N_\downarrow = 5$ (black), $N_\downarrow = 10$ (blue), and $N_\downarrow = 15$ (red). The height of the separating external potentials is $3.6E_F$ in all cases (where E_F refers to the case $N_\uparrow = N_\downarrow = 10$). The interaction constant g is the same in all cases and leads to the values $\gamma = 2.7$ for $N_\downarrow = 5$, $\gamma = 2$ for $N_\downarrow = 10$, and $\gamma = 1.6$ for $N_\downarrow = 15$.

for $l = 1, 2, \ldots$ as the spin-balanced case. The local maxima and minima of $N_\uparrow^{(L)}(t)$ for the case with $N_\downarrow = 15$ are larger in absolute value with respect to those of the spin-balanced case. This leads to a longer equilibration time t_e for the case with $N_\downarrow > N_\uparrow$ with respect to systems with $N_\uparrow = N_\downarrow$. These findings are in agreement with the fact that reducing the value of $N_\downarrow$ results in a larger coupling constant, which are characterised by a faster dynamics, while increasing $N_\downarrow$ leads to smaller coupling constants, which are characterized by a slower dynamics (cf. Fig 3.1).

In studing spin-imbalanced systems it is useful to introduce the quantity $\overline{\Delta}^2(t)$ defined by

$$\overline{\Delta}^2(t) = \frac{1}{L}\int_0^L \frac{|\Delta(x,t)|^2}{E_F^2} dx, \tag{3.7}$$

which enables us to study the time evolution of the superfluid gap. In Fig. 3.7 this quantity is reported for the same cases of Fig. 3.6. From the middle panel of Fig. 3.7 we see that $\overline{\Delta}^2(t)$ for the spin-balanced case quickly reaches a finite value around which it oscillates with no detectable periodicity (cf. right panels in Fig. 3.7). In this case, it is not possible to identify a transient time in a clear manner. The final value about which $\overline{\Delta}^2(t)$ oscillates is slightly smaller than $\overline{\Delta}^2(t=0)$. On the other hand, from the top and bottom panels (with $N_\downarrow = 5$ and $N_\downarrow = 15$, respectively) we note that a transient time is clearly detectable and the final value about which $\overline{\Delta}^2(t)$ oscillates is considerably smaller than $\overline{\Delta}^2(t=0)$ for $N_\downarrow = 5$ and slighlty larger than $\overline{\Delta}^2(t=0)$ for $N_\downarrow = 15$. From a preliminary study we have

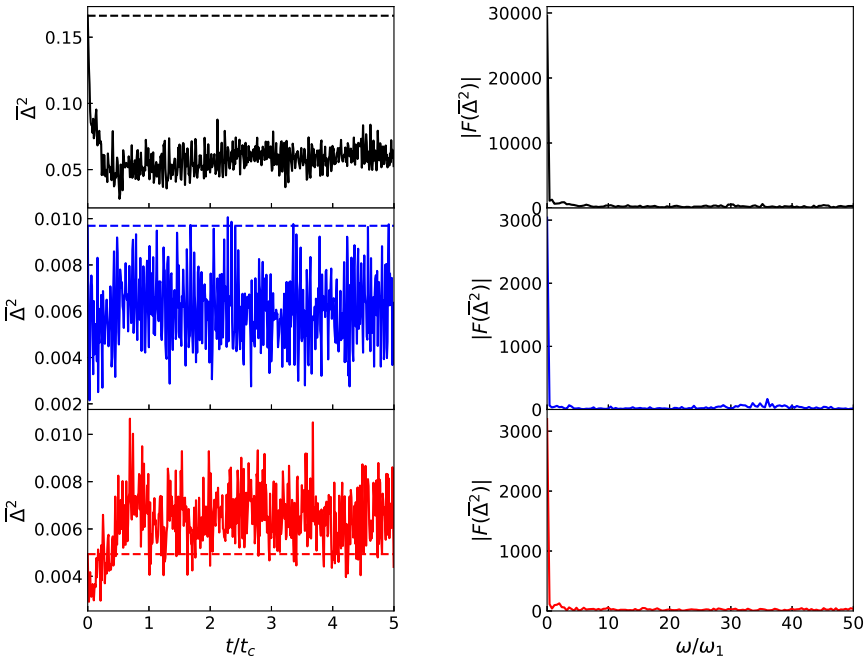

Figure 3.7: Time dependence of $\overline{\Delta}^2$ (left panels) and angular frequency dependence of the absolute value of its Fourier transform $|F(\overline{\Delta}^2)|$ (right panels) for a system with $N_\uparrow = 10$ and $N_\downarrow = 5$ (top panels), $N_\downarrow = 10$ (middle panels), and $N_\downarrow = 15$ (bottom panels) to which Protocol 1 was applied. The dashed line in each panel signals the value $\overline{\Delta}^2(t = 0)$. The separating external potentials and the coupling constant used are the same as in Fig. 3.6.

observed that the transient time of $\overline{\Delta}^2(t)$ and the equilibration time obtained from the time-dependence of $N_\uparrow^{(L)}(t)$ appear to be the same within numerical error. This interesting aspect requires further analysis.

3.2 Protocol 2

In this Protocol, we have performed a quench of the inter-particle interaction on a state whose effective temperature is larger than T_c evaluated within the BdG (mean-field) approach (see Section 3.1 for further details).

Following the procedure used in Ref. [23], in this protocol the dimensionless coupling of the system is ramped linearly to its final value in a time t_q, namely,

$$\gamma(t) = \begin{cases} \gamma_i + (\gamma_f - \gamma_i)\dfrac{t}{t_q} & \text{for} \quad t < t_q \\ \gamma_f & \text{for} \quad t \geq t_q, \end{cases} \tag{3.8}$$

γ_i and γ_f being the initial and final values of the dimensionless coupling, respectively.

Numerical results of this protocol need further analysis.

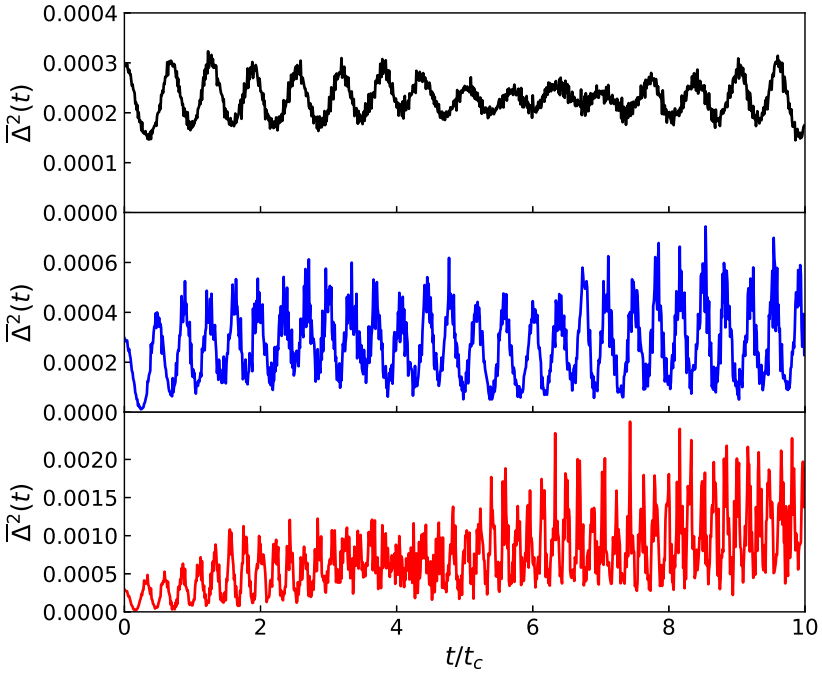

Figure 3.8: Time dependence of $\overline{\Delta}^2$ for a system of $N = 20$ ($N_\uparrow = 10$ $N_\downarrow = 10$) fermions and $\gamma = 1.05$ to which Protocol 3 was applied. The values in the top panel refer to $V_0/E_F = 1$, in the middle panel to $V_0/E_F = 2$, and in the bottom panel $V_0/E_F = 3$. In all cases $t_p/t_c = 0.001$ and $\sigma/L = 0.04$.

3.3 Protocol 3

In this Protocol, we have chosen the external potential to mimic the pump-and-probe experiments [21, 22]. The initial state for this Protocol is the ground state for a system of N fermions confined in a box with dimensionless coupling parameter γ. We perturb (pump) this system by appling a time-dependent external potential of Gaussian shape, whose height $V_{\max}$ varies with time in the following way:

$$V_{\rm ext}(x,t) = V_{\max}(t) e^{-(x-x_0)^2/(2\sigma^2)} \quad \text{with} \quad V_{\max}(t) = V_0 \begin{cases} \dfrac{t}{t_p} & \text{for} \quad t < t_p, \\ \left(2 - \dfrac{t}{t_p}\right) & \text{for} \quad t_p \le t < 3t_p, \\ \left(\dfrac{t}{t_p} - 4\right) & \text{for} \quad 3t_p \le t < 4t_p, \end{cases} \tag{3.9}$$

In Fig. 3.8 we report the evolution of $\overline{\Delta}^2$ over time for different values V_0 of the external Gaussian potential, $x_0 = L/2$ and $t_p = 0.001 t_c$. The quantity $\overline{\Delta}^2$ oscillates in time in a quite regular way and the characteristics of these oscillations are deeply affected by the value V_0. For increasing V_0, both the period and amplitude of the oscillations become larger, as it can be seen from the panels in Fig. 3.8.

The dimensionless coupling constant γ plays an important role in this dynamics.

Increasing the inter-particle interaction makes it not impossibile to identify any periodicity in the time-dependence of $\overline{\Delta}^2$, which oscillates in a random fashion around an equilibrium value.

Another important parameter is t_p (see (3.9). Its value deeply affects the energy of the final state E_∞ (cf. Fig. 3.9) and the dynamics of the system. In particular:

- For $t_p \to 0^+$, $E_\infty \to E_{\rm box}(T=0)$ and in this limit for small enough γ, $\overline{\Delta}^2$ shows periodic oscillations in time. For larger values of γ on the other hand the system is not sensible to the perturbation and experiences only small random oscillations of both density and gap profiles.

- In the "opposite" limit, namely, for $t_p \gg 0$ $E_\infty \to E_{\rm box}(T=0)$, the system for a large enough γ appears to verify the adiabatic limit and after the perturbation recovers the inital density and gap initial profiles, while for smaller values of γ, $\overline{\Delta}^2$ shows periodic oscillations at times $t > 4t_p$. These oscillations are associated with "periodic flattening and steepening of the quasiparticle distribution function" as it happened for the Higgs-like modes described in Ref. [53], but in the present case no damping has been observed in the investigated simulation time.

- For intermediate values of t_p, $\overline{\Delta}^2$ increases and for time $t \gg t_p$ oscillates in time with no detectable periodicity.

In the latter case, an "optimal" value of t_p can be identified that maximizes the ratio $E_\infty/E_{\rm box}(T=0)$. Looking at Fig. 3.9, this "optimal" value does to not depend neither on the inter-particle interaction nor on the height of the Gaussian external potential. These results need further analysis.

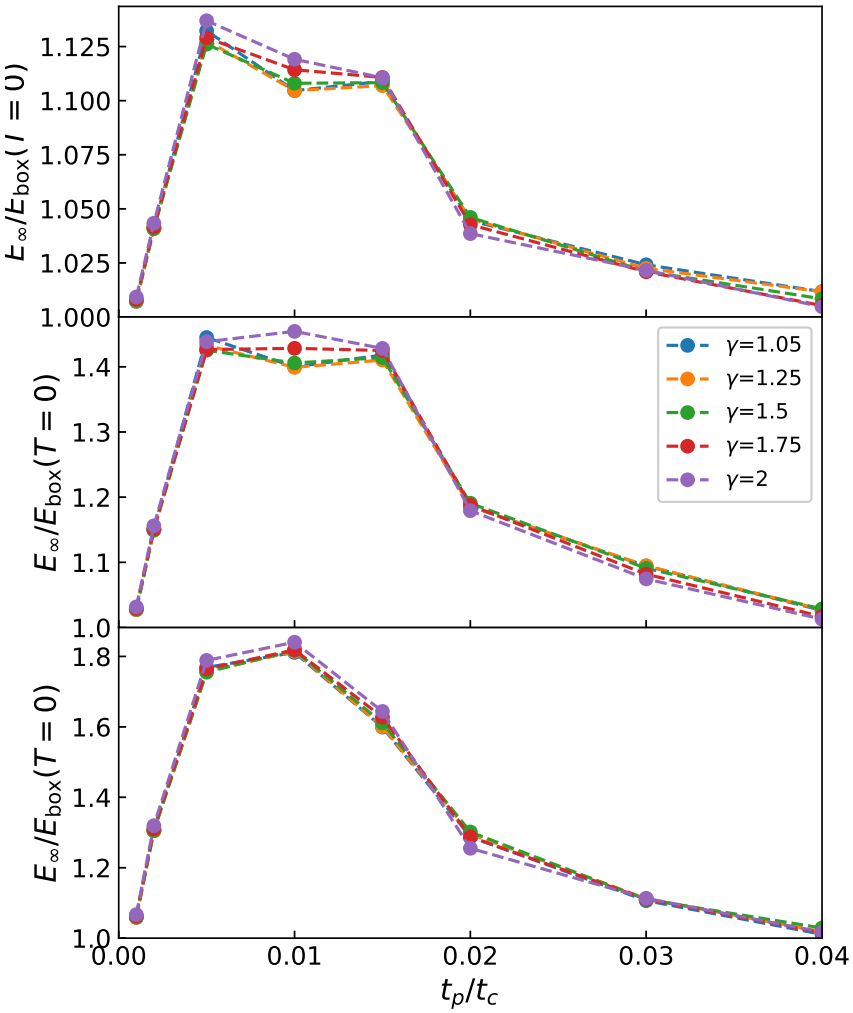

Figure 3.9: Dependence of the energy of the final state E_∞ on time t_p, for a system of $N = 20$ ($N_\uparrow = 10$ $N_\downarrow = 10$) fermions and for a set of values of γ to which Protocol 3 was applied. Values in the top panel refer to $V_0/E_F = 1$, in the middle panel to $V_0/E_F = 2$, and in the bottom panel to $V_0/E_F = 3$. In all cases, $\sigma/L = 0.04$. The legend in the middle panel refers also to the the top and bottom panels. The dotted lines are a guide to the eye.

Chapter 4

Conclusions

In the first part of this work, we have performed a systematic study of the Josephson effect at finite temperature across the BCS-BEC crossover. We have taken into consideration junctions of the type SS'S, where an external potential acts in the internal (S') region of an otherwise homogeneous superfluid. We have solved the LPDA equation, obtained through a coarse-graining of the BdG equations, for various couplings across the BCS-BEC crossover, at temperatures $0 \leq T < T_c$ and for a large set of barriers. The LPDA equation, that is a non-local differential equation for the gap parameter, has allowed this study owing to its reduced complexity with respect to the BdG equations from which it originates. This results in more feasible computation time and reduced memory load needed to extract the physical quantities one is interested in, with respect to the BdG equations.

We have studied the Josephson characteristics and the profiles of the magnitude and phase of the gap parameter varying alternatively and simultaneously coupling, temperature, barrier height, and width. In this way we have obtained the following results: The emergence of the Josephson-induced Proximity effect for increasing barrier width (see Sec. 2.4); The identification on numerical grounds of an extended BCS regime (see Sec. 2.5); The evaluation of the exponent η for the critical current J_c and its dependence on the barrier heights and width (see Sec. 2.6); The extension of the Landau criterion to finite temperature (see Sec. 2.7); A favourable comparison with experimental results currently available for ultra-cold Fermi gases (see Secs. 2.7 and 2.8).

In this work, we have proven that the temperature dependence of the critical current J_c for SS'S and SNS junctions, upon a suitable choice of the physical parameters, are essentially the same in spite of the fact that these junctions constitute two distinct physical systems, for which the changes occuring at the center of the junction affect either single-particle (for the SS'S junction) or two-particle (for the SNS junction) properties. Moreover, we have made a non-trivial consistency check of our calculations based on the Josephson-induced proximity effect introduced in Section 2.4. In this context, we plan to compare our numerical findings with the experimental temperature dependence of J_c shown in Fig. 3 of Ref. [2].

The studies on SS'S and SNS junctions were performed mainly on the BCS side of the crossover, because in that region the mean-field approach, underlying the LPDA equation, is expected to give more reliable results. For increasing temperature and going from BCS to BEC limits of the crossover, pairing fluctuations are expected to play a major role due to the fact that the Cooper pair size in that region becomes

comparable or even smaller than the inter-particle distance. In order to get more reliable results for this portion of the coupling-temperature phase diagram we are developing a procedure to include pairing fluctuations on top of the LPDA equation and currently testing it via a comparison with the available experimental data for the critical current J_c for ultra-cold Fermi gases [3]. We plan to extend this comparison to additional experimental results like those of Ref. [5] for vanishingly small barriers and of Ref. [4] in the unitary regime for increasing temperature.

In the last part of this work, we have developed three out-of-equilibrium Protocols for a system of N fermions confined in a 1D box potential. In Protocol 1 we have separated spatially the spin-up and spin-down fermions using a suitable spin-dependent external potential and studied the dynamics of this system after releasing the external potential either suddenly or by decreasing its height in a time t_R linearly. We have determined the equilibration time t_e for the densities and observed that t_e is inversely proportional to the inter-particle interaction strength. Moreover, we have observed the existence of finite-gap states whose energy corresponds to an effective temperature larger than T_c. We have applied Protocol 1 to spin-imbalanced systems and observed that the equilibration time when $N_\downarrow < N_\uparrow$ systems appears to be smaller than that when $N_\uparrow = N_\downarrow$, while systems with $N_\downarrow > N_\uparrow$ appear to have a slower dynamics with respect to their balanced counterpart. Moreover, while for spin-balanced systems a transient time can not be clearly identified from the time-evolution of the gap parameter, for imbalanced systems it can be clearly determined. In Protocol 2, we have performed a quench of the interaction strength. In this case, the numerical results need further analysis to draw definite conclusions. In Protocol 3, we have perturbated the system by a pulsing Gaussian external potential and observed a different dynamics depending on the inter-particle interaction strength γ. For small values of γ, the gap parameter shows a periodic dependence on time, while for larger values of γ this periodicity is not detectable. Moreover, we have determined the existence of an "optimal" value of the time t_p for perturbing the system, in order to maximize its final energy.

Once the dynamic following the application of Protocol 2 will be determined, we plan to extend the present study with three Protocols to spin imbalanced systems and further to 2D systems.

Appendices

Appendix A

Numerical Procedure for solving the LPDA Equation in the presence of a Supercurrent

In this Appendix, a method is set up for the numerical solution of the LPDA equation (1.49) in the presence of a supercurrent. This method can as well be used to solve directly the GP (1.60) and GL (1.57) equations in their respective domains of validity, thus complementing other numerical methods already available for these cases [54, 55].

For definiteness, we take the supercurrent directed along the x axis and assume translational invariance along the y-z plane. Accordingly, the problem effectively reduces to one dimension and Eq. (1.49) with $A(x) \to Q_0$ simplifies as follows:

$$-\frac{m}{4\pi a_F}\tilde{\Delta}(x) = \mathcal{I}_0(x)\tilde{\Delta}(x) + \frac{\mathcal{I}_1(x)}{4m}\frac{d^2}{dx^2}\tilde{\Delta}(x) + i\mathcal{I}_1(x)\frac{Q_0}{m}\frac{d\tilde{\Delta}(x)}{dx} \tag{A.1}$$

where $\tilde{\Delta}(x) = e^{-2iQ_0x}\Delta(x) \equiv |\tilde{\Delta}|(x)e^{2i\phi(x)}$ and the coefficients $\mathcal{I}_0(x)$ and $\mathcal{I}_1(x)$ are given by the expressions (1.50a) and (1.50b) of the main text, respectively. Through the integrals over the wave vector $\mathbf{k}$ in these coefficients, the system preserves memory of the orthogonal dimensions y and z. In addition, for a symmetric barrier with respect to $x = 0$, the domain of solution of Eq. (A.1) can be restricted to $(0, +\infty)$.

It is further convenient to separate the real and imaginary parts of Eq. (A.1) and introduce the spatial derivatives of $|\tilde{\Delta}|(x)$ and $\phi(x)$. In this way, Eq. (A.1) reduces to a system of four first-order differential equations in the unknown functions $|\tilde{\Delta}|(x)$, $|\tilde{\Delta}|'(x)$, $\phi(x)$, and $\phi'(x)$:

$$|\tilde{\Delta}|' = \frac{d|\tilde{\Delta}|}{dx} \tag{A.2a}$$

$$\phi' = \frac{d\phi}{dx} \tag{A.2b}$$

$$\frac{d|\tilde{\Delta}|'}{dx} = 4|\tilde{\Delta}|\left[\phi'^2 + 2Q_0\phi' - \frac{m}{\mathcal{I}_1}\left(\frac{m}{4\pi a_F} + \mathcal{I}_0\right)\right] \tag{A.2c}$$

$$\frac{d\phi'}{dx} = -2\frac{|\tilde{\Delta}|'}{|\tilde{\Delta}|}(Q_0 + \phi') \tag{A.2d}$$

where the x dependence of the various quantities has been omitted for simplicity. To ensure the solutions to these equations to be physically meaningful, we adopt

the following *boundary conditions*:

$$\begin{aligned} |\tilde{\Delta}|'(x=0) &= 0, & \phi(x=0) &= 0, \\ \lim_{x\to+\infty} |\tilde{\Delta}(x)| &= \Delta_0, & \lim_{x\to+\infty} \phi'(x) &= 0, \end{aligned} \tag{A.3}$$

where Δ_0 is the bulk value of the gap parameter in the presence of the current.

We remark that Eq.(A.2d) entails the local current conservation in both limits of weak coupling and $T \to T_c^-$ [12] (when the LPDA equation recovers the GL equation) and of strong coupling and $T = 0$ [56] (when the LPDA equation recovers the GP equation). However, when the BCS-BEC crossover is spanned at arbitrary temperature in the superfluid phase like in the present context, Eq.(A.2d) does not automatically guarantee current conservation. For this reason, we have followed the strategy adopted in Ref. [9], where the Josephson problem was considered at $T = 0$ throughout the BCS-BEC crossover, and replaced the imaginary part (A.2d) of the gap equation by the condition (2.2) for local current conservation. With the LPDA expression (1.53) for the current, this local condition reads:

$$\begin{aligned} 0 = j(x) - J = &\frac{\phi'(x)}{2m} n(x) + \frac{Q_0}{m}\,(n(x) - n) \\ &+ 2\int \frac{d\mathbf{k}}{(2\pi)^3} \frac{\mathbf{k}}{m} \left[f_F(E_+^{\mathbf{Q}_0}(\mathbf{k}|x)) - f_F(E_+^{\mathbf{Q}_0}(\mathbf{k}|x \to +\infty)) \right] \end{aligned} \tag{A.4}$$

where $\mathbf{Q}_0 = Q_0\hat{x}$, $n(x)$ is the value of the local density given by Eq.(1.54), and n is the corresponding bulk density far away from the barrier. The expression (A.4) depends on $|\tilde{\Delta}|(x)$ and $\phi'(x)$, and can be brought to the form of Eqs. (A.2a)-(A.2c) by moving $\phi'(x)$ to the left-hand side. Finally, as it was done in Ref. [9], the wave vector Q_0 occurring in Eqs. (A.2a)-(A.2c) and (A.4) can also be considered as an independent variable, thereby imposing the additional boundary condition

$$2\phi(+\infty) = \int_0^{+\infty} dx 2\phi'(x) = \frac{\delta\phi}{2} \tag{A.5}$$

that fixes in advance the asymptotic phase difference $\delta\phi$.

A.1 Implementing the implicit Runge-Kutta method

The four equations (A.2a)-(A.2c) and (A.4) to be solved are highly nonlinear in the variables $|\tilde{\Delta}|(x)$, $\phi'(x)$, and Q_0. We have thus found it convenient to solve them through an implicit rather than an explicit Runge-Kutta method, since the latter might be subject to numerical instabilities [57]. Accordingly, we have implemented this method in the following way.

Owing to the spatial localization of the perturbance introduced by the barrier in an otherwise homogeneous superfluid, it is sufficient to restrict the solution of the equations (A.2a)-(A.2c) and (A.4) to a finite interval extending from $x = 0$ to $x = x_{\max}$ (in practice, $x_{\max}$ ranges from $10k_F^{-1}$ to $200k_F^{-1}$, depending on coupling and temperature). The interval $(0, x_{\max})$ is then split into N subintervals (not necessarily

of equal length) identified by an index $\nu = (1, \cdots, N)$, such that $X_{\nu=0} = 0$ and $X_{\nu=N} = x_{\max}$. In each of these subintervals a mesh of K points

$$x_k = X_{\nu-1} + u_k \, (X_\nu - X_{\nu-1}) \qquad (k = 1, \cdots, K) \tag{A.6}$$

is further selected such that $X_{\nu-1} \leq x_k \leq X_\nu$, with the condition $u_{k=1} = 0$ and $u_{k=K} = 1$ on the variables u_k. In this way, each interval $(X_{\nu-1}, X_\nu)$ of variable length is mapped onto the interval $(0, 1)$ of unit length. [In practice, the values $N = 30$ and $K = 5$ have proven sufficient for good numerical convergence of the method.]

With this geometrical setting, the solution of Eqs. (A.2a)-(A.2c) and (A.4) proceeds as follows. Within the ν-th subinterval, these equations have the form

$$\mathbf{y}'(x_k) = \mathbf{g}(\mathbf{y}(x_k), x_k) \tag{A.7}$$

where $\{x_k; k = (1, \cdots, K)\}$ is the mesh of points (A.6) and $\mathbf{y}^T = (|\tilde{\Delta}|, \phi, |\tilde{\Delta}|', \phi')$ refers to the four unknown functions to be determined. The left-hand side of Eq. (A.7) is then represented by the expression

$$\mathbf{y}'(x_k) = \sum_{i=1}^{K} \mathbf{q}_i \, f_i(x_k) \tag{A.8}$$

in terms of K distinct functions $\{f_i(x); i = (1, \cdots, K)\}$, one of which assumes the unit value in correspondence to one of the points $\{x_k\}$, that is to say

$$f_i(x_k) = \delta_{ik}. \tag{A.9}$$

The coefficients $\{\mathbf{q}_i; i = (1, \cdots, K)\}$ of the expansion (A.8), in turn, correspond to the values of the right-hand side of Eq. (A.7), since

$$\mathbf{g}(\mathbf{y}(x_k), x_k) = \sum_{i=1}^{K} \mathbf{q}_i \, f_i(x_k) = \mathbf{q}_k \tag{A.10}$$

for any given k. Within ν-th subinterval, we thus write:

$$\mathbf{y}(x_k) = \mathbf{y}(X_{\nu-1}) + \sum_{i=1}^{K} \mathbf{q}_i \int_{X_{\nu-1}}^{x_k} dx f_i(x) = \mathbf{y}(X_{\nu-1}) + \sum_{i=1}^{K} a_{ki} \mathbf{q}_i \tag{A.11}$$

with the short-hand notation

$$a_{ki} = \int_{X_{\nu-1}}^{x_k} dx f_i(x). \tag{A.12}$$

In particular, for $k = K$ such that $x_K = X_\nu$, Eq.(A.11) becomes

$$\mathbf{y}(X_\nu) = \mathbf{y}(X_{\nu-1}) + \sum_{i=1}^{K} b_i \mathbf{q}_i \tag{A.13}$$

where now

$$b_i = \int_{X_{\nu-1}}^{X_\nu} dx f_i(x). \tag{A.14}$$

The result (A.13) is interpreted as yielding the solution $\mathbf{y}_\nu$ at the left side of the ν-th subinterval in terms of the solution $\mathbf{y}_{\nu-1}$ at the left side of the $(\nu-1)$-th subinterval. Formally, this transfer of information from the $(\nu-1)$-th to the ν-th intervals can be cast in the form $\mathbf{y}_\nu = \mathcal{P}(\mathbf{y}_{\nu-1})$ in term of a "propagator" $\mathcal{P}$.

A convenient choice for the set of variables $\{u_k\}$ and for the functions (A.9) is obtained in terms of the normalized Legendre polynomials $\overline{P}_n(u) = \sqrt{\dfrac{2n+1}{2}} P_n(u)$ where $P_n(u)$ are standard Legendre polynomials [58], such that

$$\int_{-1}^{+1} du \overline{P}_n(u) \overline{P}_{n'}(u) = \delta_{nn'}. \tag{A.15}$$

Let $\{\overline{u}_k; k = (1, \cdots, K)\}$ be the K distinct real zeros of the Legendre polynomial $P_K(u)$, obtained by solving the $K \times K$ eigenvalue problem that results by cyclic application of the recurrence relation $(n+1)P_{n+1}(u) = (2n+1)uP_n(u) - nP_{n-1}(u)$ from $n = 0$ up to $n = K-1$ where $P_{-1}(u) = 0$ (cf., e.g., Appendix B of Ref. [30]). From the normalization of the corresponding eigenvectors one also obtains the weight factors $\{w_k; k = (1, \cdots, K)\}$ that enter the Gaussian quadrature:

$$\int_{-1}^{+1} du \overline{P}_n(u) \overline{P}_{n'}(u) = \sum_{k=1}^{K} \overline{P}_n(\overline{u}_k) \overline{P}_{n'}(\overline{u}_k) w_k = \delta_{nn'}. \tag{A.16}$$

In this way, one defines the orthogonal $(K \times K)$ matrix

$$S_{nk} = \overline{P}_n(\overline{u}_k) \sqrt{w_k} \tag{A.17}$$

such that

$$\sum_{k=1}^{K} S_{nk} S^T_{kn'} = \delta_{nn'} \quad \text{and} \quad \sum_{n=0}^{K-1} S^T_{kn} S_{nk'} = \delta_{kk'}. \tag{A.18}$$

Owing to Eq. (A.17) and the second of Eqs. (A.18), the requirement (A.9) is thus implemented in the form

$$f_i(x_k) = \sqrt{w_i} \sum_{n=0}^{K-1} S^T_{in} \overline{P}_n(\overline{u}_k) = \sqrt{w_i} \sum_{n=0}^{K-1} S^T_{in} \overline{P}_n \left(\frac{2x_k - X_\nu - X_{\nu-1}}{h_\nu} \right) \tag{A.19}$$

where $h_\nu = X_\nu - X_{\nu-1}$ is the length of the ν-th interval. Here, the choice $2u_k = \overline{u}_k + 1$ maps the K roots $\overline{u}_k$ of the polynomial $P_K(u)$ in the interval $(-1, +1)$ into the K values u_k that enter Eq. (A.6) and are restricted to the interval $(0, 1)$. In this way, the coefficients (A.12) become:

$$a_{ki} = \frac{h_\nu}{2} \sqrt{w_i} \sum_{n=0}^{K-1} S^T_{in} \int_{-1}^{\overline{u}_k} dy \overline{P}_n(y) \tag{A.20}$$

where

$$\int_{-1}^{\overline{u}_k} dy \overline{P}_n(y) = \frac{1}{\sqrt{2n+1}} \times \left[\frac{\overline{P}_{n+1}(\overline{u}_k) - \overline{P}_{n+1}(-1)}{\sqrt{2n+3}} - \frac{\overline{P}_{n-1}(\overline{u}_k) - \overline{P}_{n-1}(-1)}{\sqrt{2n-1}} \right] \tag{A.21}$$

which results from the identity

$$(2n+1)P_n(x) = \frac{dP_{n+1}(x)}{dx} - \frac{dP_{n-1}(x)}{dx} \tag{A.22}$$

among the Legendre polynomials [58]. Similarly, an expression like (A.20) holds for the coefficients (A.14), where the upper end of the integral in Eq. (A.21) is now $+1$.

A.2 Successive steps of the Newton method

There remains to apply a multi-dimensional Newton method for solving Eq. (A.10), within each of the N subintervals in which the domain $(0, x_{\max})$ of the solution of this equation has been partitioned, as well as to solve Eq. (A.13) that connects adjacent subintervals. Accordingly, two successive steps have been set up for achieving the self-consistency of the solution. *First step* - With the help of Eqs. (A.6) and (A.11), Eq. (A.10) is cast in the form

$$\mathbf{g}\left(\mathbf{y}(X_{\nu-1}) + \sum_{i=1}^{K} a_{ki}\mathbf{q}_i, X_{\nu-1} + h_\nu u_k\right) - \mathbf{q}_k = 0 \tag{A.23}$$

where $\nu = (1, \cdots, N)$ identifies the ν-th subinterval and $k = (1, \cdots, K)$ the mesh of points in each subinterval. For any given ν in Eq. (A.23), the K vectors $\{\mathbf{q}_i\}$ (each of 4 dimensions) are considered unknown, while the values of $\mathbf{y}(X_{\nu-1})$ as well as the value of Q_0 are guessed beforehand as inputs of the calculation. One cycle of Newton method is then applied to determine the values of $\{\mathbf{q}_i\}$. *Second step* - Once the quantities $\{\mathbf{q}_i\}$ have been determined in this way for any given ν, their values are inserted into Eq.(A.13) which can be rewritten in the compact form

$$\mathbf{y}_\nu = \mathcal{P}(\mathbf{y}_{\nu-1}) \quad \text{with} \quad \nu = (1, \cdots, N). \tag{A.24}$$

These $4N$ equations contain $(N+1)$ sets of 4-dimensional unknown quantities $\mathbf{y}_\nu$, since $\mathbf{y}_{\nu=0}$ at the left edge of the interval $(0, x_{\max})$ has also to be taken into account. Including in $\mathbf{y}_{\nu=0}$ also the value of Q_0 that has to be self-consistently determined, the required additional equations are supplied by the five boundary conditions (A.3) and (A.5). One cycle of Newton method is then applied to determine the values of $\{\mathbf{y}_\nu; \nu = (0, \cdots, N)$. *Cycling back and forth* - Once the quantities $\{\mathbf{y}_\nu; \nu = (0, \cdots, N)\}$ have been determined in this way, their values are fed back into the first step above and new values for the quantities $\{\mathbf{q}_i\}$ are determined from Eq. (A.23) through a second cycle of Newton method. These values of $\{\mathbf{q}_i\}$ are then fed into the second step above, and new values of $\{\mathbf{y}_\nu\}$ (including Q_0) are in turn obtained. Typically $5 - 30$ (depending on coupling and temperature) cycles of this two-step Newton method are required to eventually achieve full self-consistency.

In practice, the initial values of $\{\mathbf{y}_\nu^T\}$ are taken to be $(|\tilde{\Delta}| = \tilde{\Delta}_0, \phi = 0, |\tilde{\Delta}|' = 0, \phi' = 0)$ irrespective of ν, as well as $Q_0 = 0$, where $\tilde{\Delta}_0$ is the value of the gap parameter in the absence of the barrier. In this way, the value $\delta\phi = 0$ is initially assumed for the boundary condition (A.5). Cycling back and forth between the first and second steps above produces eventually a nontrivial spatial profile for $|\tilde{\Delta}|(x)$, although still with $\phi(x) = 0$. This profile is then taken as input for determining the next value of the Josephson characteristic for a non-vanishing value of $\delta\phi$ and the corresponding value of Q_0. The process is repeated several times for increasing values of $\delta\phi$.

A.3 Two types of cycles of the Newton method

The numerical method just described is computationally quite demanding, to the extent that it becomes progressively more difficult to reach convergence for increas-

ing values of $\delta\phi$. This is especially true when considering the decreasing branch of the Josephson characteristics in order to approach the limiting value $\delta\phi = \pi$.

Under these circumstances, we found it more convenient to alternate two types of cycles while searching for the solution, namely, a first type of cycle when $\delta\phi$ is fixed and Q_0 is consistently determined as described above, and a second type of cycle when Q_0 is instead fixed and $\delta\phi$ is consistently determined. In the latter case, the boundary condition (A.5) is removed from the second step above and $\delta\phi$ is obtained by integrating the spatial profile of $\phi'(x)$. At the same time, Q_0 is fixed at the value previously obtained by performing the first type of cycle. The new solution, attained in this way by performing the second type of cycle, is then used back as input for the first type of cycle. Typically, repeating this procedure a couple of times proves sufficient.

A.4 Further numerical insights

The LPDA equation (A.1) contains the local coefficients $\mathcal{I}_0(x)$ and $\mathcal{I}_1(x)$, which have to be determined from the expressions (1.50a) and (1.50b) with sufficient numerical accuracy at each step of the Newton method. Comparable accuracy is also required to determine the local number density $n(x)$ and current $j(x)$ that enter the condition (A.4). This is because the presence of numerical noise may render the convergence of the whole method quite difficult and sometimes even impossible to reach. For these reasons, before starting the convergence procedure described above, all these quantities have been accurately evaluated over a regular grid of points in the variables $(|\Delta|, \mu, Q_0)$, and a tri-linear interpolation has been utilized to determine the actual values of these quantities needed at each iteration of the Newton method.

In practice, for a Josephson characteristics with a mesh of 50 values of $\delta\phi$, the computational time ranges from 100 to 800 minutes, 15 minutes of which are used for the calculation of the coefficients $\mathcal{I}_0(x)$ and $\mathcal{I}_1(x)$ of the LPDA equation over the above three-dimensional grid $(|\Delta|, \mu, Q_0)$. This wide range of computational time reflects the convergence of a single profile $\Delta(x)$ for given $\delta\phi$, which may require from a few seconds up to 20 minutes depending on the settings. The computer code (with no parallelization) was run on a devise with 3000 Mhz CPU speed, 187 GB RAM memory, 15 GB swap memory, 1 GB/s writing speed, and 250 MB/s reading speed.

Appendix B

Numerical Procedure for solving the BdG equations and their time-dependent version

In this Appendix, a method is described for the numerical solution of the BdG equations (1.16) and for the integration of their time-dependent version (1.38).

In Chapter 3 we considered systems confined in a 1D box potential. For this reason, we found it convenient to expand the wave functions $u_{\nu\sigma}$ and $v_{\nu\sigma}$ in the basis set of eq. (3.1). This procedure allows us to express the wave functions $u_{\nu\sigma}$ and $v_{\nu\sigma}$ in terms of a finite set of coefficients as follows:

$$\begin{cases} u_{\nu\uparrow}(x) = \sum_n^M a_n^\nu \phi_n(x) \\ v_{\nu\downarrow}(x) = \sum_n^M b_n^\nu \phi_n(x). \end{cases} \tag{B.1}$$

Here, the coefficients a_n^ν and b_n^ν obey the normalization condition

$$\sum_n \left(|a_n^\nu|^2 + |b_n^\nu|^2 \right) = 1 \tag{B.2}$$

for any values of ν in order for the $u_{\nu\sigma}$ and $v_{\nu\sigma}$ to satisfy the closure relation (1.9).

Introducing the expressions (B.1) in eq. (1.16) and projecting on the $\overline{n}$-th element of the set (3.1), we obtain the equations for the coefficients a_n^ν and b_n^ν:

$$\begin{aligned} \left(\frac{\hbar^2 k_{\overline{n}}^2}{2m} - \mu_\uparrow \right) a_{\overline{n}}^\nu + \sum_n a_n^\nu \int_0^L dx \phi_{\overline{n}}(x) V_{\text{ext}}^\uparrow(x) \phi_n(x) \\ - \sum_n b_n^\nu \int_0^L dx \phi_{\overline{n}}(x) \Delta(x) \phi_n(x) = E_\nu a_{\overline{n}}^\nu, \end{aligned} \tag{B.3a}$$

$$\begin{aligned} \left(-\frac{\hbar^2 k_{\overline{n}}^2}{2m} + \mu_\downarrow \right) b_{\overline{n}}^\nu - \sum_n b_n^\nu \int_0^L dx \phi_{\overline{n}}(x) V_{\text{ext}}^\uparrow(x) \phi_n(x) \\ - \sum_n a_n^\nu \int_0^L dx \phi_{\overline{n}}(x) \Delta^*(x) \phi_n(x) = E_\nu b_{\overline{n}}^\nu, \end{aligned} \tag{B.3b}$$

where k_n is the wavevector associated to the n-th wavefunction of the set (3.1).

It is convenient to rearrenge eqs. (B.3) in matrix form as follows:

$$\left(\begin{array}{ccc|ccc} \hbar^2k_1^2-\mu_\uparrow+V_{11}^\uparrow & \dots & V_{1M}^\uparrow & -\Delta_{11} & \dots & -\Delta_{1M} \\ \vdots & \ddots & \vdots & \vdots & \dots & \vdots \\ V_{M1}^\uparrow & \dots & \hbar^2k_N^2-\mu_\uparrow+V_{MM}^\uparrow & -\Delta_{M1} & \dots & -\Delta_{MM} \\ \hline -\Delta_{11}^* & \dots & -\Delta_{1M}^* & -\hbar^2k_1^2+\mu_\uparrow-V_{11}^\downarrow & \dots & -V_{1M}^\downarrow \\ \vdots & \dots & \vdots & \vdots & \ddots & \vdots \\ -\Delta_{M1}^* & \dots & -\Delta_{MM}^* & -V_{M1}^\downarrow & \dots & -\hbar^2k_N^2+\mu_\uparrow-V_{MM}^\downarrow \end{array}\right)\begin{pmatrix} a_1^\nu \\ \vdots \\ a_M^\nu \\ - \\ b_1^\nu \\ \vdots \\ b_M^\nu \end{pmatrix} = E_\nu \begin{pmatrix} a_1^\nu \\ \vdots \\ a_M^\nu \\ - \\ b_1^\nu \\ \vdots \\ b_M^\nu \end{pmatrix}, \quad \text{(B.4)}$$

where the matrix elements $V_{nn'}^\sigma$ and $\Delta_{nn'}$ are defined by

$$V_{nn'}^\sigma = \int_0^L dx \phi_n(x) V_{\text{ext}}^\sigma(x) \phi_{n'}(x), \quad \text{(B.5a)}$$

$$\Delta_{nn'} = \int_0^L dx \phi_n(x) \Delta(x) \phi_{n'}(x). \quad \text{(B.5b)}$$

The integral in eq. (B.5a) involving two sin functions was solved analitically in Protocol 1 and numerically in Protocol 3. The integral in eq. (B.5b) involving four sin functions (two of them being hidden in the gap parameter, cf. eq. (1.17)) was solved analitically for all Protocols.

Equation (B.4), for given $N_\uparrow$ and $N_\downarrow$, was used to determine the initial state of both Protocols 1 and 3. The unknowns in this equation are the set of coefficients a_n^ν and b_n^ν, which determine also the gap parameter and the chemical potentials $\mu_\uparrow$ and $\mu_\downarrow$. We have solved eq. (B.4) by using the following iterative procedure:

1. make an initial guess for $\mu_\uparrow$ and $\mu_\downarrow$;
2. make an initial guess on the coefficients $\Delta_{nn'}^{(i)}$;
3. solve the eigenvalue problem for the matrix in eq. (B.4) and rescale the eigenvectors, namely a_n^ν and b_n^ν, by a common factor in order to satsfy the normalization condition (B.2);
4. evalute the new $\Delta_{nn'}^{(i+1)}$ using the just found a_n^ν and b_n^ν coefficients;
5. check whether the condition $\sum_{n,n'} |\Delta_{nn'}^{(i+1)} - \Delta_{nn'}^{(i)}| / \sum_{n,n'} |\Delta_{nn'}^{(i)}| < 10^{-6}$ is satisfied; otherwise, introduce $\Delta_{nn'}^{(i+1)}$ in (B.4) and repeat steps 3→5 until the self-consistency is achieved,
6. evalute $N_\uparrow$ and $N_\downarrow$ in terms of the coefficients a_n^ν and b_n^ν by analitically integrating the expression (1.18a);
7. check whether $N_\uparrow$ and $N_\downarrow$ are the desired values within 10^{-6} accuracy; otherwise modify $\mu_\uparrow$ and $\mu_\downarrow$ accordingly and repeat steps 3→7 until the condition is eventually verified.

The coefficients a_n^ν and b_n^ν, as well as the chemical potentials $\mu_\uparrow$ and $\mu_\downarrow$, solution of eq. (B.4) for given $N_\uparrow$ and $N_\downarrow$ fermions, depend on the number M of functions used in the expansion (B.1). We have verified that both the chemical potentials and the average gap parameter in the 1D box approach a limiting value for increasing

M. We have chosen the number M of functions for the expansion in eq. (B.1) such that the limiting value of the average gap parameter is recovered within 5%. The energy associated to this cutoff corresponds to about $100E_F$ for spin-balanced systems and is in line with the values of the cutoff energy utilized in the literature [59]. In this respect, results corresponding to a smaller energy cutoff, which can be obtained faster though quantitatively not totally accurate, may provide useful qualitative insights in a reduced computational time.

To integrate the time-dependent BdG equations, we found it convenient to rewrite the wave functions $u_{\nu\sigma}$ and $v_{\nu\sigma}$ in (1.38) in the form

$$\begin{cases} u_{\nu\uparrow}(x,t) = \sum_{n=1}^{M} a_n^\nu(t) e^{i\omega_n t}\phi_n(x) \\ v_{\nu\downarrow}(x,t) = \sum_{n=1}^{M} b_n^\nu(t) e^{-i\omega_n t}\phi_n(x) \end{cases} \tag{B.6}$$

where ω_n are the eigenfrequencies associated with the n-element of the basis (3.1). The introduction of the factors $e^{\pm i\omega_n t}$ stems from the fact that they correspond to the time-dependence of the non-interacting system and prevent the numerical integration of the equations to numerically diverge. In both Protocol 1 and Protocol 3, $a_n^\nu(t=0) = a_n^\nu$ and $b_n^\nu(t=0) = b_n^\nu$, where a_n^ν and b_n^ν are the coefficients solution of eq. (B.4) for fixed $N_\uparrow$ and $N_\downarrow$.

In practice, the time-dependent BdG equations (1.38), with the expansions (B.6) for $u_{\nu\sigma}$ and $v_{\nu\sigma}$ corresponds to eq. (B.4) where

$$a_n^\nu \to a_n^\nu(t)e^{i\omega_n t}, \qquad b_n^\nu \to b_n^\nu(t)e^{-i\omega_n t}, \qquad E_\nu \to i\hbar\frac{d}{dt}.$$

They are a set of coupled first order differential equations for the complex coefficients $a_n^\nu(t)$ and $b_n^\nu(t)$. We have integrated these equations by means of a predictor-corrector (PEC) algorithm. Accordingly, we have chosen a carefully selected time step Δt and used the Runge-Kutta method to predict the values of the coefficients $a_n^\nu(t_i)$ and $b_n^\nu(t_i)$ (where $t_i = i\Delta t$)for $i = 1, \ldots, 4$, while for later times ($i > 4$) we have used the Adam-Bashforth method [60] in combination with the Adam-Moulton method [60] to find $a_n^\nu(t_i)$ and $b_n^\nu(t_i)$. Upon writing the set of first-order differential equations that we are solving in the form

$$\frac{d\mathbf{y}}{dt} = \mathbf{F}(t, \mathbf{y}), \tag{B.7}$$

where $\mathbf{y}$ is the column vector whose elements are the coefficients a_n^ν and b_n^ν, the Adam-Bashforth method used in the Predict-Evaluate step of PEC algorithm is

$$\begin{aligned} \mathbf{y}(t_{i+5}) =& \mathbf{y}(t_{i+4}) + \Delta t \left[\frac{1901}{720}\mathbf{F}(t_{i+4}, \mathbf{y}(t_{i+4})) - \frac{2774}{720}\mathbf{F}(t_{i+3}, \mathbf{y}(t_{i+3})) \right. \\ &\left. + \frac{2616}{720}\mathbf{F}(t_{i+2}, \mathbf{y}(t_{i+2})) - \frac{1274}{720}\mathbf{F}(t_{i+1}, \mathbf{y}(t_{i+1})) + \frac{251}{720}\mathbf{F}(t_i, \mathbf{y}(t_i)) \right]; \end{aligned} \tag{B.8}$$

while the Adam-Moulton method used in the Correct step of PEC algorithm is

$$\begin{aligned} \mathbf{y}(t_{i+4}) =& \mathbf{y}(t_{i+3}) + \Delta t \left[\frac{251}{720}\mathbf{F}(t_{i+4}, \mathbf{y}(t_{i+4})) + \frac{646}{720}\mathbf{F}(t_{i+3}, \mathbf{y}(t_{i+3})) \right. \\ &\left. - \frac{264}{720}\mathbf{F}(t_{i+2}, \mathbf{y}(t_{i+2})) + \frac{106}{720}\mathbf{F}(t_{i+1}, \mathbf{y}(t_{i+1})) - \frac{19}{720}\mathbf{F}(t_i, \mathbf{y}(t_i)) \right]. \end{aligned} \tag{B.9}$$

The PEC algorithm was preferred to the Runge-Kutta method because, by keeping in memory the values of $\mathbf{y}$ at the previous time steps, it requires only one evaluation of $\mathbf{F}$ per time t_i, with respect to the four which would be needed by the Runge-Kutta algorithm. We have checked that, for the same time step Δt, the numerical accuracy of the two methods is practically the same.

As a final remark on the method used to integrate the time-dependent BdG equations, we point out that the chosen time step Δt considerably affects the conservation in time of the normalization of the coefficients $a_n^\nu(t)$ and $b_n^\nu(t)$ (B.2). Moreover, the larger the number of M functions used in (B.6), the smaller Δt needs to be. A reasonable criterion in this respect is setting $\Delta t = 2\pi/50\omega_M$, which guarantees the conservation of the normalization condition (B.2) within a 10^{-3} accuracy for evolution times up to $5000\hbar/E_F$.

Appendix C

Recurrence Time of a Non-Interacting N-Fermion System

A characteristic feature of the fermionic system embedded in a one-dimensional box with hard walls at $x = 0$ and $x = L$, whose time evolution we have studied in detail numerically in Section III in terms of the TDBdG equations, was that in the absence of inter-particle interaction the fermionic densities for both spins were bouncing back and forth with a definite period if they were initially prepared, say, in only half of the box. In this Appendix, we are going to determine an analytic expression for this recurrence time, by considering a system of a N non-interacting (spinless) fermions system subject to Pauli principle.

Suppose that the N non-interacting fermions are initially confined to a "left" (ℓ) segment of width QL, extending from $x = 0$ to $x = QL$ with $Q < 1$. The (normalized) single-particle wave functions corresponding to this initial configuration are given by

$$\phi_{n_\ell}^{(\ell)}(x) = \sqrt{\frac{2}{QL}} \sin\left(\frac{n_\ell \pi x}{QL}\right) \qquad (n_\ell = 1, 2, \dots) \tag{C.1}$$

such that $\phi_{n_\ell}^{(\ell)}(x = 0) = \phi_{n_\ell}^{(\ell)}(x = QL) = 0$ for all n_ℓ. In addition, each of these wave functions vanishes for $x > QL$. Correspondingly, the N-fermion density associated with this initial ($t = 0$) ground-state configuration reads:

$$n(x, t = 0) = \sum_{n_\ell=1}^{N} |\phi_{n_\ell}^{(\ell)}(x)|^2. \tag{C.2}$$

Suppose now that at $t = 0^+$ this system is suddenly released from the segment and let free to expand over the entire box from $x = 0$ to $x = L$. Each of the N eigenfunction occurring in the expression (C.2) will then evolve in time as follows ($t > 0$):

$$\phi_{n_\ell}^{(\ell)}(x, t) = \sum_n \left[\int_0^{QL} dx' \phi_{n_\ell}^{(\ell)}(x') \phi_n^*(x')\right] \phi_n(x) e^{-i\epsilon_n t/\hbar} \tag{C.3}$$

where $\phi_n(x)$ are the wave functions extending to the entire box from $x = 0$ to $x = L$ (introduce in the main text) and

$$\epsilon_n = \frac{\hbar^2 \pi^2 n^2}{2mL^2} \tag{C.4}$$

are the corresponding eigenvalues (m being the fermion mass). The coefficients in Eq. (C.3) can be readily brought to the form

$$\int_0^{QL} dx \phi_{n_\ell}^{(\ell)}(x) \phi_n^*(x) = 2\sqrt{Q} \int_0^1 \sin(n_\ell \pi y) \sin(n\pi Q y). \tag{C.5}$$

Let's now consider the symmetric "right" (r) segment also of width QL, extending from $x = (1-Q)L$ to $x = L$. If the N fermions were confined to this segment, their wave functions would be given by

$$\phi_{n_r}^{(r)}(x) = \sqrt{\frac{2}{QL}} \sin\left[\frac{n_r \pi}{QL}(x - (1-Q)L)\right] \qquad (n_r = 1, 2, \dots) \tag{C.6}$$

such that $\phi_{n_r}^{(r)}(x = (1-Q)L) = \phi_{n_r}^{(r)}(x = L) = 0$ for all n_r (with the understanding that these wave functions vanish for $x < (1-Q)L$). Each wave function (C.6) can be represented in terms of the wave functions $\phi_n(x)$ for the entire box from $x = 0$ to $x = L$, by writing

$$\phi_{n_r}^{(r)}(x) = \sum_n \left[\int_{(1-Q)L}^{L} dx' \phi_{n_r}^{(r)}(x') \phi_n^*(x')\right] \phi_n(x) \tag{C.7}$$

where

$$\int_{(1-Q)L}^{L} dx \phi_{n_r}^{(r)}(x) \phi_n^*(x) = (-1)^{n_r+n} 2\sqrt{Q} \int_0^1 \sin(n_r \pi y) \sin(n\pi Q y). \tag{C.8}$$

By comparing the results (C.5) and (C.8), we obtain that

$$\int_0^{QL} dx \phi_m^{(\ell)}(x) \phi_n^*(x) = (-1)^{m+n} \int_{(1-Q)L}^{L} dx \phi_m^{(r)}(x) \phi_n^*(x) \tag{C.9}$$

for $n_\ell = n_r = m$.

On the other hand, the time-dependent factor $e^{-i\epsilon_n t/\hbar}$ in the expression (C.3) also equals $(-1)^n$ for a characteristic time t_c such that $\epsilon_n t_c/\hbar = \pi n^2$, that is to say,

$$t_c = \frac{2mL^2}{\pi\hbar} = \frac{\pi\hbar}{\epsilon_{n=1}}. \tag{C.10}$$

With the results (C.9) and (C.10), each time-dependent function (C.3) becomes for $t = t_c$:

$$\begin{aligned} \phi_{n_\ell=m}^{(\ell)}(x, t_c) &= \sum_n (-1)^{m+n} \left[\int_{(1-Q)L}^{L} dx' \phi_{n_r=m}^{(r)}(x') \phi_n^*(x')\right] \phi_n(x) (-1)^n \\ &= (-1)^m \phi_{n_r=m}^{(r)}(x, t_c). \end{aligned} \tag{C.11}$$

When this result is eventually used in the expression of the number density $n(x,t)$ that develops in time from its initial value (C.2) at $t = 0$, we then obtain that at time $t = t_c$

$$n(x, t = t_c) = \sum_{n_\ell=1}^{N} \left|\phi_{n_\ell}^{(\ell)}(x, t = t_c)\right|^2 = \sum_{m=1}^{N} \left|\phi_m^{(r)}(x)\right|^2. \tag{C.12}$$

In conclusion we have proved that, if the density profile of a non-interacting N-fermion system is initially confined within the left segment $0 \leq x \leq QL$ (with $Q < 1$) and then at $t = 0$ let to expand freely over the whole box $0 \leq x \leq L$, after a characteristic time t_c given by the expression (C.10) this density profile will be specularly reflected within the right segment $(1 - Q)L \leq x \leq L$. This reflection will then repeat itself in a cyclic way, with a characteristic period $2t_c$. The occurrence of this phenomenon has also been confirmed by our numerical calculations with the TDBdG equations in the absence of the inter-particle interaction.

Bibliography

[1] B.D. Josephson. Possible new effects in superconductive tunnelling. *Physics Letters*, 1(7):251–253, 1962.

[2] E. Polturak, G. Koren, D. Coher, E. Aharoni, and G. Deutscher. Proximity effect in $yba_2cu_3o_7/y_{0.6}pr_{0.4}ba_2cu_3o_7/yba_2cu_3o_7$ junctions. *Phys. Rev. Lett.*, 67:3038, November 1991.

[3] W. J. Kwon, G. Del Pace, R. Panza, M. Inguscio, W. Zwerger, M. Zaccanti, F. Scazza, and G. Roati. Strongly correlated superfluid order parameters from dc josephson supercurrents. *Science*, 369(6499):84–88, 2020.

[4] G. Del Pace, W. J. Kwon, M. Zaccanti, G. Roati, and F. Scazza. Tunneling transport of unitary fermions across the superfluid transition. *Phys. Rev. Lett.*, 126:055301, Feb 2021.

[5] Wolf Weimer, Kai Morgener, Vijay Pal Singh, Jonas Siegl, Klaus Hueck, Niclas Luick, Ludwig Mathey, and Henning Moritz. Critical velocity in the bec-bcs crossover. *Phys. Rev. Lett.*, 114:095301, Mar 2015.

[6] U. Fano. Effects of configuration interaction on intensities and phase shifts. *Phys. Rev.*, 124:1866–1878, Dec 1961.

[7] Herman Feshbach. Unified theory of nuclear reactions. *Annals of Physics*, 5(4):357–390, 1958.

[8] A. Spuntarelli, P. Pieri, and G. C. Strinati. Josephson effect throughout the bcs-bec crossover. *Phys. Rev. Lett.*, 99:040401, Jul 2007.

[9] Andrea Spuntarelli, Pierbiagio Pieri, and G Calvanese Strinati. Solution of the bogoliubov–de gennes equations at zero temperature throughout the bcs–bec crossover: Josephson and related effects. *Physics Reports*, 488:111–167, 2010.

[10] P. G. de Gennes. *Superconductivity of Metals and Alloys*. Benjamin, 1966.

[11] Vinay Ambegaokar and Alexis Baratoff. Tunneling between superconductors. *Phys. Rev. Lett.*, 10:486–489, Jun 1963.

[12] Donald A. Jacobson. Ginzburg-landau equations and the josephson effect. *Phys. Rev.*, 138:A1066–A1070, May 1965.

[13] H. J. Fink. Supercurrents through superconducting-normal-superconducting proximity layers. i. analytic solution. *Phys. Rev. B*, 14:1028–1038, Aug 1976.

[14] H. J. Fink and R. S. Poulsen. Supercurrents through proximity layers. ii. numerical solution of superconducting-normal-superconducting and superconducting-superconducting-superconducting weak links. *Phys. Rev. B*, 19:5716–5724, Jun 1979.

[15] A. A. Golubov, M. Yu. Kupriyanov, and E. Il'ichev. The current-phase relation in josephson junctions. *Rev. Mod. Phys.*, 76:411–469, Apr 2004.

[16] Gert Eilenberger. Transformation of gorkov's equation for type ii superconductors into transport-like equations. *Zeitschrift für Physik A Hadrons and nuclei*, 214:195, 4 1968.

[17] Jørgen Rammer. *Quantum Field Theory of Non-equilibrium States*. Cambridge University Press, 2007.

[18] Klaus D. Usadel. Generalized diffusion equation for superconducting alloys. *Phys. Rev. Lett.*, 25:507–509, Aug 1970.

[19] S. Simonucci and G. C. Strinati. Equation for the superfluid gap obtained by coarse graining the bogoliubov˘de gennes equations throughout the bcs-bec crossover. *Phys. Rev. B*, 89:054511, Feb 2014.

[20] P. Pieri, L. Pisani, and G. C. Strinati. Bcs-bec crossover at finite temperature in the broken-symmetry phase. *Phys. Rev. B*, 70:094508, Sep 2004.

[21] D. Fausti, R. I. Tobey, N. Dean, S. Kaiser, A. Dienst, M. C. Hoffmann, S. Pyon, T. Takayama, H. Takagi, and A. Cavalleri. Light-induced superconductivity in a stripe-ordered cuprate. *Science*, 331(6014):189–191, 2011.

[22] M. Budden, T. Gebert, M. Buzzi, G. Jotzu, E. Wang, T. Matsuyama, G. Meier, Y. Laplace, D. Pontiroli, M. Riccò, F. Schlawin, D. Jaksch, and A. Cavalleri. Evidence for metastable photo-induced superconductivity in k3c60. *Nature Physics*, 17:611–618, 5 2021.

[23] P. Dyke, A. Hogan, I. Herrera, C. C. N. Kuhn, S. Hoinka, and C. J. Vale. Dynamics of a fermi gas quenched to unitarity. *Phys. Rev. Lett.*, 127:100405, Aug 2021.

[24] H. Fröhlich. Theory of the superconducting state. i. the ground state at the absolute zero of temperature. *Phys. Rev.*, 79:845–856, Sep 1950.

[25] Leon N. Cooper. Bound electron pairs in a degenerate fermi gas. *Phys. Rev.*, 104:1189–1190, Nov 1956.

[26] A. L. Fetter and Walechka J. D. *Quantum Theory of Many-Particle Systems*. Dover Publications, 2014.

[27] G. E. Santoro. Lecture-notes of the course on "non-equilibrium quantum-systems, 2016.

[28] Giancarlo Calvanese Strinati, Pierbiagio Pieri, Gerd Röpke, Peter Schuck, and Michael Urban. The bcs-bec crossover: From ultra-cold fermi gases to nuclear systems. *Physics reports*, 738:1–76, April 2018.

[29] L. P. Gor'kov. Microscopic derivation of the ginzburg-landau equations in the theory of superconductivity. *Sov.Phys. JETP*, 36:1364–1367, Dec 1959.

[30] S. Simonucci and G. Calvanese Strinati. Nonlocal equation for the superconducting gap parameter. *Phys. Rev. B*, 96:054502, Aug 2017.

[31] L. P. Abrikosov, A. A. Gorkov and Dzyaloshinski I. E. *Methods of quantum field theory in statistical physics*. Dover Publications, 2016.

[32] M. A. Baranov and D. S. Petrov. Critical temperature and ginzburg-landau equation for a trapped fermi gas. *Phys. Rev. A*, 58:R801–R804, Aug 1998.

[33] V. Piselli, S. Simonucci, and G. Calvanese Strinati. Josephson effect at finite temperature along the bcs-bec crossover. *Phys. Rev. B*, 102:144517, Oct 2020.

[34] W. Haberkorn, H. Knauer, and J. Richter. A theoretical study of the current-phase relation in josephson contacts. *physica status solidi (a)*, 47(2):K161–K164, 1978.

[35] LG Aslamazov and AI Larkin. Josephson effect in superconducting point contacts. *ZhETF Pisma Redaktsiiu*, 9:150, 1969.

[36] F. Palestini and G. C. Strinati. Temperature dependence of the pair coherence and healing lengths for a fermionic superfluid throughout the bcs-bec crossover. *Phys. Rev. B*, 89:224508, Jun 2014.

[37] Peng Zou and Franco Dalfovo. Josephson oscillations and self-trapping of superfluid fermions in a double-well potential. *Journal of Low Temperature Physics*, 177:240–256, Dec 2014.

[38] P. G. DE GENNES. Boundary effects in superconductors. *Rev. Mod. Phys.*, 36:225–237, Jan 1964.

[39] W. L. McMillan. Tunneling model of the superconducting proximity effect. *Phys. Rev.*, 175:537–542, Nov 1968.

[40] H. le Sueur, P. Joyez, H. Pothier, C. Urbina, and D. Esteve. Phase controlled superconducting proximity effect probed by tunneling spectroscopy. *Phys. Rev. Lett.*, 100:197002, May 2008.

[41] G Deutscher and P G de Gennes. Proximity effects. *pp 1005-34 of Superconductivity. Vols. 1 and 2. Parks, R. D. (ed.). New York, Marcel Dekker, Inc., 1969.*, 2, 10 1969.

[42] Siyuan Han, K. W. Ng, E. L. Wolf, H. F. Braun, Lee Tanner, Z. Fisk, J. L. Smith, and M. R. Beasley. Anomalous s-wave proximity-induced josephson effects in ube_{13}, $cecu_2si_2$, and $labe_{13}$: A new probe of heavy-fermion superconductivity. *Phys. Rev. B*, 32:7567–7570, Dec 1985.

[43] E. V. Thuneberg and Vinay Ambegaokar. Microscopic theory of the proximity-induced josephson effect. *Phys. Rev. Lett.*, 60:365–368, Jan 1988.

[44] V. Piselli, S. Simonucci, and G. Calvanese Strinati. Optimizing the proximity effect along the bcs side of the bcs-bec crossover. *Phys. Rev. B*, 98:144508, Oct 2018.

[45] E. Taylor. Critical behavior in trapped strongly interacting fermi gases. *Phys. Rev. A*, 80:023612, Aug 2009.

[46] L. Landau. Theory of the superfluidity of helium ii. *Phys. Rev.*, 60:356–358, Aug 1941.

[47] P. Nozières and S. Schmitt-Rink. Bose condensation in an attractive fermion gas: From weak to strong coupling superconductivity. *Journal of Low Temperature Physics*, 59, 05 1985.

[48] M. Zaccanti and W. Zwerger. Critical josephson current in bcs-bec–crossover superfluids. *Phys. Rev. A*, 100:063601, Dec 2019.

[49] Luca Salasnich, Nicola Manini, and Alberto Parola. Condensate fraction of a fermi gas in the bcs-bec crossover. *Phys. Rev. A*, 72:023621, Aug 2005.

[50] M Pini, P Pieri, M Jäger, J Hecker Denschlag, and G Calvanese Strinati. Pair correlations in the normal phase of an attractive fermi gas. *New Journal of Physics*, 22(8):083008, aug 2020.

[51] Leonid A. Sidorenkov, Meng Khoon Tey, Rudolf Grimm, Yan-Hua Hou, Lev Pitaevskii, and Sandro Stringari. Second sound and the superfluid fraction in a fermi gas with resonant interactions. *Nature*, 498:78, 6 2013.

[52] Wilhelm Zwerger. *The BCS-BEC Crossover and the Unitary Fermi Gas*. Springer, 2012.

[53] R. G. Scott, F. Dalfovo, L. P. Pitaevskii, and S. Stringari. Rapid ramps across the bec-bcs crossover: A route to measuring the superfluid gap. *Phys. Rev. A*, 86:053604, Nov 2012.

[54] Yung-Sze Choi, Juha Javanainen, Israel Koltracht, Marijan Koštrun, Patrick J. McKenna, and Nataliya Savytska. A fast algorithm for the solution of the time-independent gross–pitaevskii equation. *Journal of Computational Physics*, 190(1):1–21, sep 2003.

[55] M.V. Milošević and R. Geurts. The ginzburg–landau theory in application. *Physica C: Superconductivity*, 470(19):791–795, 2010. Vortex Matter in Nanostructured Superconductors.

[56] Vincent Hakim. Nonlinear schrödinger flow past an obstacle in one dimension. *Phys. Rev. E*, 55:2835–2845, Mar 1997.

[57] Endre Süli and David F. Mayers. *An Introduction to Numerical Analysis*. Cambridge University Press, 2003.

[58] W. Magnus, F. Oberhettinger, and R. P. Soni. *Formulas and Theorems for the Special Functions of Mathematical Physics*. Springer-Verlag, 1966.

[59] Peng Zou. Mean-field theory for the dynamics of superfluid fermions in the bcs-bec crossover, 2014.

[60] Ernst Hairer, Syvert Paul Nørsett, and Gerhard Wanner. *Solving ordinary differential equations I: Nonstiff problems*. Springer-Verlag, 1993.